MANY-BODY PHYSICS AND NON-EQUILIBRIUM DYNAMICS IN ULTRACOLD ATOMIC SYSTEMS

A Dissertation

Presented to the Faculty of the Graduate School

of Cornell University

in Partial Fulfillment of the Requirements for the Degree of

Doctor of Philosophy

by

Matthew Douglas Reichl

August 2017

MANY-BODY PHYSICS AND NON-EQUILIBRIUM DYNAMICS IN ULTRACOLD ATOMIC SYSTEMS

Matthew Douglas Reichl, Ph.D.

Cornell University 2017

This thesis presents a series of theoretical studies of ultra cold atomic systems which model and propose experiments, and develop new computational techniques in order to elucidate aspects of many-body physics and non-equilibrium dynamics. In the first two studies I model the dynamics of non-linear solitonic excitations in ultracold fermionic superfluids: the first simulates recent experiments and supports the hypothesis that the solitons generated in those experiments are unstable to the formation of vortex rings; the second demonstrates how population imbalance between up and down spin fermions can be used to prevent this instability. In the next study I discuss a method for generating and probing topologically protected edge states using periodically driven optical lattices potentials. Next I use a perturbative approach to study the spectral density of fermions with strong attractive interactions in the normal phase. After that I develop a novel cluster expansion technique to model the dynamics of interacting fermions in a disordered optical lattice. Finally I apply a Ginzurg-Landau theory to model experimental studies of superfluid ^{3}He embedded in nematically ordered aerogel, finding evidence for a new phase of matter –the "polar phase"– which is not seen in bulk ^{3}He.

BIOGRAPHICAL SKETCH

Matthew Reichl was born and raised in Houston, Texas where he earned his Bachelor's degree in Physics and Mathematics from the University of Houston. While at UH, Matthew performed research in statistical physics, studying non-equilibrium phase transitions and complex networks with Professor Kevin Bassler. Matthew began graduate studies at Cornell University in 2011 and joined Professor Erich Mueller's research group in 2012. In 2014, Matthew was awarded a Masters degree in Physics. After earning his Ph.D at Cornell, Matthew will begin a career in quantitative finance at an investment bank in Charlotte.

In his spare time, Matthew enjoys reading nonfiction, engaging in spirited discussions of politics and culture, listening to music, and performing as a jazz pianist.

ACKNOWLEDGEMENTS

The work presented in this thesis would not have occurred without the love and support of my family, friends, mentors and fellow grad students. I would first like to acknowledge my advisor Erich Mueller. His enthusiasm for physics and the energy he brings to research continue to motivate and inspire me. I owe a debt of gratitude for his helpfulness, his patience, and for all the physics I've learned from him.

I also owe much to the other physics faculty at Cornell. Of the many courses I took during my first few years of graduate school, I particularly benefited from Quantum Field Theory taught by Csaba Csaki, Solid State Physics taught by Chris Henley, and Basic Training in Condensed Matter Physics taught by the LASSP theory faculty. I would also like to thank Paul Ginsparg and Mukund Vengallatore for serving on my committee, and Jeevak Parpia for allowing me a chance to collaborate with his group and for serving on my committee as well.

I've learned much from the other graduate students and visitors in Erich's group– Shovan, Sayan, Bhuvanesh, Yariv, Ran, Nur, Levent, and Junjun– as well as those I shared offices with in Rockefeller and Clark Hall– Evan, Yi, Johannes, Yi-Ting, and Kyungmin. I've also enjoyed many interesting conversations and crossword puzzels over lunch with Bhuvanesh and Ran and many debates with my political sparring partner Simon. Shoutout to my jazz friends– Joannalyn, Simon, Paul, Curran, Christine, Tom, Noah, Chris– for playing great music and allowing me a chance to temporarily escape from my physics work.

I owe thanks to my family in Houston – Dad, Sue, Erik, Mark, Scott, Aunt Barbara, Grandma and Grandpa – and my family in the UK – Renee, Yannig and their new addition Michele-Christine – for all their support and for providing a warm home to visit during the holidays.

I will forever be grateful to my best friend and partner Melody. I am sure I would not have been as happy in college or grad school without her kindness, love and never-ending support.

Finally, I would like to acknowledge the various funding agencies and programs which have supported my research at Cornell: the National Science Foundation under grants No. PHY-1068165 and No. PHY-1508300, the National Science Foundation Graduate Research Fellowship under grant DGE-1144153, ARO-MURI Non-equilibrium Many-body Dynamics grant W911NF-14-1-0003, and the Cornell Graduate Fellowship.

TABLE OF CONTENTS

LIST OF FIGURES

CHAPTER 1

INTRODUCTION AND OUTLINE

1.1 Introduction

Since the first experimental realization of Bose-Einstein condensation in 1995 [9, 44], the study of ultracold atomic systems has proven to be among the most fruitful avenues for furthering our understanding of quantum many-body physics. In these systems, gases of fermionic or bosonic atoms are confined in optical potentials and cooled to nano-kelvin temperatures where quantum statistics and the wave-like nature of the atoms become crucial for describing their behavior. The utility of these systems for exploring quantum mechanics comes from the wide plethora of "knobs" – the density, the shape of the confinement, the strength and nature of interactions, the degree of disorder – which experimentalists can tune to precisely control and manipulate the atoms.

This control makes these ultracold systems a veritable playground for theorists like me to develop and apply new mathematical and computational tools, and to dream up schemes for observing novel quantum phenomena. One of the joys of being a theorist in this field is the ability to explore a wide breadth of physics and work on many different projects, either analyzing and modeling previously performed experiments, or envisioning new ones. Unfortunately this aspect of the field also makes for a generally disjointed thesis. Rather than focusing on one specific subtopic, this thesis presents a series of separate projects studying cold atomic systems which are loosely connected by the themes of many-body physics and non-equilibrium dynamics. An outline and description of each chapter is listed below.

1.2 Outline

In Chapter 2, we use the time-dependent Gross-Pitaevskii equation to study the motion of a vortex ring produced by phase imprinting on an elongated cloud of cold atoms. Our approach models the experiments of Yefsah et al. [176] on ^{6}Li in the Bose-Einstein-condensate regime where the fermions are tightly bound into bosonic dimers. We find ring oscillation periods which are much larger than the period of the axial harmonic trap. Our results lend further strength to Bulgac et al.'s arguments [29] that the heavy solitons seen in those experiments are actually vortex rings. We numerically calculate the periods of oscillation for the vortex rings as a function of interaction strength, trap aspect ratio, and minimum vortex ring radius. In the presence of axial anisotropies the rings undergo complicated internal dynamics where they break into sets of vortex lines, then later combine into rings. These structures oscillate with a similar frequency to simple axially symmetric rings.

In Chapter 3, we use the time-dependent Bogoliubov de Gennes equations to study dark solitons in three- dimensional spin-imbalanced superfluid Fermi gases. We explore how the shape and dynamics of dark solitons are altered by the presence of excess unpaired spins which fill their low-density core. The unpaired particles broaden the solitons and suppress the transverse snake instability. We discuss ways of observing these phenomena in cold atom experiments.

In Chapter 4, we describe an experimental setup for imaging topologically protected Floquet edge states using ultracold bosons in an optical lattice. Our setup involves a deep two dimensional optical lattice with a time dependent superlattice that modulates the hopping between neighboring sites. The finite

waist of the superlattice beam yields regions with different topological numbers. One can observe chiral edge states by imaging the real-space density of a bosonic packet launched from the boundary between two topologically distinct regions.

In Chapter 5, we compute the spectral density in the normal phase of an interacting homogenous Fermi gas using a T-matrix approximation. We fit the quasiparticle peaks of the spectral density to BCS-like dispersion relations, and extract estimates of a pseudo-gap energy scale and an effective Fermi- wavevector as a function of interaction strength. We find that the effective Fermi-wavevector of the quasiparticles vanishes when the inverse scattering length exceeds some positive threshold. We also find that near unitarity the quasiparticle lifetimes, estimated from the widths of the peaks in the spectral density, approach values on the order of the inverse Fermi-energy. These results are consistent with the breakdown of Fermi liquid theory observed in recent experiments.

In Chapter 6, motivated by experiments in Munich [147], we study the dynamics of interacting fermions initially prepared in charge density wave states in one-dimensional bichromatic optical lattices. The experiment sees a marked lack of thermalization, which has been taken as evidence for an interacting generalization of Anderson localization, dubbed many-body localization. We model the experiments using an interacting Aubry-Andre model and develop a computationally efficient low-density cluster expansion to calculate the even-odd density imbalance as a function of interaction strength and potential strength. Our calculations agree with the experimental results and shed light on the phenomena. We also explore a two-dimensional generalization. The clus-

ter expansion method we develop should have broad applicability to similar problems in non-equilibrium quantum physics.

Finally in Chapter 7, we discuss and analyze the results from an experiment performed by collaborators at Cornell which used a torsion pendulum to measure the superfluid density of ^{3}He confined in an extremely anisotropic, nematically ordered aerogel. Kinks in the development of the superfluid fraction (at various pressures) as the temperature is varied correspond to phase transitions. Two such transitions are seen in the superfluid state, and we use Ginzburg-Landau theory to help identify the superfluid phase closest to the critical temperature at low pressure as the polar state, a phase that is not seen in bulk ^{3}He.

CHAPTER 2

VORTEX RING DYNAMICS IN TRAPPED BOSE EINSTEIN CONDENSATES

The work discussed in this chapter was originally published as *Vortex ring dynamics in trapped Bose-Einstein condensates* by M. D. Reichl and E. J. Mueller, Physical Review A **88** 053626 (2013).

Yefsah et. al. [176] recently observed anomalously slow oscillations of a nominal soliton in a harmonically trapped fermonic superfluid. By illuminating half the cloud with light, they generated a phase profile with a large jump. This phase jump evolved into a localized density depletion that oscillated with a period many times larger than the period associated with the harmonic trap. This slow motion is remarkable, as it exceeds the best theoretical calculations of the oscillation frequency of a soliton [104, 148] by an order of magnitude. Recently, Bulgac et. al. [29] hypothesized that the experimental protocol produces a vortex ring instead of a soliton. Through integrating time dependent equations based upon a superfluid density functional theory, Bulgac et. al. showed that near unitarity the experimental observations are consistent with this vortex ring hypothesis. Here we extend this analysis to the BEC regime, where the fermions are tightly bound into dimers.

To study this problem, we numerically evolve the time-dependent Gross-Pitaevskii (GP) equation to simulate the dynamics of vortex rings. We model the phase imprinting process and measure the period of oscillations of the vortex ring as a function of interaction strength, trap aspect ratio, and initial ring radius. We find that the period of oscillation for the vortex ring is quantitatively consistent with the experimental observations in the BEC regime.

In our simulations, the phase imprinting produces a soliton [64] which decays into a vortex ring through a "snake instability". This instability has been explored in the past [100, 119, 61, 64, 34], as has the structure and motion of individual vortex rings [152, 20, 136, 7, 141, 86, 54, 96, 83, 73, 79, 1, 32]. Despite these precedents, our exploration of this full process, in this particular geometry, is novel. An excellent review of the theory of solitons and vortices in BEC's can be found in Ref. [33].

Experimentally, vortex rings have been observed in the decay of dark solitons [8], in complex vortex ring/soliton oscillations [66, 154], and in binary condensates [114].

2.1 Physics of Vortex Rings

The flow in a Bose condensate is irrotational ($\nabla \times \mathbf{v} = 0$, where $\mathbf{v} = \frac{\hbar}{m}\nabla\phi$ is the local velocity and ϕ is the phase of the order parameter) except at line singularities. The superfluid phase winds by $2\pi n$, for integer n, when one moves around one of these vortex lines. Here we study configurations where these vortex lines form loops. In particular, consider a cigar shaped cloud, elongated along the $\hat{z}$ axis, with a vortex ring in a perpendicular plane, concentric with the cloud. In Sec. 2.2 we numerically solved the time-dependent GP equation to analyze such a ring, but its basic properties can be understood from a semiclassical argument given by Jackson et. al. [83] for a vortex ring in a spherically symmetric condensate. They find that each element of the vortex ring moves with a velocity $\mathbf{v}$:

$$\mathbf{v} = v_{in}(R)\hat{\mathbf{z}} + \omega_p \hat{\kappa} \times \mathbf{r} \tag{2.1}$$

where $\hat{\kappa}$ defines the direction of the circulation at the element.

The first term in Eq. 2.1 describes the induced velocity $v_{in}(R)$ resulting from the sum of the velocity contributions from each element on the ring. For a ring in a uniform condensate, this induced velocity is a function of the ring radius R and is given by $v_{in}(R) = \frac{\hbar}{2mR}[\log(8R/\xi) - 0.615]$ [141], where ξ is the coherence length. Thus the ring has an inherent tendency to propagate along the z-axis.

A cartoon of this physics comes from the two-dimensional analog of a vortex ring: a vortex dipole consisting of two point vortices–one with circulation $+\kappa$, the other with $-\kappa$. If these are separated by a distance $2R$, they move with a velocity $v = \frac{\kappa}{4\pi R}$ [128].

The second term in Eq. 2.1 describes the Magnus force on the ring caused by the harmonic trap. In the case of a straight vortex line, this forces leads to precession with frequency ω_p. Note that w_p is not equal to any trap frequency; for instance, in the Thomas-Fermi limit, a single vortex in a two-dimensional condensate will precess with a frequency given by [62]

$$\omega_p = \frac{3\hbar\omega^2}{4\mu}\log(\frac{R_\perp}{\xi}) \tag{2.2}$$

where ω is the trap frequency, $\mu = \hbar^2/2m\xi^2$ and $R_\perp^2 = 2\mu/m\omega^2$.

A small ring ($R << R_\perp$) beginning at $z = 0$ will have a large velocity component in the positive z direction. As it moves in the z direction the Magnus term, $\hat{\kappa} \times \mathbf{r}$, causes the ring to grow. Once the ring radius is sufficiently large the Magnus force pushes the ring in the negative z direction. In this manner the ring

moves periodically. The two dimensional analog of this motion was observed in experiments by Neely et. al. [123].

While this model is too simple to produce a quantitative prediction for the period of these vortex ring oscillations, it captures the qualitative behavior of the vortex ring seen in the numerical simulations discussed in Sec. 2.2.3. Moreover, it predicts that the period should increase roughly as $T_{ring} \sim \frac{1}{\xi^2 \log(1/\xi)} \sim gn/\log gn \sim g^{2/5}/\log g$ where g is the interaction strength and n is the density. This scaling is seen in our simulations (see Fig. 2.3). We note that the period of dark soliton oscillations, $T_{sol} = \sqrt{2}T_z$ [31, 95, 23] where T_z is the trap period in the z direction, is independent of g. For sufficiently large g we expect slower oscillations for the vortex ring than the dark soliton.

We also note that the vortex ring dynamics are highly nonlinear, and that the ring's oscillation period is strongly dependent on the minimum ring radius. As in Bulgac et. al.'s work [29], we find that smaller radii lead to shorter periods (see Fig. 2.5). We also find that the oscillations are non-sinusoidal, with a slight asymmetry between the motion to the left and to the right.

2.2 Numerical Results

2.2.1 Simulation Details

In this section we present results from numerical simulations of the time-dependent GP equation:

$$i\hbar\partial_t\psi = -\frac{\hbar^2}{2m}\nabla^2\psi + V_t(r,z)\psi + \frac{4\pi\hbar^2 aN}{m}|\psi|^2\psi + V_i(t,r,z)\psi \tag{2.3}$$

where N is the total number of particles, a is the scattering length and ψ is normalized such that

$$\int |\psi(\vec{r})|^2 d^3r = 1 \tag{2.4}$$

$V_t(r,z) = \frac{m}{2}(\omega_r^2 r^2 + \omega_z^2 z^2)$ is a harmonic trapping potential and $V_i(t,r,z)$ is a time dependent phase-imprinting potential which we'll describe below.

After rescaling the variables $t \to \omega_z t$, $\vec{r} \to \frac{1}{a_z}\vec{r}$ where $a_z = \sqrt{\frac{\hbar}{m\omega_z}}$, and rescaling $\psi \to a_z^{3/2}\psi$, we can rewrite the GP equation in the dimensionless form:

$$i\partial_t\psi = -\frac{1}{2}\nabla^2\psi + g|\psi|^2\psi + \frac{1}{2}(\lambda^2 r^2 + z^2)\psi + V_i(t,r,z)\psi \tag{2.5}$$

where $\lambda = \frac{\omega_r}{\omega_z}$ is the trap aspect ratio and $g = \frac{4\pi a N}{a_z}$ parametrizes the interaction strength. As discussed in Sec. 2.2.3, an experimentally relevant set of parameters are $\lambda = 6$ and $g = 3 \times 10^4$.

In Secs. 2.2.2 and 2.2.3 we assume axial symmetry while in Sec. 2.2.4 we carry out full 3D simulations, including slight trap asymmetries. We numerically solve Eq. 2.5 using a split-step method. We use a square grid, choosing our grid spacing sufficiently small that the dynamics are independent of the grid. We find for our parameter range that it suffices to take $\delta r = \delta z = 0.1$. Smaller grids are necessary for larger interactions. Similarly we find a time step $\delta t = 10^{-3}$ suffices for preventing large phase jumps between time steps, ensuring numerical stability. We set $V_i(t,r,z) = \frac{\pi}{\delta t}\Theta(t)\Theta(\delta t - t)f(z)$ so that a sharp ϕ phase jump is imprinted about the line $z = 0$ after the first time step. Each simulation begins after first relaxing the system into the ground state of the trapping potential using imaginary time propagation.

The resulting dynamics after phase-imprinting can depend sensitively on the precise shape of $f(z)$. However, away from the quasi-one dimensional

regime ($\lambda << ng$), we find from our simulations that $f(z)$ generically creates a soliton that quickly decays into one (as in Fig. 2.1) or more vortex rings via a snake instability. For simplicity, and in keeping with the experimental observations in Ref. [176] where there is only one discernible density depletion, we choose $f(z) = \frac{1}{2}(1 + \tanh(z/\delta z))$ where δz is our numerical grid spacing. This protocol consistently results in only one long lasting vortex ring.

It is difficult to control the minimum radius R_{min} of the vortex ring using this phase printing technique. Therefore, to study the behavior of the vortex ring as function of R_{min}, we do not use phase imprinting but instead relax the gas to a state with the following ansatz for its phase:

$$\frac{\psi(r,z)}{|\psi(r,z)|} = \frac{(r - R_{min}) + iz}{\sqrt{(r - R_{min})^2 + z^2}} \tag{2.6}$$

This ansatz closely approximates the phase of the vortex rings created after phase imprinting and allows us to easily investigate the ring behavior as a function of R_{min}.

2.2.2 Example of Snake Instability and Vortex Ring Dynamics

Fig. 2.1 shows an example of the dynamics of the condensate following phase imprinting. A soliton, seen as a density dip extending axially through the condensate, travels in the positive z direction and almost immediately begins bowing outward near the center of the gas (see $t/T_z = 0.04$ in Fig. 2.1). By time $t/T_z = 0.16$ the soliton has decayed via this snake instability leaving a vortex ring which is seen as two zero density cores in the $y = 0$ slice shown in Fig. 2.1.

Fig. 2.2 shows an example of the vortex ring oscillations that follow the decay of a soliton. At $t/T_z \approx 1.2$ the vortex ring is positioned at $z = 0$ and is traveling in

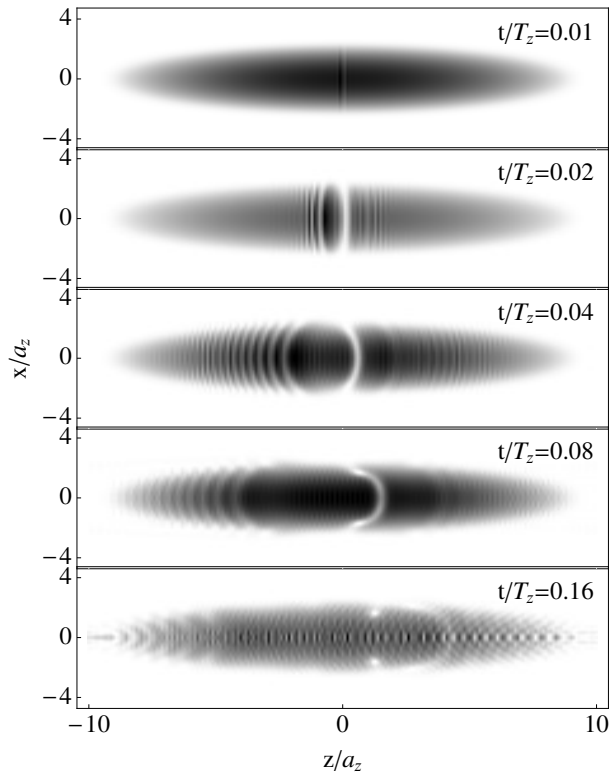

Figure 2.1: Condensate dynamics following phase imprinting with $g = 4000$, $\lambda = 4$. Each graph shows the density $|\psi(x, y = 0, z)|^2$, where darker colors represent higher density. The dark soliton is unstable and forms a vortex ring (seen as two zero density cores) at time $t/T_z \approx 0.16$.

the negative z direction. The ring continues to travel in this direction until $t/T_z \approx 1.8$. After this time the ring radius expands to the edge of condensate while the ring begins traveling back in the positive z direction. The ring completes half of an oscillation and returns to $z = 0$ at $t/T_z \approx 2.4$. In the following subsection we calculate the frequency of vortex ring oscillations as a function of g, λ, and R_{min}.

2.2.3 Period of Vortex Ring Oscillations

Fig. 2.3 shows a plot of the vortex ring oscillation period as a function of interaction strength g with a trap aspect ratio of $\lambda = 4$ Each point is computed by

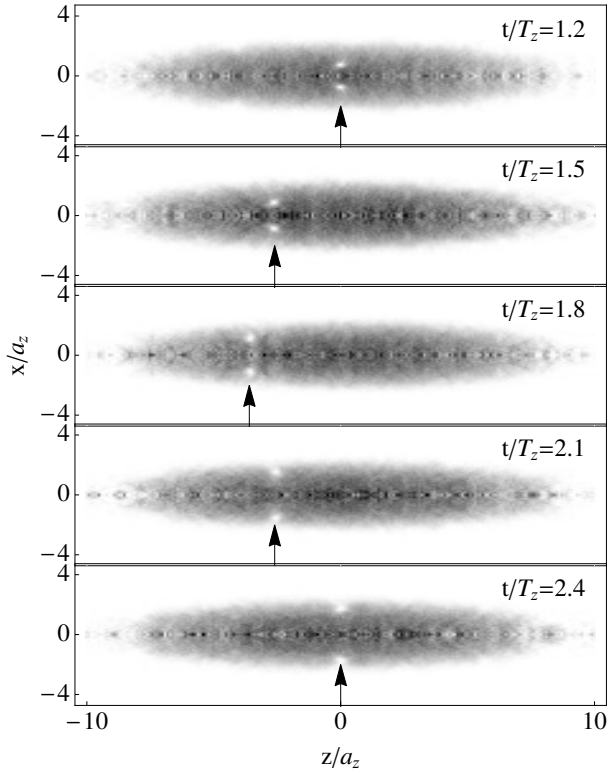

Figure 2.2: Half of a vortex ring oscillation with $g = 4000$, $\lambda = 4$. Each graph shows the density $|\psi(x, y = 0, z)|^2$, where darker colors represent higher density. An arrow is shown pointing to the vortex ring.

first preparing the vortex ring with the phase imprinting method discussed in Sec. 4.2, and then calculating the number of time steps for a vortex core starting at $z = 0$ to complete an oscillation and return to $z = 0$. As predicted above, the oscillation period increases as $gn/\log gn$ for large gn. Moreover, for $g \gtrsim 500$, the vortex ring oscillates at a period larger than the period for a dark soliton in a BEC $T = \sqrt{2}T_z$ [31, 95, 23].

In Fig. 2.4 we plot the oscillation period of the ring as function of trap aspect ratio λ, at constant interaction strength $g = 4000$. The period decreases at larger aspect ratios which is consistent with observations in Ref. [176]. The explanation for this trend is that our phase imprinting method yields vortex rings with smaller minimum radii at larger λ. As discussed in Sec. 2.1, the rings with

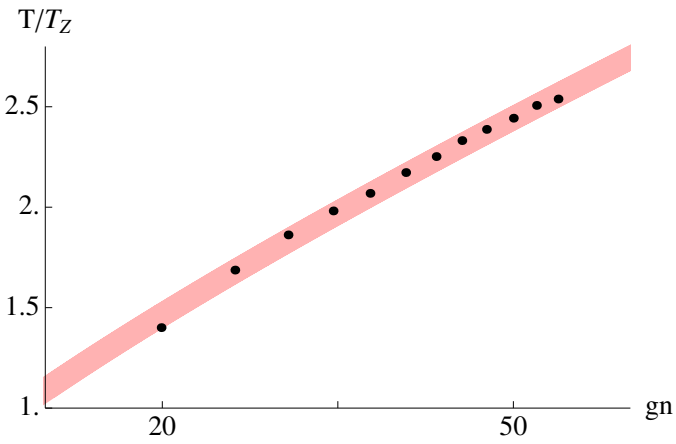

Figure 2.3: Vortex ring oscillation period T (normalized by the trap period T_z) versus interaction strength times the density gn with a trap aspect ratio of $\lambda = 4$ after phase imprinting. As predicted in Sec. 2.1, $T \sim gn/\log gn$; the thick red curve shows a fit of the data to this scaling.

smaller R_{min} have smaller periods.

To explore the radius dependence of the ring dynamics, we find the ring oscillation period as function of R_{min} (see Eq. 2.6) with $g = 4000$ and $\lambda = 4$ using the relaxation procedure discussed in the last paragraph of Sec. 4.2. The results are shown in Fig. 2.5 which clearly demonstrates that rings with smaller R_{min} have smaller periods; this is consistent with a similar finding reported in Ref. [29].

Finally, we compare our simulations to the experiment in Ref. [176]. Typical experimental parameters in the BEC regime are: $T_r \approx 14$ms, $T_z \approx 87$ms, total number of bosonic Feshbach molecules $N \approx 1.1 \times 10^5$, Thomas-Fermi radius $R_{TF} = (R_{TF_x} R_{TF_y} R_{TF_z})^{1/3} = 135\mu$m, and $\frac{1}{k_F a_F} \approx 2.6$ where $k_F \approx 0.86(\mu\text{m})^{-1}$ is the Fermi wave vector and $a_F \approx 0.448\mu$m is the fermionic scattering length at $B = 700G$. Noting that $a = 0.6 a_F$ [131], these parameters give $\lambda = 6.2$ and $g = 3.08 \times 10^4$ in our dimensionless units.

We find that with these parameters the soliton created after phase imprinting

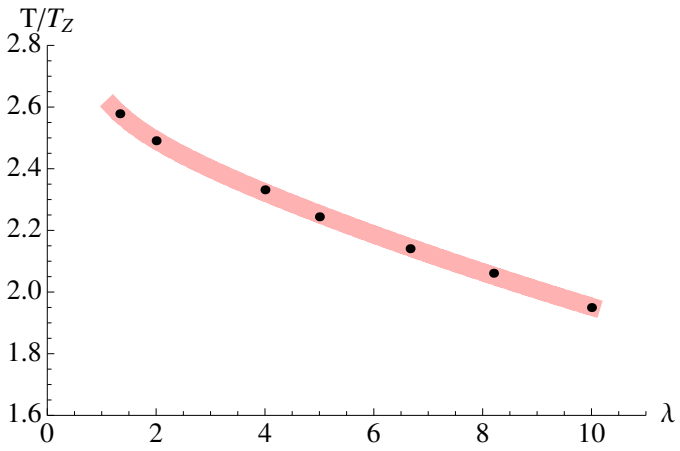

Figure 2.4: Vortex ring oscillation period T (normalized by the trap period T_z) versus trap aspect ratio $\lambda = \frac{\omega_r}{\omega_z}$ after phase imprinting with $g = 4000$. The thick red curve is an interpolation to guide the eye.

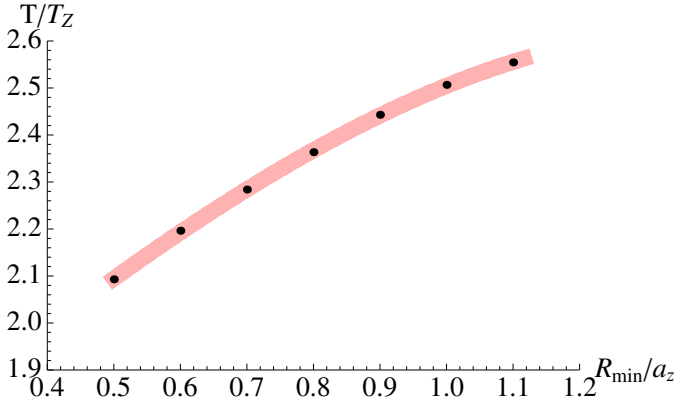

Figure 2.5: Vortex ring oscillation period T (normalized by the trap period T_z) versus the minimum vortex ring radius R_{min} with $g = 4000$ and $\lambda = 4$. The thick red curve is an interpolation to guide the eye.

quickly decays into a vortex ring. The period depends sensitively on the minimum ring radius (as in Fig. 2.5), which in turn depends on the phase imprinting protocol. We can reproduce (within the reported error bars) the experimentally measured period of $T = 4.4 \pm 0.5 T_z$ by relaxing to a vortex ring state using the ansatz in Eq. 2.6 with $R_{min} = 1.2 a_z$. It is plausible that the particular phase imprinting procedure used in the experiment yields a vortex ring with a similar minimum ring radius.

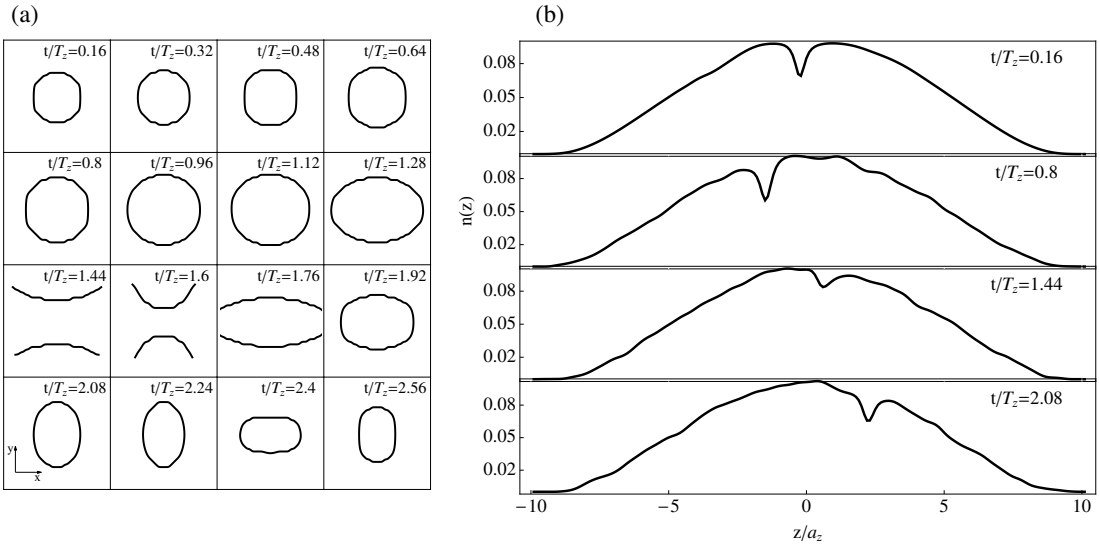

Figure 2.6: Vortex ring dynamics in the presence of a small perturbation to axial symmetry ($V_t(x, y, z) = \frac{1}{2}[\lambda^2(0.99x^2 + y^2) + z^2]$). Here $\lambda = 4$, $g = 4000$, and the system is initialized with a vortex ring of radius $R = 1.0a_z$ located at $z = 0$. (a) The locations of non-zero vorticity at different times projected into the x-y plane. (b) The density of the condensate at different times integrated over the x and y directions, $n(z) = \int dxdy\rho(x, y, z)$.

2.2.4 Ring Dynamics with Axial Asymmetry

To give a more complete picture, we relaxed our assumption of axial asymmetry and performed fully three dimensional simulations with a trap potential given by $V_t(x, y, z) = \frac{1}{2}[\lambda^2(0.99x^2 + y^2) + z^2]$. We again find the vortex structure moves periodically in the z-direction (with roughly the same period), but we find additional internal dynamics, some of which is related to previous studies[78, 132].

This evolution is illustrated by Fig. 2.6a which shows the locations of non-zero vorticity at different times projected into the x-y plane (here $\lambda = 4$, $g = 4000$). Figure 2.6b shows the density of the condensate integrated over the x and y directions. The system at time $t = 0$ contains a vortex ring of radius $R = 1.0a_z$ located at $z = 0$. After one half of an oscillation (at $t/T_z \approx 1.4$) the

vortex ring breaks apart into two lines of opposite vorticity extending along the x axis, which continue to move together along the z axis. After reaching the edge of the condensate, the vortex lines recombine into a ring which then moves in the opposite direction along the z-axis. Similar behavior is seen over the range of parameters explored in Sec. 2.2.3. From the axial density profiles in Fig. 2.6b, however, none of this internal dynamics is apparent. In fact Fig. 2.6b looks like an oscillating grey soliton.

2.3 Conclusion

Using numerical simulations, we have found that dark solitons created through phase imprinting in three dimensional BECs are unstable to becoming vortex rings, and that these vortex rings oscillate with much larger periods than solitons. We numerically computed the period of these vortex ring oscillations as a function of interaction strength, trap aspect ratio, and minimum vortex ring radius. We found that our results are qualitatively consistent with Jackson et. al.'s [83] semiclassical model of vortex rings for axially symmetric potential traps. Slight perturbations to axial symmetry produce negligible changes to the oscillation period of the ring, but cause the ring to break apart and recombine during oscillations. Finally, we simulate the BEC regime of a recent experiment claiming to have observed oscillations of "heavy" dark solitons in cold Fermi gases [176]. The oscillation periods of vortex rings in our simulations are quantitatively consistent with the periods of the supposed solitons, and we therefore conclude that these solitons are likely to be vortex rings, or more complicated objects as shown in Fig. 2.6.

A key distinction between vortex rings and solitons, besides their dynamics, is their density profile: a vortex ring appears as two density dips in a two-dimensional profile, while a soliton appears as a solid line of density depletion extending across the condensate. In fermionic superfluids away from the BEC regime, the density depletion associated with vortices and solitons is small, as the cores are filled by normal fluid. For superfluids initially away from the BEC regime, Yefsah et. al. [176] were forced to ramp the magnetic field to the deep BEC regime in order to clearly observe *any* density depletion in their gas after releasing it from the trap. We recommend further experiments in the BEC regime where such ramps are unnecessary. We note that previous experiments with BECs have successfully distinguished vortex rings from dark solitons using expansion imaging [8], and *in situ* imaging [154]. We also note that several of the images in Ref. [176] are suggestive of vortex rings or tangles. This is particularly true of the images in the supplementary information section.

A less direct distinguishing feature of a vortex ring's dynamics is the asymmetry of its motion. For example if the ring is smaller when moving left to right, it will move faster during that interval than on the return. In Fourier analysis of the existing experimental data, this asymmetry would show up as odd harmonics. We calculated the first odd harmonic for the experimental parameters, and unfortunately found it too small to readily measure. Devising techniques to generate vortex rings with a smaller minimum radii would improve this situation.

Finally, we should mention one shortcoming of our modeling. We find that for our axially symmetric simulations the period of the vortex ring is sensitive to the imprinting protocol,while the experiment finds very reproducible periods.

Perhaps the more complicated structures in Sec. 2.2.4 yield more reproducibility. The computational cost of the full 3D simulations have prevented us from studying this in detail.

2.3.1 New Experiments

Following the publication of the work discussed in this chapter, a series of experiments [97, 98] were performed using new imaging techniques designed to correctly identify the collective excitations described in Ref. [176]. Consistent with our simulations, these new experiments found that planar solitons created through phase imprinting undergo snaking instabilities and break apart to form vortex rings. Because of the axially asymmetry in the harmonic trap used in the experiments, these vortex rings in turn break apart to form stable vortex lines which oscillate within the trap.

CHAPTER 3

CORE FILLING AND SNAKING INSTABILITY OF DARK SOLITONS IN SPIN-IMBALANCED SUPERFLUID FERMI GASES

The work discussed in this chapter was originally archived online as *Core filling and snaking instability of dark solitons in spin-imbalanced superfluid Fermi gases* by M. D. Reichl and E. J. Mueller arXiv:1703.04808, and submitted for publication in Physical Review A.

Ultracold atoms have become the best platform for studying collective nonlinear phenomena such as dark solitons. Dark solitons are persistent nonlinear collective excitations in which the density is reduced in a plane. They have been studied in a number of physical settings including atomic Bose-Einstein Condensates (BECs) [64] and superfluid Fermi gases of spin-1/2 atoms [11, 104, 148, 176]. They are ubiquitous in quenches [101, 53] and can be engineered through phase imprinting protocols [30, 47, 8, 23, 176, 97, 98]. Previous experimental [163, 8, 57, 53, 97, 98] and theoretical work [177, 85, 99, 111, 119, 61, 120, 27, 87, 28, 34, 112, 29, 139, 108] has discovered that these dark solitons are dynamically unstable to a "snaking" instability transverse to the plane of the soliton in both BECs and Fermi gases. In this chapter, we theoretically study the dynamics of dark solitons in superfluid Fermi gases in which there is an imbalance between the number of up and down spins in the system. We find that the snaking instability is suppressed by the presence of excess spins which reside within the density depleted plane–or core–of the soliton.

Previous work [34] has studied the snaking instability in spin-balanced Fermi gases using similar approaches as this chapter. More recently, the authors of Refs. [107, 108] applied an effective field theoretic approach [92] to studying

core filling and snaking instabilities of dark solitons in imbalanced Fermi gases. In this chapter, we take a more microscopic approach and model the Fermi gas using the Bogoliubov de Gennes (BdG) equations. Our work also extends recent simulations of the stability of one-dimensional soliton trains [56] which suggest that excess spin can stabilize dynamical instabilities of dark solitons.

The BdG theory captures the phenomenology of the BEC-BCS crossover [180]: at strong attractive interactions the fermions form tightly bound bosonic pairs which condense into a BEC, while at weak interactions the fermions form Cooper pairs which form a neutral analog to a BCS superconductor. Here we study the unitary gas which lies between these two limits. We caution that the BdG theory is a mean-field theory which only approximately models strong correlation physics in the unitary gas. However, the BdG equations has been successfully utilized in previous studies of dark soliton profiles and dynamics in the unitary gas [11, 104, 148, 157, 149] and appears to be semi-quantitative.

In Sec. 3.1 we discuss the BdG model and find stationary dark solitons in the presence of imbalance. In Sec. 3.2 we apply time-dependent BdG equations to simulate the snaking instability. In Sec. 3.3 we discuss how our results might be observed in cold atom experiments.

3.1 Stationary Dark Solitons

3.1.1 Model

We consider the following Hamiltonian which describes spin-imbalanced spin-1/2 fermions with short-range attractive interactions

$$\hat{H} = \int d^3\vec{x}\Big[\sum_{\sigma=\uparrow,\downarrow} \Psi^\dagger_\sigma(\vec{x})(-\frac{\hbar^2\nabla^2}{2m} - \mu_\sigma)\Psi_\sigma(\vec{x}) - g\Psi^\dagger_\uparrow(\vec{x})\Psi^\dagger_\downarrow(\vec{x})\Psi_\downarrow(\vec{x})\Psi_\uparrow(\vec{x})\Big] \tag{3.1}$$

Here μ_σ is the chemical potential for spin component σ and g is the bare interaction strength. g is related to the s-wave scattering length a_s by $1/g = -m/(4\pi\hbar^2 a_s) + \frac{1}{V}\sum_k 1/(2\epsilon_k)$ where V is the volume of the system and $\epsilon_k = \frac{\hbar^2 k^2}{2m}$. The sum over momenta comes with a cutoff determined by the grid spacing of our numerics. In this chapter we focus our attention on the unitary limit $a_s \to \infty$.

At zero temperature, up and down spin atoms combine into Cooper pairs and condense to form a superfluid. We rewrite $\hat{H}$ in terms of the Cooper pair field $\Delta(\vec{x}) = g\langle\Psi_\uparrow(\vec{x})\Psi_\downarrow(\vec{x})\rangle$ and neglect quadratic fluctuations. This gives the following mean-field BdG Hamiltonian [45]

$$\hat{H}_{\text{BdG}} = \int d^3\vec{x}\begin{pmatrix} \Psi_\uparrow(\vec{x}) \\ \Psi^\dagger_\downarrow(\vec{x}) \end{pmatrix}^\dagger \begin{pmatrix} -\frac{\hbar^2\nabla^2}{2m} - \mu_\uparrow & \Delta(\vec{x}) \\ \Delta^*(\vec{x}) & \frac{\hbar^2\nabla^2}{2m} + \mu_\downarrow \end{pmatrix} \begin{pmatrix} \Psi_\uparrow(\vec{x}) \\ \Psi^\dagger_\downarrow(\vec{x}) \end{pmatrix} \tag{3.2}$$

H_{BdG} is diagonalized through a Bogoliubov transformation

$$\begin{pmatrix} \Psi_\uparrow(\vec{x}) \\ \Psi^\dagger_\downarrow(\vec{x}) \end{pmatrix} = \sum_n \begin{pmatrix} u_n(\vec{x}) & -v^*_n(\vec{x}) \\ v_n(\vec{x}) & u^*_n(\vec{x}) \end{pmatrix} \begin{pmatrix} \gamma_{\uparrow,n} \\ \gamma^\dagger_{\downarrow,n} \end{pmatrix} \tag{3.3}$$

where $\gamma^\dagger_{\sigma,n}$ is the creation operator for a Bogoliubov excitation of energy $E_{\sigma,n} =$

$E_n \pm h$ where E_n are the positive eigenvalues of the equation

$$\begin{pmatrix} -\frac{\hbar^2\nabla^2}{2m} - \mu & \Delta(\vec{x}) \\ \Delta^*(\vec{x}) & \frac{\hbar^2\nabla^2}{2m} + \mu \end{pmatrix} \begin{pmatrix} u_n(\vec{x}) \\ v_n(\vec{x}) \end{pmatrix} = E_n \begin{pmatrix} u_n(\vec{x}) \\ v_n(\vec{x}) \end{pmatrix} \tag{3.4}$$

and where h and μ are given by $h = \frac{1}{2}(\mu_\uparrow - \mu_\downarrow)$ and $\mu = \frac{1}{2}(\mu_\uparrow + \mu_\downarrow)$. At zero temperature, $\Delta(\vec{x})$ is expressed in terms of u's and v's as

$$\Delta(\vec{x}) = g \sum_{E_n>0} u_n(\vec{x}) v_n^*(\vec{x})(1 - \Theta(-E_{\uparrow,n}) - \Theta(-E_{\downarrow,n})) \tag{3.5}$$

where $\Theta(x)$ is the unit step function. The density $n_\sigma(\vec{x})$ of fermions with spin σ is given by

$$\begin{aligned} n_\sigma &= \langle \Psi_\sigma^\dagger(\vec{x}) \Psi_\sigma(\vec{x}) \rangle \\ &= \sum_{E_n>0} \left[|u_n(\vec{x})|^2 \Theta(-E_{\sigma,n}) + |v_n(\vec{x})|^2 (1 - \Theta(-E_{-\sigma,n})) \right] \end{aligned} \tag{3.6}$$

3.1.2 Numerical results

We numerically solve the coupled equations (3.4) and (3.5) using an iterative procedure. We first choose an ansatz pair field $\Delta(\vec{x}) = \Delta \tanh(x/\xi)$ corresponding to a planar dark soliton fixed at $x = 0$. ξ parametrizes the width of the soliton core and is generally chosen in the ansatz to be $\xi \approx k_F$, where $k_F \equiv (3\pi^2 n_o)^{1/3}$ is the Fermi wavevector and n_o is the density far from the core of the soliton. We then solve Eq. (3.4) and calculate a new Δ from Eq.(3.5). This process is repeated until Δ converges to a stationary solution. In all the calculations presented in this chapter we check that Δ converges to same stationary solution after small changes to the initial ansatz.

For simplicity we consider a system in a rectangular box geometry with dimensions $L_x \times L_\perp \times L_\perp$. We impose periodic boundary conditions in the y

and z (perpendicular) directions, and in the x-direction we impose the conditions: $u_n(x + L_x) = u_n(x)$ and $v_n(x + L_x) = -v_n(x)$. This boundary condition in the x-direction ensures that $\Delta(x + L_x) = -\Delta(x)$, which is consistent with the profile of a single dark soliton in a finite size box. Because of the homogeneity of the stationary soliton in the perpendicular directions, the solution to Eq. (3.4) can be expressed in the form $u_n(\vec{x}) = u_{m,k_y,k_z}(x)\exp(ik_y y + ik_z z)$, $v_n(\vec{x}) = v_{m,k_y,k_z}(x)\exp(ik_y y + ik_z z)$. This effectively reduces the three dimensional problem to a series of one-dimensional problems for each k_y and k_z, and substantially speeds up the calculation.

Fig. 3.1 shows the total density $n_\uparrow + n_\downarrow$ (solid blue curve) and density difference $n_\uparrow - n_\downarrow$ (dashed orange curve) for stationary dark soliton solutions in the presence of spin imbalance. The densities are plotted as functions of x after integrating over the y and z directions. In these calculations the dimensions of the box are set to $L_x k_f \approx 28$ and $L_\perp k_f \approx 23$, and we use 60 grid points along the x-direction and 50 k-space points in both perpendicular directions. Our results are unchanged by using more grid points.

We characterize the spin imbalance using the relative spin imbalance n_I:

$$n_I = \frac{n_\uparrow(x = 0) - n_\downarrow(x = 0)}{n_o} \tag{3.7}$$

where as before n_o is the total density far from the core. Fig. 3.1 shows a range of imbalances from $n_I = 0$ to $n_I = 0.33$. As the imbalance is increased, the soliton core (visually represented in the figure as the dip in the total density at $x = 0$) fills with excess up spins and widens. This is consistent with previous calculations using different methods [107, 108] and is expected given simple energetic considerations: the most energetically favorable place to store excess unpaired spins is at the core of the soliton where $\Delta = 0$ and hence no Cooper pairs need to

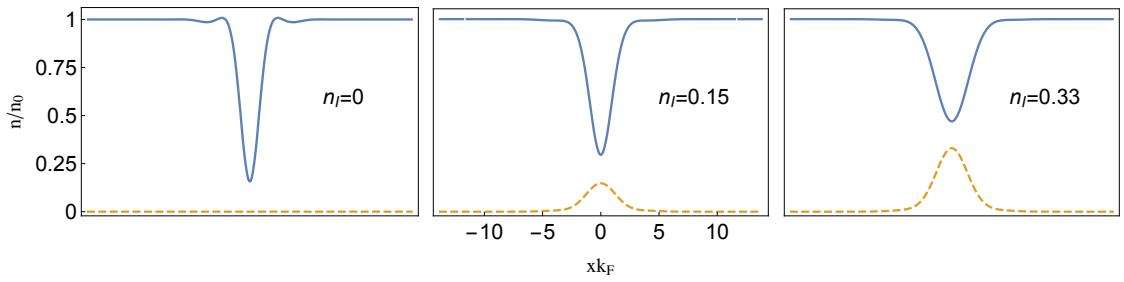

Figure 3.1: Density profiles of a dark soliton at different relative spin imbalances $n_I = 0, 0.15, 0.33$ (Eq. 3.7) . The solid blue curves show the total density $n_\uparrow + n_\downarrow$ and the dashed orange curves show the density difference $n_\uparrow - n_\downarrow$. The densities are plotted as a function of x after integrating over the y and z directions and normalizing by the asymptotic density n_o

be broken. On a more microscopic level, the soliton supports a band of midgap Andreev states which are bound to the core of the soliton [11] which are filled by excess spins after tuning the chemical potential bias h away from 0.

3.2 Snaking Instability

In this section we discuss time dependent simulations of the snaking instability of dark solitons in the presence of spin imbalance. We find that the instability proceeds slower or, for sufficiently high imbalance, is completely suppressed by the presence of excess spins in the core of the soliton.

We numerically solve the following time-dependent BdG equations:

$$\begin{pmatrix} -\frac{\hbar^2\nabla^2}{2m} - \mu & \Delta(\vec{x},t) \\ \Delta^*(\vec{x},t) & \frac{\hbar^2\nabla^2}{2m} + \mu \end{pmatrix} \begin{pmatrix} u_n(\vec{x},t) \\ v_n(\vec{x},t) \end{pmatrix} = i\hbar\frac{\partial}{\partial t} \begin{pmatrix} u_n(\vec{x},t) \\ v_n(\vec{x},t) \end{pmatrix} \tag{3.8}$$

where

$$\Delta(\vec{x},t) = g\sum_{E_n>0} u_n(\vec{x},t)v_n^*(\vec{x},t)(1-\Theta(-E_{\uparrow,n})-\Theta(-E_{\downarrow,n})) \tag{3.9}$$

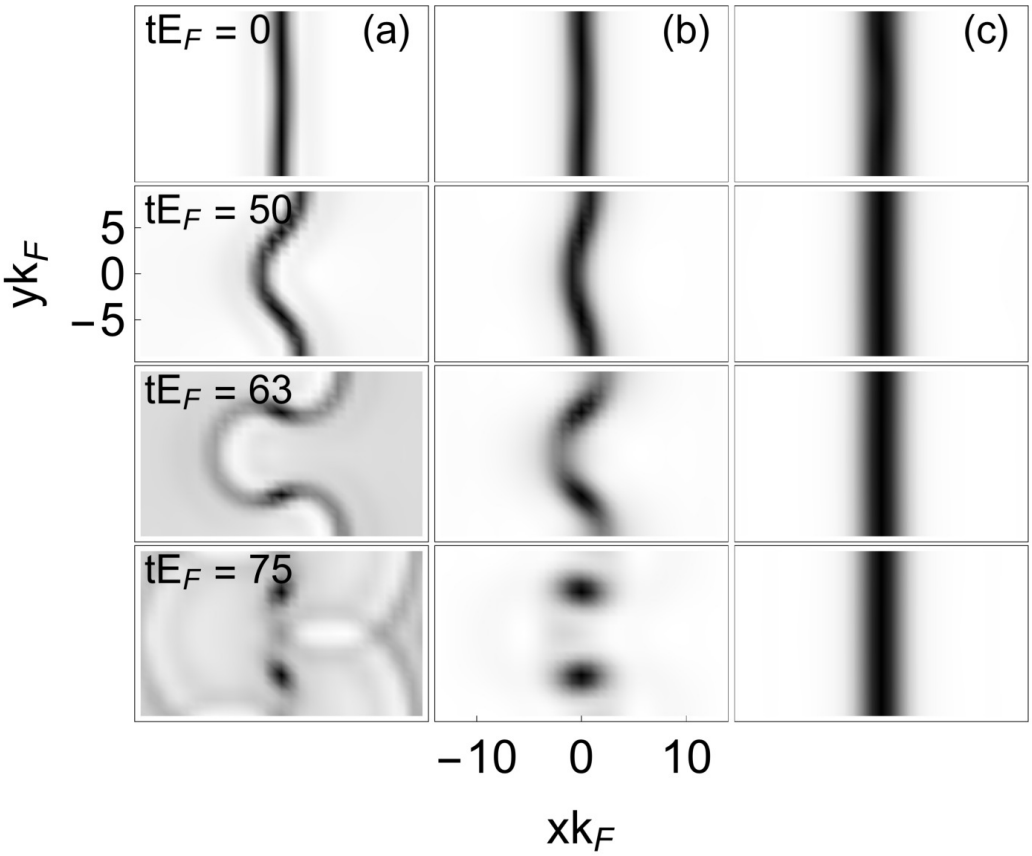

Figure 3.2: Dynamics of the snaking instability of dark solitons in the presence of excess spins. Dark colors are regions of low density. The relative spin imbalances n_I at the core of the soliton (Eq. 3.7) are $n_I = 0, 0.18, 0.40$ for columns (a), (b), (c), respectively. The transverse length is $L_\perp k_F \approx 18$.

The initial set of $u_n(\vec{x}, 0)$ and $v_n(\vec{x}, 0)$ and the E_n's in Eq. (3.9) are stationary solutions of Eqs. (3.4) and (3.5). For simplicity we again consider a system at unitarity ($a_s = \infty$) in a rectangular box geometry of dimensions $L_x \times L_\perp \times L_\perp$, and we use the same boundary conditions as in Sec. 5.2. We assume homogeneity along the z-direction and express the u_n's and v_n's in the form $u_n(\vec{x}, t) = u_{m,k_z}(x, y, t) \exp(ik_z z)$ and $v_n(\vec{x}, t) = v_{m,k_z}(x, y, t) \exp(ik_z z)$. We use approximately 1000 grid points in the $x - y$ plane and 25 k_z points.

In all the simulations described here, we first perturb the stationary $\Delta(x)$ by

adding a small term which seeds a snaking instability along the y-direction:

$$\Delta(\vec{x}, 0) = \Delta(\vec{x}) + \epsilon \,\mathrm{sech}(x) \sin \frac{2\pi}{L_y}(y - L_y/4) \tag{3.10}$$

where $\epsilon \approx 0.1\Delta_o$ and Δ_o is the value of Δ far from the soliton core. We then discretize time and evolve the set of u_n's and v_n's forward by one time step using a split step method with Δ calculated from the current time-step. After finding the new u_n's and v_n's, we calculate $\Delta(t)$ at the next time-step using Eq. (3.9).

Figure 3.2 shows the dynamics of a dark soliton for three different relative imbalances $n_I = 0, 0.18, 0.4$ (columns (a), (b), (c), respectively). The figures show graphs of the density as a function of x and y after integrating over the z dimension; darker colors correspond to regions of low density. In these graphs we have $L_x k_F \approx 28$ and $L_\perp k_F \approx 18$. At zero imbalance there is clearly a snaking instability whose rate is consistent with similar calculations in other work [34]. The plane of the soliton buckles and eventually breaks leaving behind two vortex cores. However at $n_I = 0.18$, the instability occurs at a slower rate and finally at $n_I = 0.4$ the instability is completely suppressed. We have run these simulations up to times of $t = 150/E_F$, finding no sign of a snaking instability for large imbalances.

Figure 3.3 shows time scales for the snaking instability at different imbalances and different transverse dimensions $L_\perp$. Each time scale τ was calculated by first extracting the position of the core $x_{\mathrm{core}}(t)$ along the $y = 0$ line, and fitting it to a exponential function $x_{\mathrm{core}}(t) \sim \exp(t/\tau)$. At zero imbalance the time scale gets larger as $L_\perp$ increases. This trend is somewhat counter-intuitive, but can be understood by noting that the unstable mode's wavelength grows as $L_\perp$ increases. The instability connects with the Goldstone mode, and hence its frequency $\omega = i\hbar/\tau$ vanishes as $L_\perp \to \infty$. Similar results were seen in Ref. [34]. For

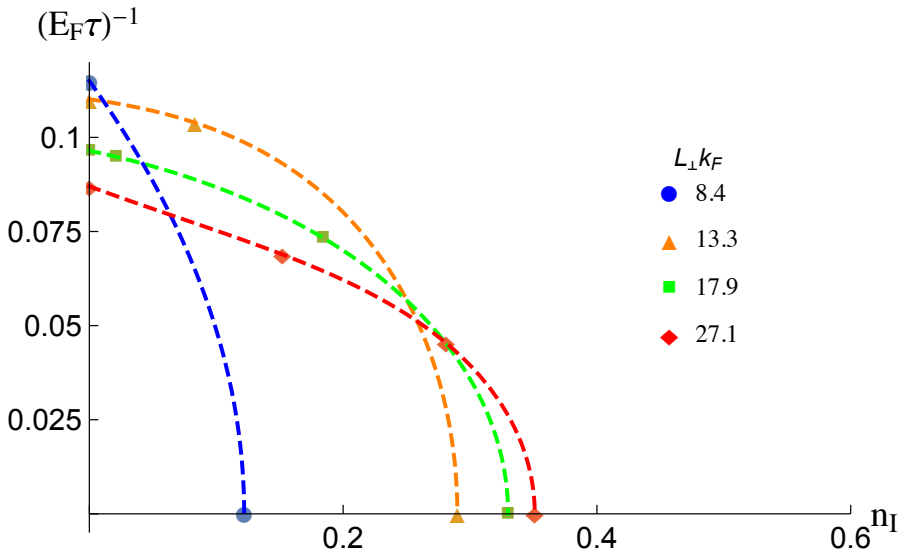

Figure 3.3: Time scale τ for the decay of a dark soliton via a transverse snaking instability as a function of the relative spin imbalance n_I (Eq. (3.7)) at the core of the soliton . The different colors and shapes represent different transverse lengths $L_\perp$. The dashed curves show guides for the eye.

larger $L_\perp$ (beyond those shown in this figure) additional decay modes appear. For sufficiently small $L_\perp$ ($\frac{\hbar^2}{mL_\perp^2} \sim \mu$) the rate will again decrease as the system becomes quasi-one dimensional. For small enough $L_\perp$ the soliton is stable, even without imbalance.

Once the soliton core is filled with excess spins the rate of the snaking instability becomes slower and is eventually suppressed altogether (up to times of at least $tE_F = 150$). At smaller $L_\perp$ the snaking instability is suppressed for smaller values of spin imbalance.

3.3 Discussion

In this chapter we have studied the dynamics of a dark soliton in an imbalanced Fermionic superfluid. We have found that the snaking instability of the soliton

is suppressed by the presence of excess spins which reside at the low density core of the soliton.

We feel that observing this physics experimentally is feasible given existing tools. In a trapped imbalanced Fermi gas at equilibrium, excess spins reside along the edge of the trap [125]. One naive idea is therefore to phase imprint a soliton onto the system and allow for the excess spins to diffuse from the edge of the trap into the core of the soliton. Unfortunately, the time scales for this process are prohibitively long. Instead we suggest first using a laser to create a potential barrier across the center of the trap and separating the imbalanced superfluid into two disjoint regions. This geometry was produced in Ref. [167]. Excess spins will then reside at the center of the trap between the two superfluid halves. Phase imprinting should then result in a soliton whose core is at the location of the excess spins. Varying the shape and dynamics of the applied potential barrier should allow experimentalists to control the relative imbalance n_I. One can image the soliton in time of flight after a ramp to the BEC limit as done in Refs. [176, 97, 98].

CHAPTER 4

FLOQUET EDGE STATES WITH ULTRACOLD ATOMS

The work discussed in this chapter was originally published as *Floquet edge states with ultracold atoms* by M. D. Reichl and E. J. Mueller, Physical Review A **89** 063628 (2014).

One of the most exciting prospects in ultracold atomic physics is the ability to experimentally engineer and probe quantum states with topological order. Many of the theoretical proposals in this direction involve synthetic gauge fields [105, 41] which require complicated experimental setups in which Raman lasers couple internal atomic degrees of freedom. More recently there have been proposals to generate topological order in Floquet systems with periodically driven optical lattices [74, 93, 178, 179, 21, 40]. While every technique brings its own technical challenges, the Floquet approaches appear to be simpler. Similar proposals appear in the solid state and photonics literature [106, 164, 70, 77]. Recent cold atoms experiments have successfully demonstrated uniform 1D gauge fields [159] and band hybridization [127] using shaken optical lattices. Time-periodic Hamiltonians with effective magnetic fields have also been implemented with Raman techniques [4, 116].

In this chapter we propose an experiment that simulates an especially simple square-lattice Floquet Hamiltonian [143] that nonetheless displays edge state physics and topological order. We discuss an implementation using bosons in an optical lattice, and demonstrate using numerical simulations how edge states can be directly imaged in the system.

Our proposal for probing edge states in this system involves initializing and

releasing a wave packet of bosons at the spatial boundary between two topological phases and directly observing chiral edge states by watching how this packet evolves. This proposal can be thought of as the cold atom analogue to a recent quantum optics experiment [137] where wave packets of light were directly observed propagating along the edge of a topological Floquet system. Here bosonic atoms play the role of the photons. Our imaging scheme is similar to the proposal in Ref. [69] where propagating edge states are also directly observed in the density of atoms following the initialization and release of a wave packet. In that study, the authors considered non-driven topological systems. Our work extends this basic imaging idea to Floquet topological insulators. There are also connections between this approach and ideas of directly measuring Chern numbers by following wave-packet dynamics [135, 90, 43, 16, 171].

4.1 Model

The simplest description of our proposed experiment is in terms of a two-dimensional tight binding model given by a Hamiltonian $H(t)$

$$\begin{aligned} H(t) = \sum_{ij} & J_1(t)[c^\dagger_{B_{i,2j-1}} c_{A_{i+1,2j-1}} + c^\dagger_{B_{i,2j}} c_{A_{i,2j}} + h.c.] + J_2(t)[c^\dagger_{B_{i,j+1}} c_{A_{i,j}} + h.c.] \\ & + J_3(t)[c^\dagger_{B_{i,2j-1}} c_{A_{i,2j-1}} + c^\dagger_{B_{i+1,2j}} c_{A_{i,2j}} + h.c.] + J_4(t)[c^\dagger_{B_{i,j}} c_{A_{i,j+1}} + h.c.] \end{aligned} \tag{4.1}$$

where

$$J_m(t) = \begin{cases} J, & \text{if } \frac{(m-1)}{5}T < t \mod T < \frac{m}{5}T \\ 0, & \text{otherwise} \end{cases} \tag{4.2}$$

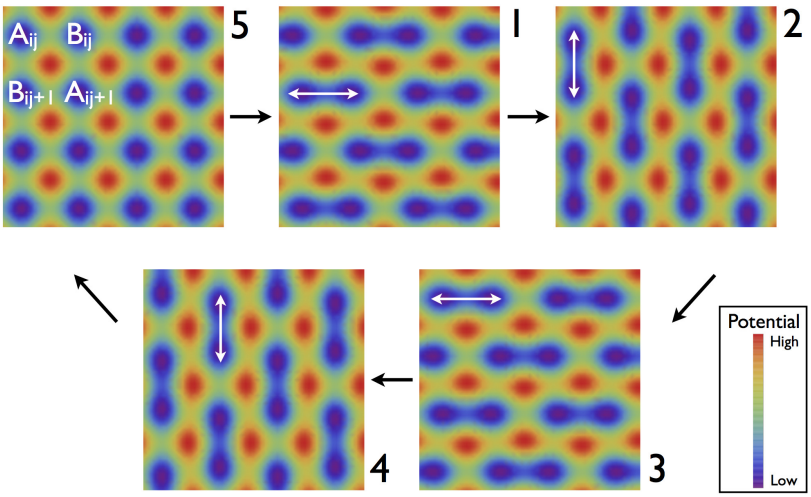

Figure 4.1: Snapshots of the potentials used to produce the tight binding model for trapped atoms studied in this chapter (Eq. 4.1). Each potential is applied sequentially for a fixed period of time. As shown in the key, blue and red respectively correspond to low and high potential. As depicted by the white arrows, during time-steps 1, 2, 3, and 4, hopping only occurs between closely spaced "dimers". No hopping occurs during time-step 5. The labeling of sites A_{ij} and B_{ij} are illustrated in panel 5. For the protocol described here, step 5 plays no role, but is convenient for generalizations that include a potential bias between A sites and B sites [143].

are the time dependent hopping parameters, and T is the period of $H(t)$. Fig. 4.1 gives a pictorial representation of this model. The fifth time interval, where $H(t) = 0$, is unnecessary for our proposal but is included here in order to connect with prior literature [143]. Section 4.3 describes how this model can be realized.

The sudden jumps between different hoppings are unnecessary, but make the analysis simpler. This model is readily generalized to the case where the hoppings $J_m(t)$ vary continuously with time. In an experiment the jumps can be quite sharp: For a tight binding model to be applicable, all time dependence need only be slow compared to the band spacing.

This same model is discussed in detail in Ref. [143]. Here we review some of

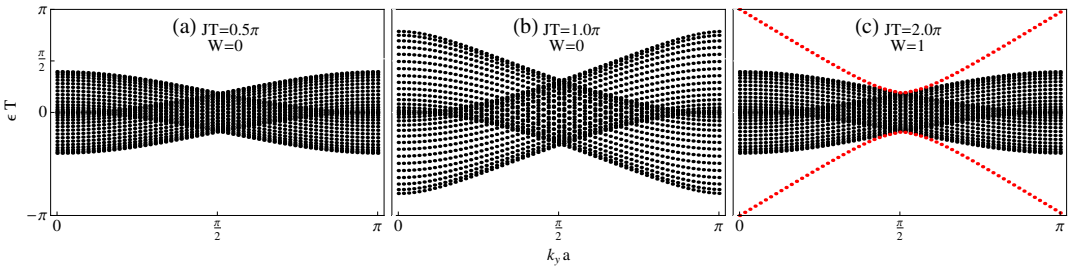

Figure 4.2: Floquet band structure of the model in Eq. 4.1 with open boundary conditions in the x-direction and periodic boundary conditions in the y-direction. For weak hopping ($JT < J_cT = \frac{5}{4}\pi$: panels (a) and (b)) there are two overlapping bulk bands and the winding number $W = 0$ (see Eq. 4.6). For larger J, two edge modes are apparent (shown in red), and $W = 1$. [cf. Ref. [143]].

its essential features.

Because of the periodicity of the Hamiltonian $H(t + T) = H(t)$, we can use Floquet's theorem to express solutions of the time-dependent Schrodinger equation in the form $|\psi(t)\rangle = \exp(-i\epsilon t)|\phi(t)\rangle$ where $|\phi(t + T)\rangle = |\phi(t)\rangle$. These states are eigenstates of the time evolution operator $U(t)$ evaluated at $t = T$: $U(T)|\psi(0)\rangle \equiv |\psi(T)\rangle = \exp(-i\epsilon T)|\psi(0)\rangle$. Often $U(T)$ is calculated using perturbation theory in T, but here we find $U(T)$ exactly.

We can then define an effective time-independent "Floquet Hamiltonian" $H_{\text{eff}} = i \log(U(T))/T$. The branches of the log are chosen so that the eigenvalues of H_{eff}, the quasi-energy spectrum ϵ, fall within $-\pi/T < \epsilon \leq \pi/T$. One can take energy-space to be periodic, identifying ϵ with $\epsilon + \frac{2\pi n}{T}$ for any integer n. If we impose periodic boundary conditions on Eq. 4.1, $H(t)$ has the following form in momentum space:

$$
\begin{aligned}
H(t) &= \sum_{\mathbf{k}} (c^{\dagger}_{\mathbf{k},A} c^{\dagger}_{\mathbf{k},B}) H(\mathbf{k},t) \begin{pmatrix} c_{\mathbf{k},A} \\ \\ c_{\mathbf{k},B} \end{pmatrix} \\
H(\mathbf{k},t) &= -J \sum_{n=1}^{4} (e^{i\mathbf{b}_n \cdot \mathbf{k}} \sigma^{+} + e^{-i\mathbf{b}_n \cdot \mathbf{k}} \sigma^{-})
\end{aligned}
\tag{4.3}
$$

where $\sigma^{\pm} = (\sigma_x \pm i\sigma_y)/2$, $\mathbf{b}_1 = -\mathbf{b}_3 = (a, 0)$, $\mathbf{b}_2 = -\mathbf{b}_4 = (0, a)$, and a is the nearest-neighbor lattice spacing. We can then label the quasi-energies $\epsilon(\mathbf{k})$,where $\mathbf{k}$ is the quasi-momentum. Of particular importance is the structure of H_{eff} near $\mathbf{k} = \mathbf{0}$ which is given by

$$
H_{\text{eff}} T \approx \pi + (\pi - \tfrac{4JT}{5})\sigma_x + f(J)\left[k_{-} \sin\left(\tfrac{JT}{5}\right)\sigma_y + k_{+} \cos\left(\tfrac{JT}{5}\right)\sigma_z\right] \tag{4.4}
$$

where $k_{-} = a(k_x - k_y)$, $k_{+} = a(k_x + k_y)$ and

$$
f(J) \equiv 4\left(\frac{\pi - \frac{4JT}{5}}{\sin\left(\frac{4JT}{5}\right)}\right) \sin^2\left(\frac{JT}{5}\right) \cos\left(\frac{JT}{5}\right) \tag{4.5}
$$

When $\frac{4JT}{5} = \pi$, the function $f(JT) \to 1$, and this has the structure of the 2D massless Dirac equation: $(H_{\text{eff}} T - \pi) \approx a(k_x - k_y)\sigma_x + a(k_x + k_y)\sigma_y$.

Boundaries, or spatial inhomogeneities can be accommodated in the real-space formalism of Eq. (4.1), and can lead to edge modes [91, 143].

In Fig. 4.2, we plot the band structure $\epsilon(k_y)$ for the system in a strip-geometry (open boundary conditions in the x-direction and periodic in the y-direction) for $JT = 0.5\pi, 1.0\pi, 2.0\pi$. We will later consider more realistic experimental geometries. The phase at $JT = 0.5\pi$ and $JT = 1.0\pi$ is topologically trivial and there are no edge modes in the system. However, as one would expect from Eq. 4.4, at $JT = J_c T = \frac{5}{4}\pi$ the gap at $\epsilon = \pi/T$ closes. The gap then reopens for $J > J_c$,

leaving edge modes connecting the top of the band to the bottom as seen in Fig. 4.2(c). As argued by Rudner et. al. [143] the topological invariant in this case is a "winding number" W calculated from the full time evolution operator $U(t, k_x, k_y)$:

$$W[U] = \frac{1}{8\pi^2} \int dt dk_x dk_y \cdot Tr(\tilde{U}^{-1}\partial_t \tilde{U} \cdot [\tilde{U}^{-1}\partial_{k_x}\tilde{U}, \tilde{U}^{-1}\partial_{k_y}\tilde{U}]) \tag{4.6}$$

where

$$\tilde{U}(t) = U(2t)\Theta(T/2 - t) + U_{\text{eff}}(2T - 2t)\Theta(t - T/2) \tag{4.7}$$

In the topologically trivial phase $W = 0$, meaning one can continuously deform $U(t)$ into $U_{\text{eff}}(t) \equiv e^{-iH_{\text{eff}}t}$. In the topologically nontrivial phase (for instance at $JT = 2.0\pi$) $W = 1$ and there is no continuous path between them. Interestingly, the Chern numbers for the bulk bands of H_{eff} are zero for all J [143].

4.2 Imaging Edge States

In this section we discuss an experimental method for imaging edge states in the Floquet model discussed in the previous section.

4.2.1 Edge State Physics

Edge states can appear at the boundary between topologically distinct phases. In solid state models, this could be a boundary between "vacuum" and a topological insulator or a domain boundary in a system with spatially modulated parameters [89]. In the model considered here, the simplest interface to engineer is between the states in Fig. 4.2(a) and Fig. 4.2(c). As such we envision a spatially dependent hopping generated by the spatial profile of the laser

beams creating the lattice (see Sec. 4.3). Such spatially dependent hopping has precedence in cold atom experiments: Mathy et. al. recently proposed using a similar approach to help attain magnetic order in the Fermi-Hubbard model [113]. Fig. 4.3(a) shows a typical hopping profile $J(x)T = 2\pi \exp[-\frac{(x-L/2)^2}{2\sigma^2}]$. Also shown are the local values of the winding number W as predicted by a local density approximation. Here we take periodic boundary conditions in the y-direction. This geometry is purely for theoretical convenience. In Sec. 4.2B we consider the more experimentally relevant geometry where J varies with $r = \sqrt{(x-\frac{L}{2})^2 + (y-\frac{L}{2})^2}$. One expects an edge mode at the interface where $JT = J_c T = \frac{5}{4}\pi$. In our strip geometry we label this location as x_o. For the graph in Fig. 4.3(a), $\sigma = \frac{L}{2\sqrt{6}}$, $L = 40a$, and $x_o \approx 7.5a$ where L is the system size.

Fig. 4.3 (b) through (d) shows slices of the single-particle local density of states $\rho(\epsilon, x)$,

$$\rho(\epsilon, x) = \sum_n \int dy |\psi_n(x,y)|^2 \delta(\epsilon - \epsilon_n) \tag{4.8}$$

where ψ_n and ϵ_n are the eigenstates and eigenenergies of the Floquet Hamiltonian H_{eff}; we have broadened the delta function in Eq. 4.8 to a Lorentzian of width $0.05/T$. As expected, we find a density of mid gap edge states at the spatial locations where the hopping parameter $J(x,y)$ crosses between distinct topological regions. As is clear from Fig. 4.2, these mid-gap states should be visible at $\epsilon T = \pi$ (see Fig. 4.3(b)). There are proposals to spectroscopically detect such edge states [67, 68].

The structure of the states near the boundary is elucidated by expanding H_{eff} about $k_x = k_y = 0$ (Eq. 4.4) and $x = x_o$. Linearizing $J(x)$ at $x = x_o$ and squaring both sides of Eq. 4.4 gives

$$(H_{\text{eff}}T - \pi)^2 = (\frac{4T}{5} J'(x_o)(x - x_o))^2 + 2a^2(k_x^2 + k_y^2) \tag{4.9}$$

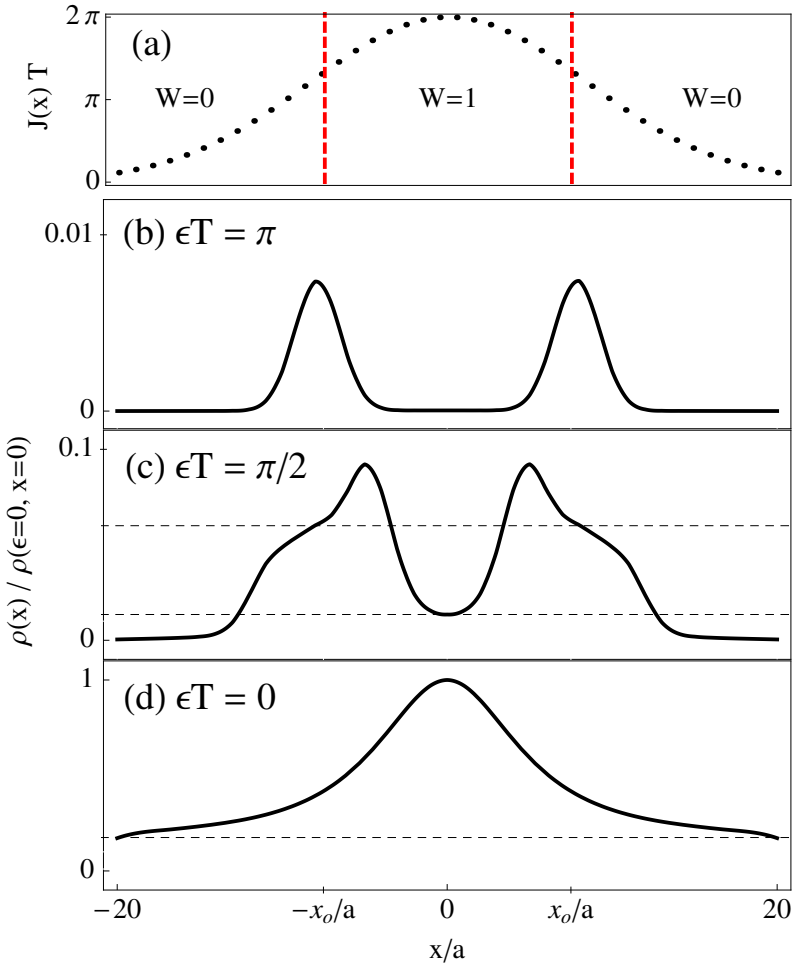

Figure 4.3: (a) Spatially dependent hopping $J(x)$. (b,c,d) The corresponding local density of states $\rho(\epsilon, x)$ at $\epsilon T = \pi, \pi/2, 0$ (see Eq. 4.8). The red dashed lines in the top graph separate spatial regions that are in different topological phases. Mid-gap edge states at $\epsilon T = \pi$ are spatially localized at the boundary $\pm x_o$ between the different phases. Dashed horizontal lines are drawn to help visualize the strongest features.

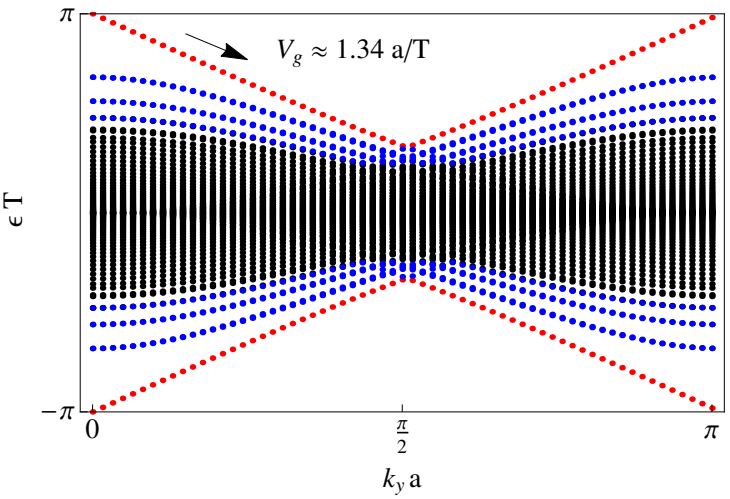

Figure 4.4: Dispersion relation $\epsilon(k_y)$ for a system with spatially dependent hopping $J(x)$ (see Fig. 4.3). The red points specify the energies of "massless" edge states with dispersion $(\epsilon(k_y) - \frac{\pi}{T}) \propto k_y$. These lie at the boundary between the $W = 1$ and $W = 0$ regions in Fig. 4.3(a). The edge-state group velocity V_g is given by slope of these lines $V_g = \frac{\partial \epsilon}{\partial k_y} \approx 1.34a/T$. The blue points specify the energies of "massive" states with dispersion $(\epsilon_n(k_y) - \frac{\pi}{T}) \propto \sqrt{\widetilde{m_n}^2 + V_g^2 k_y^2}$ (see Eq. 4.10).

In the strip geometry considered in this section, k_y is a good quantum number while k_x should be interpreted as a differential operator $k_x = \frac{1}{i}\partial_x$. This is just an harmonic oscillator Hamiltonian in the x-direction plus a constant proportional to k_y^2. The energy spectrum of H_{eff} for the $\epsilon > 0$ branch is then given by

$$\epsilon_n(k_y) = \frac{\pi}{T} - \sqrt{m_n^2 + V_g^2 k_y^2} \tag{4.10}$$

where $m_n = \sqrt{n \times 2\sqrt{2}a(\frac{4T}{5}J'(x_o))}$, $V_g = \sqrt{2}\frac{a}{T}$, and $n \geq 0$ is an integer. There is one linearly dispersing "massless" edge mode ($n = 0$) and ladder of "massive" modes localized near x_o with effective mass $m_n \propto \sqrt{n}$. These analytic results match the numerical results shown in Fig. 4.4 (red and blue points corresponding to $n = 0$ and $4 \geq n > 0$, respectively) within $\sim 10\%$ error. The approximations we have used here improve for smaller $J'(x_o)$.

4.2.2 Imaging Protocol

To experimentally observe the edge states in this setup, we suggest watching the motion of a wave-packet of bosons. Fig. 4.5 shows the time evolution of the boson density in a simulation with spatial dependent hopping given by $J(x,y)T = 2\pi \exp[-\frac{(x-L/2)^2+(y-L/2)^2}{2\sigma^2}]$. When the system is initialized with a gaussian wave packet localized at the boundary, we find a clearly identifiable wave packet propagating in the clockwise-direction along a circle of radius $7.5a$ (Fig. 4.5(a)). The time it takes for the wave packet to propagate around the circle once, $t' \approx 35T$, is consistent with the group velocity V_g we calculated in Fig. 4.4: $t' = \frac{\text{circumference}}{V_g} \approx \frac{2\pi \times 7.5a}{1.34a/T} \approx 35T$. The packet does spread somewhat, as several modes are occupied.

Fig. 4.5(b) shows the result of running the steps of the model (Fig. 4.1) in reverse. Here one finds that the edge state wave packet moves with the opposite chirality. By contrast, if the packet is initialized away from the boundary (Fig. 4.5(c)) it undergoes dynamics in which it sequentially expands and contracts.

For these calculations we used a large grid extending in both the x and y directions with open boundary conditions. We verified that the edge of our grid did not affect our results.

4.3 Experimental Implementation

One can implement this model experimentally using an optical lattice driven with time-dependent phases and amplitudes. In particular, we envision a po-

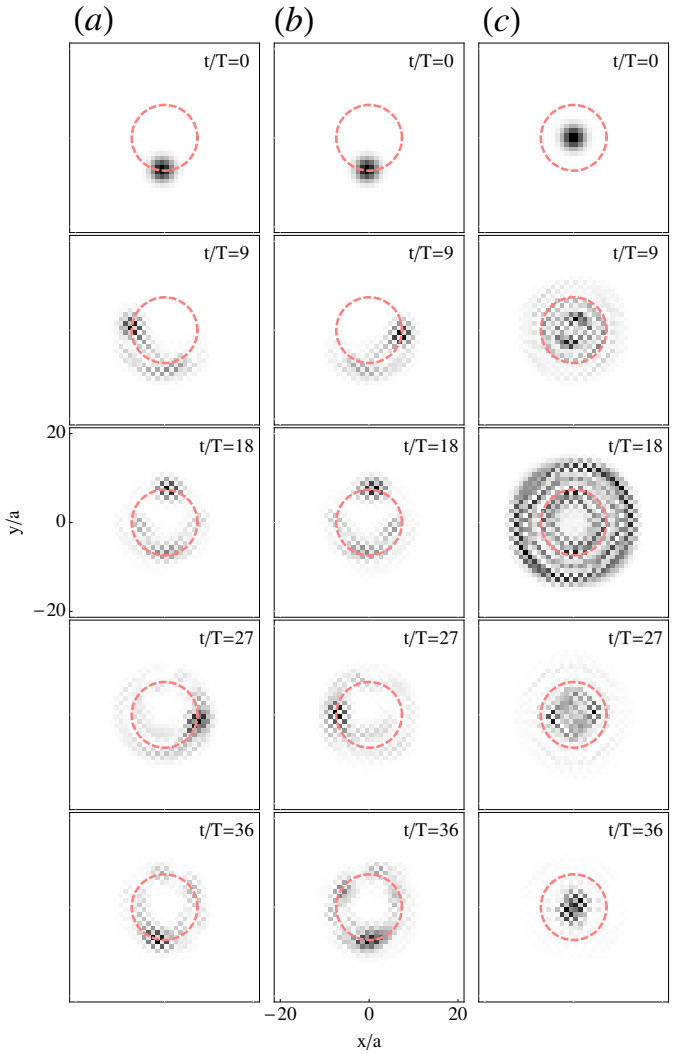

Figure 4.5: Real space density showing chiral edge modes. Darker colors represent higher density. Column (a) shows the dynamics resulting from the experimental protocol described in Sec. 4.2-B with spatially dependent hopping $J(x,y)T = 2\pi \exp[-12\frac{(x-L/2)^2+(y-L/2)^2}{L^2}]$ where $L = 40a$. At time $t = 0$ a condensate is placed in the lattice. A wavepacket moves in the clockwise direction along the circular boundary separating two topologically distinct regions (dashed red line). Column (b) shows the dynamics resulting from running the steps shown in Fig. 4.1 in reverse. The edge state wave packet now moves in the counterclockwise direction. Column (c) shows the dynamics resulting after initializing a wave packet away from the circular boundary. In this case there is no observable edge-state propagation.

tential of the form

$$\begin{aligned} V(x,y,t) &= A(\sin^2(k_{L_1}x) + \sin^2(k_{L_1}y)) \\ &-C(x,y,t)\times(\sin^2[\frac{k_{L_1}}{2}(x+y+\phi_1(t))] + \sin^2[\frac{k_{L_1}}{2}(x-y+\phi_2(t))]) \end{aligned} \tag{4.11}$$

where $C(x,y,t) = C(x,y)$ for steps $1-4$ and $C(x,y,t) = 0$ for step 5. This fifth step can be omitted, if desired. $\phi_1(t) = +\pi/2$ for steps 1 and 2 and $\phi_1(t) = -\pi/2$ for steps 3 and 4; $\phi_2(t) = +\pi/2$ for steps 1 and 4 and $\phi_2(t) = -\pi/2$ for steps 2 and 3. This potential is illustrated in Fig. 4.1 for spatially uniform C. If A is sufficiently large, hopping only occurs between neighboring pairs of sites. The spatially dependent $C(x,y,t)$–which generically decreases away from the center as described below– implies that the hopping is stronger at the center than the edge as in Fig. 4.3(a). Additionally, a deep lattice along the z-direction restricts motion to two dimensions.

One can create the first term of Eq. 4.11 with two independent sets of counter propagating lasers. The second term in Eq. 4.11 is created with two sets of *red-detuned* lasers with wave-vectors $\vec{k}_{L_2} = (\frac{k_{L_1}}{2}, \pm\frac{k_{L_1}}{2}, q)$. The resulting potential in the x-y plane does not depend on q, but allowing such a term gives additional design flexibility. By modulating the amplitudes and phases of the lasers one would control the the time-dependence of C, ϕ_1, and ϕ_2. The finite beam waists of these lasers naturally yield a profile $C(x,y) \approx \exp(-(x^2+y^2)/2\sigma^2)$. With this spatial dependence the barrier between neighboring lattice points is maximally reduced at $(x,y) = (0,0)$ but grows as x and y increase, similar to Fig. 4.3(a). The spatial variation of the hopping parameter can further be controlled by changing the profile of the laser [72].

4.4 Conclusions

We have proposed an experiment that realizes a Floquet topological insulator in an optical lattice, and we have demonstrated an experimental protocol that allows for the direct observation of topologically protected edge states. Using numerical simulations, we have shown that by imaging the evolution of a wavepacket, chiral edge states can be observed at the boundary between two distinct topological phases. Our proposal provides a simple and direct way to realize and probe topologically ordered quantum states using ultracold atoms.

CHAPTER 5

QUASIPARTICLE DISPERSIONS AND LIFETIMES IN THE NORMAL STATE OF THE BCS-BEC CROSSOVER

The work discussed in this chapter was originally published as *Quasiparticle dispersions and lifetimes in the normal state of the BCS-BEC crossover* by M. D. Reichl and E. J. Mueller, Physical Review A **91** 043627 (2015).

Interacting degenerate Fermi gases have attracted continued interest since their experimental realization over a decade ago [46]. Below a critical temperature T_c these gases exhibit a superfluid state which can be continuously tuned via Feshbach resonances [38] from a BCS state of Cooper pairs, to a BEC state of tightly bound bosonic molecules [138]. While the physics of the superfluid phase in this BCS-BEC crossover is well established [180], much less is known about the normal phase at temperatures above T_c.

One theme that has emerged from theoretical and experimental investigations at $T > T_c$ is the idea of a "pseudogap" phase in the middle of the crossover, where the density of states at the Fermi energy is suppressed due to strong many-body pairing effects. If and how this phase emerges in the BEC-BCS crossover has long been a source of experimental and theoretical investigation (see Ref. [36] for a comprehensive review). More recently, there has been interest [65, 122, 129, 144, 52] in a related question: How does Fermi-liquid theory [22], which is expected to be valid in in the BCS regime, break down when crossing over to the BEC regime where the normal phase is a gas of weakly interacting bosons? There has been some disagreement in the conclusions drawn from experiments which use radio-frequency (RF) spectroscopy to probe the single particle spectral density in harmonically trapped systems. The observed

RF spectrum in the crossover region seems to be well described by both Fermi-liquid theory [122] and theories displaying a pseudogap phase [65, 129]. A more recent experiment [144] probed the spectral density in a nearly *homogenous* system which avoids the density inhomogeneity of the trapped systems that can obscure features in the RF spectrum [6]. This experiment found evidence that the well defined quasi-particles one expects from Fermi-liquid theory become absent as the interactions are tuned from the BCS to the BEC side.

In this chapter we address this problem theoretically by computing the single particle spectral density within a T-matrix approximation as a function of interaction strength. We find near unitarity that the quasiparticles represented by peaks in the spectral density have short lifetimes at the Fermi-wavevector. We also find that an effective Fermi-wavevector extracted from the shape of the quasiparticle dispersions vanishes when one moves sufficiently deep into the BEC regime. Both of these observations point toward a breakdown in the Fermi-liquid description of the normal phase in which there is a well-defined Fermi surface and long-lived quasiparticles at the Fermi-wavevector. Previous theoretical works using related T-matrix approximations have similarly discussed the shape and widths of peaks in the spectral density [130, 165, 126]. Much of that work focused on the BEC regime [130] or on the temperature dependence of the spectral density at a few discrete values of the interaction strength [165, 126]. We extend these results and systematically explore the dependence of the spectral density on interaction strength.

This chapter is organized as follows. In Sec. 5.1 we discuss the T-matrix approximation in detail. In Sec. 5.2 we show numerical results for the spectral densities and describe our procedure for analyzing the quasiparticle dispersions

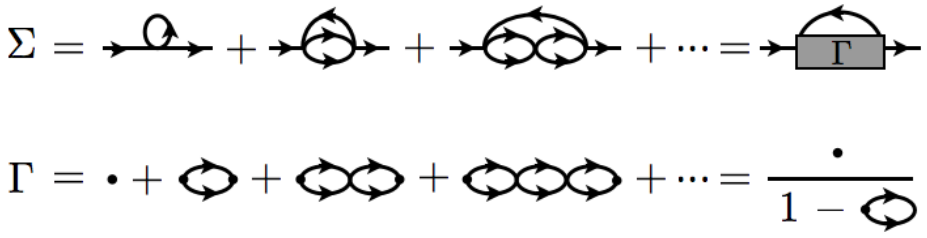

Figure 5.1: Diagrammatic representation of the T-matrix approximation used in this chapter (Eq. (5.1)).

and lifetimes. In Sec. 5.3 we discuss our results and conclude.

5.1 T-Matrix Approximation

We use a non-self-consistent T-matrix approximation [130, 158], to calculate the single-particle self energy Σ:

$$\Sigma(\mathbf{q}, i\omega_n) = \frac{T}{V}\sum_{\mathbf{k}}\sum_{m}\Gamma(\mathbf{k}, i\Omega_m)G_0(\mathbf{q}-\mathbf{k}, i\Omega_m - i\omega_n)$$
$$\Gamma(\mathbf{q}, i\Omega_m)^{-1} = \frac{m}{4\pi a} - \frac{1}{V}\sum_{\mathbf{k}}\frac{m}{k^2} + \frac{T}{V}\sum_{\mathbf{k}}\sum_{n}G_0(\mathbf{q}-\mathbf{k}, i\Omega_m - i\omega_n)G_0(\mathbf{k}, i\omega_n) \quad (5.1)$$

where $\omega_n = (2n+1)\pi T$ and $\Omega_m = 2m\pi T$ (with integers m and n) are fermionic and bosonic Matsubara frequencies at temperature T. $G_0(\mathbf{k}, i\omega_n) = 1/(i\omega_n - \epsilon_{\mathbf{k}})$ denotes the bare single particle propagator. The density is given by

$$n \equiv \frac{k_F^3}{3\pi^2} = 2\frac{T}{V}\sum_{\mathbf{k}}\sum_{n}G(\mathbf{k}, i\omega_n) \quad (5.2)$$

where $G^{-1} = G_0^{-1} - \Sigma$. The critical temperature is set by a pairing instability condition (the Thouless criterion)

$$\Gamma^{-1}(\mathbf{q}=0, i\Omega_m = 0)|_{T=T_c} = 0 \quad (5.3)$$

The expressions in Eq. (5.1) are derived by summing the infinite subset of Feynman diagrams that include scattering processes occurring in the vacuum

two-body problem (this shown in Fig. 5.1). This approximation, which neglects interactions between *pairs* of fermions, nevertheless accurately models the physics in the weakly interacting BCS regime ($\frac{1}{k_F a} << -1$, where the normal phase is a Fermi-liquid) and in the strongly interacting BEC regime ($\frac{1}{k_F a} >> 1$, where the normal phase near T_c is a gas of free bosonic molecules of mass $2m$). In particular in the deep BCS regime, the Thouless criterion is equivalent to the expression for T_c from BCS theory; in the deep BEC regime, the Thouless criterion together with Eq. (5.2) yield the correct condensation temperature for a gas of non-interacting bosons [124].

In the crossover regime ($-1 < \frac{1}{k_F a} < 1$) this approximation is less well-controlled and there is no *a priori* reason to expect it to be accurate. However previous studies using *ab initio* techniques [110] and self-consistent T-matrix theories [75] (where the bare propagators in Eq. (5.1) are replaced by the fully dressed propagator G) produce results with similar qualitative features. Since we are mainly concerned with discussing the qualitative physics within this regime, we use the relatively simple approximation described by Eq. (5.1).

After performing the Matsubara sums in Eq. (5.1) and taking $i\omega_n \rightarrow \lim_{\delta \rightarrow 0} \omega + i\delta$ we arrive at the following expressions for the imaginary part of the self energy:

$$\mathrm{Im}\Sigma(\mathbf{q}, \omega) = \int \frac{d^3k}{(2\pi)^3} B(\mathbf{k} + \mathbf{q}, \omega + \epsilon_{\mathbf{k}})[f_B(\omega + \epsilon_{\mathbf{k}}) + f_F(\epsilon_{\mathbf{k}})] \tag{5.4}$$

where $f_F(\epsilon) = (\exp(\epsilon/T) + 1)^{-1}$, $f_B(\epsilon) = (\exp(\epsilon/T) - 1)^{-1}$, and

$$B(\mathbf{q}, \omega) = \mathrm{Im}\Gamma(\mathbf{q}, \omega) = \\ \mathrm{Im}\left[\frac{m}{4\pi a} + \int \frac{d^3k}{(2\pi)^3} \frac{f_F(\epsilon_{\mathbf{k}}) + f_F(\epsilon_{\mathbf{q}-\mathbf{k}}) - 1}{(\omega + i\delta) - \epsilon_{\mathbf{k}} - \epsilon_{\mathbf{q}-\mathbf{k}}} - \frac{m}{k^2}\right]^{-1} \tag{5.5}$$

with $\delta \to 0$. We numerically evaluate the integrals in Eqs. (5.4) and (5.5) and extract the real part of the retarded self energy using a Kramers-Kronig relation. The single particle spectral density $A(\mathbf{k}, \omega)$ is then given by

$$A(\mathbf{k}, \omega) = -2\mathrm{Im}G(\mathbf{k}, \omega) = \frac{-2\mathrm{Im}\Sigma(\mathbf{k}, \omega)}{[\omega - \epsilon_{\mathbf{k}} - \mathrm{Re}\Sigma(\mathbf{k}, \omega)]^2 + [\mathrm{Im}\Sigma(\mathbf{k}, \omega)]^2} \tag{5.6}$$

5.2 Results

5.2.1 Spectral Density

Fig. 5.2 shows the spectral density $A(\mathbf{k}, E)$ calculated for interaction strengths $-0.5 \lesssim \frac{1}{k_F a} \lesssim 0.5$ at temperatures $T = 1.1T_c$. This choice of temperature was motivated by recent experiments performed slightly above T_c [144]. In the weakly interacting BCS limit (for instance, the bottom right panel in Fig, 5.2) we observe a strong quadratically dispersing quasiparticle peak along with a faint peak at $E > 0, k < k_F$.

As the interactions become stronger we see two clearly identifiable quasiparticle dispersions, one with $E > 0$ and another with $E < 0$. These two branches are separated in energy by a depression (or "pseudogap" [165, 160, 37]) in the density of states centered at $E = 0, k = k_F$. Finally, for very strong interactions (the

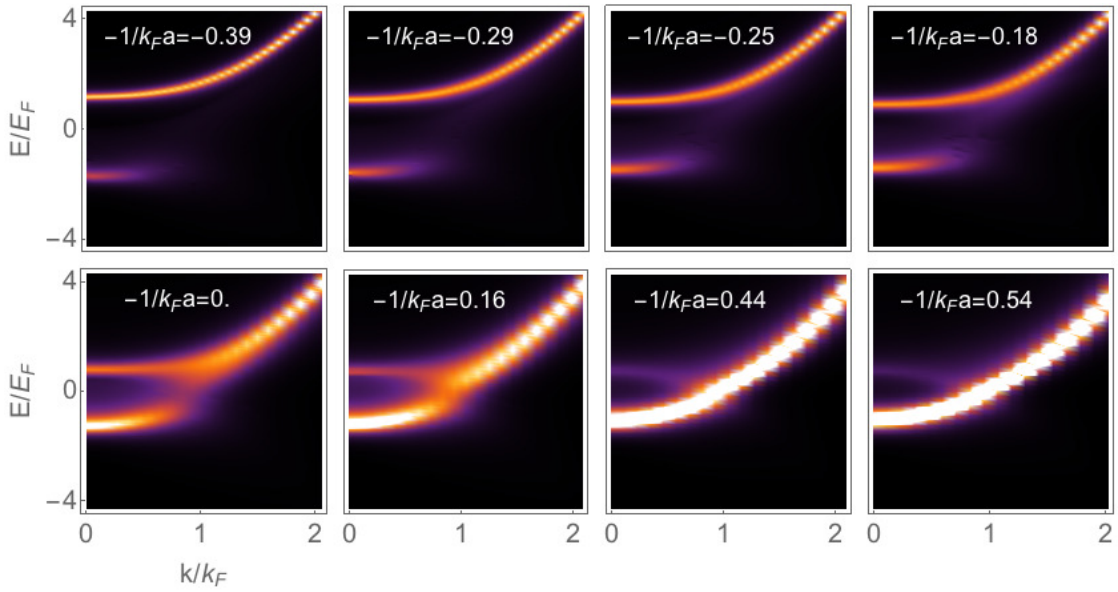

Figure 5.2: Spectral density in the normal phase for various interaction strengths at temperature $T = 1.1T_c$. Lighter colors correspond to higher spectral density.

top panels in Fig. 5.2) the two quasiparticle branches become further separated in energy and the spectral density is nearly fully suppressed near $E = 0, k = k_F$. Similar results calculated from various T-matrix approximations are shown in Refs. [165, 37, 126].

In the BCS regime there is a simple cartoon picture [118] of these results: One can add a fermion by either occupying a "normal" fermion particle state with dispersion $E \approx \epsilon_{\mathbf{k}}$ or by creating a "pair" of energy $E_{\text{pair}}(\mathbf{p})$ and annihilating a fermion with energy $\epsilon_{\mathbf{p}-\mathbf{k}}$. The latter excitations are broad as the pairs will be created with a range of $\mathbf{p}$. In this regime, the pair has vanishingly small energy $E_{\text{pair}}(0) \approx 0$, so we expect the "pair" peak to roughly track $E \approx -\epsilon_{\mathbf{k}}$. As the interactions are increased, there is hybridization between these two branches that produces a psuedogap analogous to the gap that is produced by the hybridization of particle and hole states in the superfluid phase. Finally in the BEC regime, $E_{\text{pair}} < 0$, which shifts the branch associated with pairs entirely

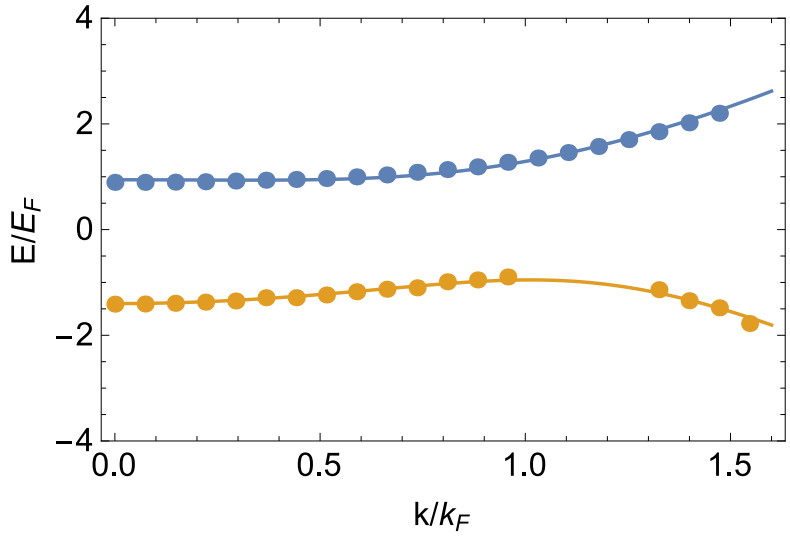

Figure 5.3: Peak locations of the spectral density at $1/k_F a = 0.18$ ($T = 1.1T_c$). The solid lines show least-squares fits to the dispersion relation in Eq. (5.7). The board and asymmetric nature of the peaks prevents us from determining the lower branch dispersion in the range $1.0k_F \lesssim k \lesssim 1.25k_F$.

to negative energies; the positive energy branch in this regime corresponds to adding one "normal" fermion to a sea of paired fermions for all k.

5.2.2 Quasiparticle Dispersions and Lifetimes

To describe the qualitative features of the quasiparticle dispersions, we fit the peaks in the spectral density to a phenomenological model obtained from the dispersion relations expected in the superfluid phase:

$$E_{\text{peak}}(k)_{\pm} = \pm\sqrt{\frac{1}{2m}(k - k_{L_{\pm}})^2 + \Delta_{\pm}^2} \tag{5.7}$$

where $E_{\text{peak}}(k)_{\pm}$ are the peak locations as a function of momentum for the positive and negative energy branches. $\Delta_{\pm}$ parametrizes the magnitude of the psuedo-gap energy scale, and $k_{L_{\pm}}$ parametrizes the location of the effective Fermi-wavevector. Note that k_L (called the "Luttinger-wavevector" in Refs.

[129, 126]) may not equal k_F as defined in Eq. (5.2). An example of such a fit is shown in Fig. 5.3 (where $1/k_F a = 0.18$, $\Delta_- = 0.95E_F$, $\Delta_+ = 0.94E_F$, $k_{L_-} = 1.01k_F$, and $k_{L_+} = 0.34k_F$).

Fits like these have been performed in previous work in the BEC regime [130] and for a few select values of the interaction strength at different temperatures [126]. Here we focus on the dependence of the fit parameters on interaction strength and perform fits for a number of different values of $1/k_F a$ in the crossover regime. Similar strategies have been used to capture the qualitative features of experimental data for harmonically trapped fermions [129, 166].

Figs. 5.4 and 5.5 show the fitting parameters $\Delta_\pm$ and $k_{L_\pm}$, respectively, as a function of interaction strength. Each point was exacted by performing a least squares minimization of the difference between Eq. (5.7) and the location of the quasiparticle peaks in the spectral densities in Fig. 5.2. The psuedogap scale is maximal on the BEC side of resonance, smoothly dropping as one approaches the BCS side. These parameters are determined by a global fit, so they are sensitive not only to features near the Fermi wave-vector, but to all k. While k_{L_+} and k_{L_-} are generically quite different, we find $\Delta_+ \approx \Delta_-$.

To estimate the lifetimes of the quasiparticles we extract the widths of the spectral peaks at $k = k_F$ by fitting the peaks in the function $A(k = k_F, E)$ to Lorentzian functions. Fig. 5.7 shows an example of such a fit for $\frac{1}{k_F a} = 0.18$. Fig. 5.6 shows the quasiparticle widths τ^{-1} as a function of interaction strength. We note that for $\frac{1}{k_F a} < 0$ the negative energy branch cannot clearly be separated from the positive energy branch at $k = k_F$; for these interaction strengths we only plot one value of the quasiparticle lifetime.

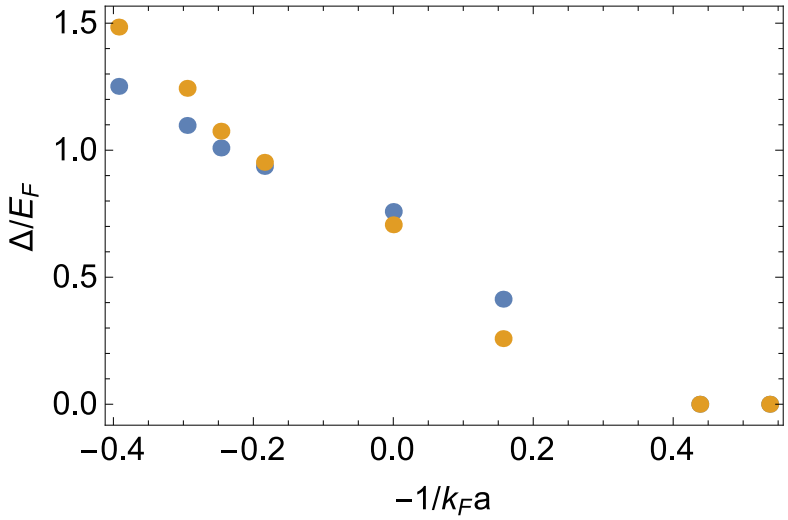

Figure 5.4: Pseudogap energy scale Δ_- (orange) and Δ_+ (blue) extracted from fits of Eq. (5.7) to the peak locations in the spectral density ($T = 1.1T_c$).

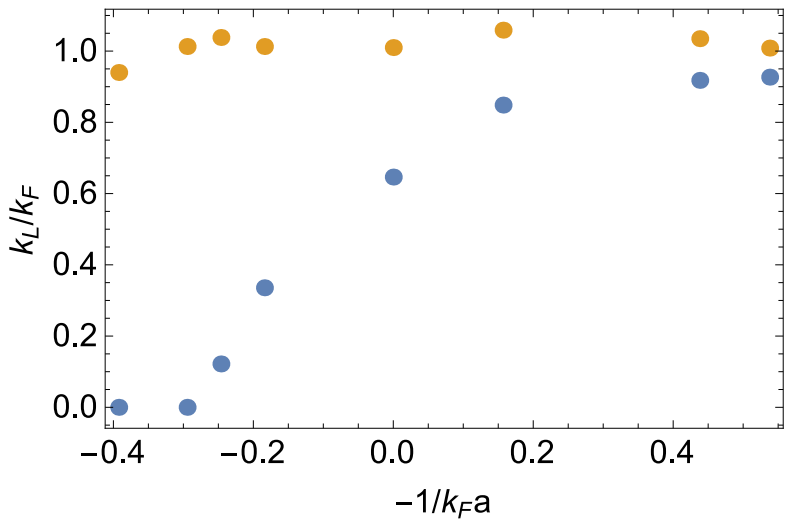

Figure 5.5: Effective Fermi-wave vectors k_{L_-} (orange) and k_{L_+} (blue) extracted from fits of Eq. (5.7) to the peak locations in the spectral density ($T = 1.1T_c$).

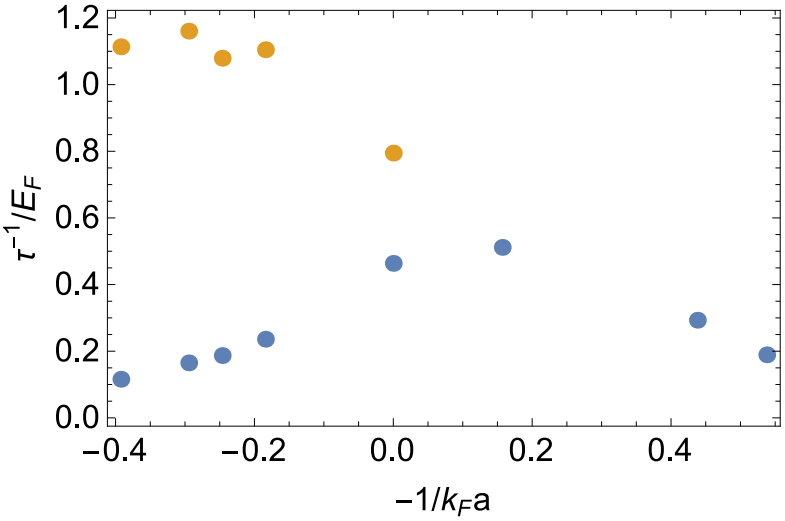

Figure 5.6: Inverse quasi particle lifetimes τ^{-1} as a function of interaction strength ($T = 1.1T_c$). The orange (blue) points are the spectral widths of the negative (positive) energy branch of the quasiparticle spectral peak at $k = k_F$.

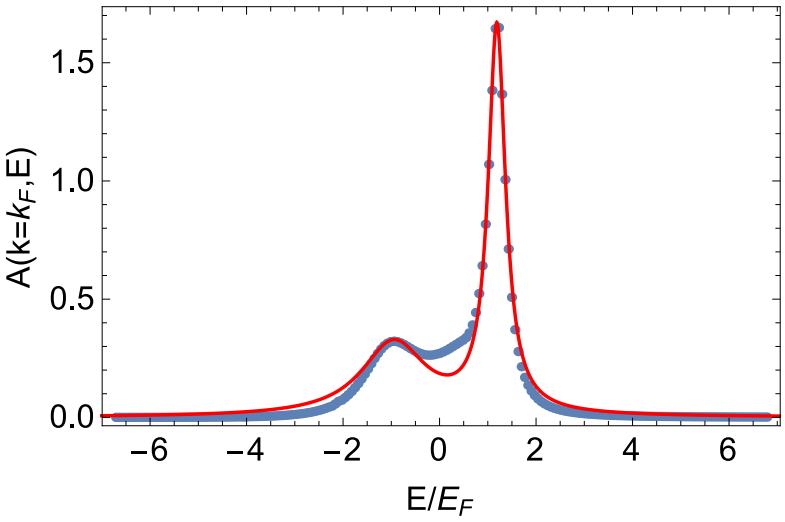

Figure 5.7: $A(k = k_F, E)$ at $\frac{1}{k_F a} = 0.18$ ($T = 1.1T_c$). The solid red line is a fit of the data to the sum of two Lorenzians. The two widths extracted from these fits provide estimates of the inverse quasi-particle lifetimes τ^{-1}. τ^{-1} at other interaction strengths are plotted in Fig. 5.6.

5.3 Discussion and Conclusions

Our results demonstrate a breakdown of Fermi-liquid theory in two key respects. First, as shown in Fig. 5.6, the inverse lifetimes of the quasi-particles at k_F increase as one approaches unitarity from the BCS-side and eventually reaches a maximum of value on the order of E_F. Fermi-liquid theory is predicated on a vanishingly small inverse lifetime at the Fermi-surface. This breakdown is due to both the high temperature and the strong interactions.

Second, the effective Fermi-wavevector k_L, which helps identify the presence of a remnant Fermi surface [129, 126], vanishes for the upper branch at $\frac{1}{k_F a} \approx 0.3$ (see Fig. 5.5). We note that the effective Fermi-wavevector for the bottom branch (k_{L_-}) remains fixed at k_F for the range of interaction strengths shown in Fig. 5.5). However, other studies have shown that at higher interaction strengths ($\frac{1}{k_F a} \approx 0.7$), k_{L_-} vanishes as well [129]. k_{L_-} and k_{L_+} are associated with different branches of excitations and therefore have distinct physical interpretations. k_{L_+} is associated with particle excitations, while k_{L_-} is associated with holes. On the BEC side of resonance, one can add a fermion without disturbing the pairs, but adding a hole requires breaking pairs. Thus many-body effects are less important for particles, and k_{L_+} vanishes in a regime where k_{L_-} is still essentially equal to k_F.

A recent experiment [144] used RF spectroscopy to probe the spectral density of a nearly homogenous Fermi gas in the normal phase as a function of interaction strength. The RF signal reported in this work came primarily from the negative energy branch of the single particle excitations since any signal from positive energy excitations is suppressed by a Fermi factor. The authors

fit their data to a two-mode model with a narrow quadratically dispersing peak expected from a Fermi-liquid theory (with weight $Z \leq 1$) and a broad "incoherent background" (with weight $(1 - Z)$) corresponding to the spectral weight of weakly interacting bosonic molecules in the normal phase. They find that the best fit to their data at interaction strengths $\frac{1}{k_f a} \gtrsim 0.3$ has $Z \approx 0$. The authors conclude that this is a signal of a breakdown in the Fermi-liquid description of their data.

We caution however that because their two mode fit was performed on a single broad dispersing peak (coming from the negative energy branch of excitations), it is somewhat difficult to interpret the meaning of this vanishing Fermi-liquid contribution. Moreover, good fits to the data came at the expense of some unrealistic values of the fitting parameters. In particular, the parameter corresponding to the temperature of the incoherent bosonic contribution had best fit values nearly four times greater than the estimated temperature of the gas.

One possible interpretation of this two-mode fitting procedure is that Z roughly measures the weight of the component of the RF signal which disperses as $E \sim k^2$. Assuming that the peaks of the RF data are well described by the BCS-like dispersion $E_{\text{peak}}(k)_-$ given in Eq. (5.7), the quadratically dispersing component vanishes when $k_{L_-} \to 0$. The vanishing of Z in the two-mode model then seems to roughly correspond to the vanishing of k_{L_-} that occurs as one approaches the BEC regime. We recommend fitting the peaks of the RF data to the BCS dispersion relations in Eq. (5.7) to directly extract k_{L_-} and to compare the experimental results with our T-matrix calculations.

Given the high temperatures and strong interactions in the normal state near

unitarity, it is not surprising that many of the features expected of a Fermi liquid are absent. It appears that the T-matrix approximation captures this physics. It remains to be seen if an alternative framework can replace these Fermi-liquid ideas. The most tantalizing steps in that direction come from exploring universal bounds on transport coefficients [3].

CHAPTER 6

DYNAMICS OF PATTERN-LOADED FERMIONS IN BICHROMATIC OPTICAL LATTICES

The work discussed in this chapter was originally published as *Dynamics of pattern-loaded fermions in bichromatic optical lattices* by M. D. Reichl and E. J. Mueller, Physical Review A **93** 031601(R) (2016).

An important challenge in many-body physics is to understand how interactions and disorder influence the transport properties of an electron gas. The non-interacting disordered problem was largely solved by Anderson [10, 2]. By studying the expansion dynamics of wave packets of weakly interacting atoms, cold atom experiments have found evidence for Anderson localization in 1D [25] and 3D [94, 84] random speckled potentials and in 1D quasi random optical superlattices [140]. More recently, attention has turned to the interacting problem [153, 18, 58, 71, 19, 55, 161, 82, 150, 151, 80, 170, 5, 103, 117, 172, 121, 59, 48]. Schreiber et. al [147] devised an ingenious experiment to test these ideas. Here we model that experiment.

The experiment in Ref. [147] uses lasers to create a one-dimensional lattice with a weak periodic superlattice that is incommensurate with the main lattice (see the inset in Fig. 6.1). The resulting quasi-periodic potential shares features with a disordered one. For example, when the potential is sufficiently strong, all single particle states are localized. The experimentalists load interacting spin-1/2 fermions into some of the odd sites of the lattice, leaving the even sites empty. Some odd sites are doubly occupied. The atoms hop and interact for

time t. The experimentalists measure the sublattice imbalance $I(t)$

$$I(t) = \frac{N_{\text{odd}} - N_{\text{even}}}{N_{\text{odd}} + N_{\text{even}}} \tag{6.1}$$

where $N_{\text{odd/even}}$ is the number of fermions on odd/even sites at time t. In a localized phase, the atoms do not travel far from their initial position, and have a relatively high probability of being found at their starting point. Consequently in such a phase, one expects $I(t)$ to be non-zero at long times. Conversely, in a delocalized phase, one might expect $I(t)$ to decay to zero at long times. The experiment explores the long time behavior of I as a function of superlattice strength and the interaction strength. The initial configuration of fermions on odd sites is random and the measurements are the result of ensemble averages over initial states. The experimentalists find two phases: one in which I decays to zero, the other in which it is finite. The boundary appears to depend on the interactions in a non-monotonic manner.

In this chapter we model the experiment, addressing the fundamental question of the interplay of incommensurate potentials and interactions. We develop a low-density cluster expansion which expresses the ensemble averaged imbalance as the sum of terms which involve only single-particle and two-particle dynamics. Using this computationally efficient approximation, we numerically calculate the long time imbalance as a function of interaction strength and superlattice strength. Our calculations reproduce the experimental results and provide insight into localization in the interacting system. We also extend our method to the case of a two dimensional lattice with an incommensurate superlattice in only one direction. The extra transverse degrees of freedom give kinetic pathways for equilibration; we calculate the consequences.

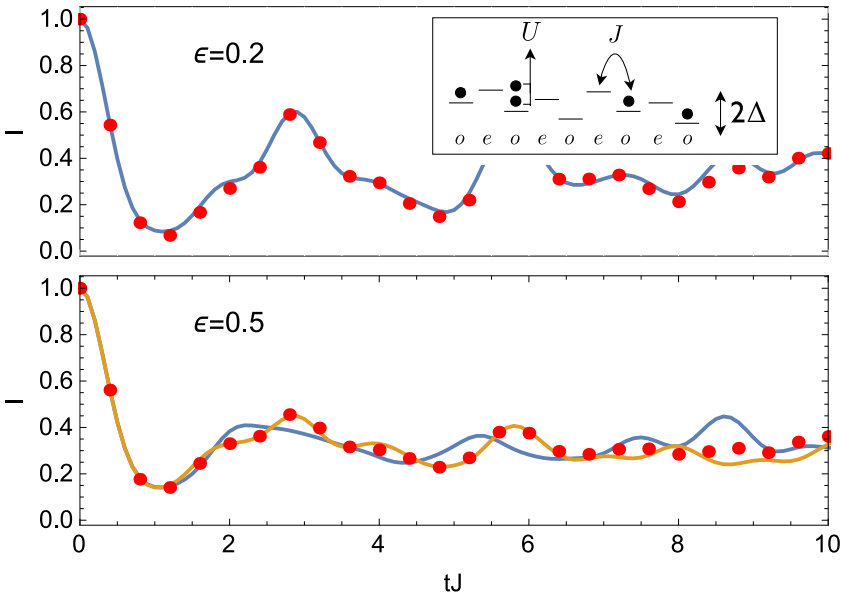

Figure 6.1: Imbalance $I = \frac{N_{\text{odd}} - N_{\text{even}}}{N_{\text{odd}} + N_{\text{even}}}$ vs time t, measured in units of the nearest-neighbor hopping strength J for fermions in an incommensurate superlattice of strength Δ. $N_{\text{odd/even}}$ is the number of fermions on odd/even sites. The inset shows the geometry. At time $t = 0$, $I = 1$. The dark (blue) curves show the result of keeping the first two terms in the cluster expansion in Eq. (6.6) for 20 sites. The light (orange) curve shows the result of including three-particle terms in the cluster expansion. Red dots correspond to a time-dependent DMRG simulation. Here $\Delta = 3J$, $U = 3J$, the superlattice period $\beta^{-1} = (0.721)^{-1}$ and the superlattice phase $\phi = 0$. The density is $\epsilon = 0.2$ in the top graph and $\epsilon = 0.5$ in the bottom graph.

6.1 Model and Methods

We model the atomic dynamics via the interacting Aubry-Andre model, given by the Hamiltonian [17, 82]

$$H = -J \sum_{i,\sigma} \left(c^{\dagger}_{i,\sigma} c_{i+1,\sigma} + \text{h.c} \right) + \Delta \sum_{i,\sigma} \cos(2\pi\beta i + \phi) c^{\dagger}_{i,\sigma} c_{i,\sigma} + U \sum_{i} n_{i,\uparrow} n_{i,\downarrow} \tag{6.2}$$

The first term describes nearest neighbor tunneling with strength J while the second term describes a periodic superlattice potential of strength Δ. For nearly all irrational values of β, this potential functions as quasi-random disorder which localizes all single particle states for sufficiently large superlattice

strength ($\Delta/J > 2$) [17]. In this regime, and for infinitely large systems, the single particle states are localized with a localization length $\lambda = (2\log\frac{\Delta}{2J})^{-1}$, independent of β [17, 155]. If $\beta = p/q$ is rational, the eigenstates are extended Bloch waves with period q. For large Δ and large q, the wavefunction in each unit cell is sharply peaked, and locally the eigenstates are similar to the irrational case.

The localization transition is reflected in the observable $I(t)$, which for typical irrational β and $U = 0$ relaxes to 0 for $\Delta/J < 2$ but remains finite at long times for $\Delta/J > 2$ (see the inset in Fig. 6.2). We define $I_\infty = I(t \to \infty)$. Although $I_\infty \to 0$ as $\Delta/J \to 2$, the way it vanishes depends strongly on β and is inconsistent with the naive estimate from structureless exponentially localized states $I_{\text{est}} \sim 1/\lambda^2$ (see Ref. [147], supplementary material). The graph of I_∞ vs. β and Δ/J is fractal (see Fig. A1 in Appendix A), as it has different behaviors for rational and irrational β. Despite this complexity, the long time behavior of I is distinct in the localized and delocalized phase: $I(t)$ captures the localization transition, but also probes features of the single-particle wave functions beyond the localization length.

The third term in Eq. (6.2) describes on-site interactions of strength U. Here we develop a low-density expansion to calculate the imbalance in the presence of interactions.

We define $\langle I(t)\rangle$ to be the expectation value of the imbalance, averaged over the ensemble of initial states,

$$\langle I(t)\rangle = \frac{1}{Z}\sum_{n=1}^{N_s}\sum_{\{n\}} W(\{n\}) \times \frac{1}{n}\langle\{n\}|\hat{n}_I(t)|\{n\}\rangle \tag{6.3}$$

Here $\{n\} = \{i_1\sigma_1, i_2\sigma_2, ..., i_n\sigma_n\}$ labels an n-particle initial state with particles at sites i with spin σ, $\sum_{\{n\}}$ denotes a sum over the i_j's and σ_j's, $W(\{n\})$ is the weight of a given n particle state, $Z = \sum_{\{n\}} W(\{n\})$, and $\hat{n}_I(t) = e^{iHt}(\hat{N}_{\text{odd}} - \hat{N}_{\text{even}})e^{-iHt}$ where $\hat{N}_{\text{odd/even}}$ are the number operators (for both spins) on odd/even sites.

To model the experiment, we take $W(\{n\}) = 0$ if any of the particles are on even sites. We take the initial occupation of each odd site to be an independent random variable, and hence $W(\{n\}) = \epsilon^n(1-\epsilon)^{N_s-n}$, where N_s is the number of sites. Our method is readily generalized to more sophisticated weights. For instance, as shown in Eq. (A.12) in Appendix A, we can weight the initial states with separate probabilities for sites with two atoms (doublons) or one atom (singlons) (see also Fig. 6.3).

With this choice of W, the normalization is $Z = 1-(1-\epsilon)^{N_s}$ which approaches 1 in the $N_s \to \infty$ limit. In that same limit, the mean density (the number of particles per site averaged over the ensemble of initial states) is ϵ .

Substituting our weight function into Eq. (6.3) yields an expression for the imbalance as a sum of terms involving different numbers of particles:

$$\begin{aligned}\langle I(t)\rangle =& \frac{1}{Z}\Big[\epsilon(1-\epsilon)^{N_s-1}\sum_{\{1\}}{}'C_{\{1\}}(t) + \frac{\epsilon^2}{2}(1-\epsilon)^{N_s-2}\sum_{\{2\}}{}'C_{\{2\}}(t) + \\ & \frac{\epsilon^3}{3}(1-\epsilon)^{N_s-3}\sum_{\{3\}}{}'C_{\{3\}}(t) + ... + \frac{\epsilon^{N_s}}{N_s}\sum_{\{N_s\}}{}'C_{\{N_s\}}(t)\Big]\end{aligned} \tag{6.4}$$

where $C_{\{n\}}(t) = \langle\{n\}|\hat{n}_I(t)|\{n\}\rangle$, and the primes on the sums mean they only include odd sites.

We wish to resum this series, taking advantage of the fact that well-separated particles will move independently. Somewhat analogous to cumulants, we define functions $\widetilde{C}_{\{n\}}(t)$ via

$$C_{\{n\}}(t) = \widetilde{C}_{\{n\}}(t) + \sum_{\langle\{1\}\in\{n\}\rangle} C_{\{1\}}(t) + \sum_{\langle\{2\}\in\{n\}\rangle}\widetilde{C}_{\{2\}}(t) + \sum_{\langle\{3\}\in\{n\}\rangle}\widetilde{C}_{\{3\}}(t) + ... + \sum_{\langle\{n-1\}\in\{n\}\rangle}\widetilde{C}_{\{n-1\}}(t) \tag{6.5}$$

where $\sum_{\langle\{k\}\in\{n\}\rangle}$ denotes a sum over all $\binom{n}{k}$ combinations of k site and spin labels in $\{n\}$. We set $\widetilde{C}_{\{1\}}(t) = C_{\{1\}}(t)$. These new functions $\widetilde{C}_{\{k\}}(t)$ extract the k-body

dynamics from the original functions $C_{\{k\}}(t)$. First instance, the two particle term $\widetilde{C}_{\{i_1\sigma_1,i_2\sigma_2\}}(t) = C_{\{i_1\sigma_1,i_2\sigma_2\}}(t) - C_{\{i_1\sigma_1\}}(t) - C_{\{i_2\sigma_2\}}(t)$ is the difference between a term representing the exact dynamics of two particles with initial positions and spins $i_1\sigma_1$ and $i_2\sigma_2$ and the single particle dynamics of a particle initialized at site i_1 and another particle initialized at site i_2. In the non-interacting limit $U = 0$, we only have single particle dynamics and $\widetilde{C}_{\{k\}}(t) = 0$ for all $k > 1$. In a diagrammatic formulation, $\widetilde{C}$ involves only connected diagrams.

Substituting Eq. (6.5) into Eq. (6.4), and using the arguments in Appendix A gives

$$\langle I(t)\rangle = \frac{1}{N_s}\sum_{\{1\}}{}'\widetilde{C}_{\{1\}}(t) + \frac{\epsilon}{N_s}\sum_{\{2\}}{}'\widetilde{C}_{\{2\}}(t) + O(\epsilon^2) \tag{6.6}$$

in the $N_s \to \infty$ limit. For our numerical calculations we include the finite size corrections in Eq. (A.7) in Appendix A.

Equation (6.6) expresses the n-particle time dependent observable $\langle I(t)\rangle$ explicitly as the sum of 1-particle terms ($\widetilde{C}_{\{1\}}(t)$), 2-particle terms ($\widetilde{C}_{\{2\}}(t)$), etc. The first sum in Eq. (6.6) contains N_s terms. The second sum contains $O(N_s^2)$ terms, but when the two particles are farther apart than some length scale ξ, where ξ is the smaller of the one-particle localization length λ and the ballistic length $l = Jt$, the particles are effectively non-interacting and $\widetilde{C}_{\{2\}}$ will vanish. Therefore only ξN_s terms contribute to the sum. Similarly, there are only $O(\xi^2 N_s)$ which contribute in the sum over $\widetilde{C}_{\{3\}}$ terms.

Each subsequent term in Eq. (6.6) is intensive and is weighted by a coefficient of the order ϵ^{n-1} (the density exponentiated to the number of particles in the cluster minus 1). This cluster expansion is a non-equilibrium analogue to the virial expansion in statistical physics [88]. When the localization length is

greater than the system size ($\lambda > N_s$) the series is only guaranteed to converge for short times $l = Jt \lesssim 1/\epsilon$. Therefore, for calculations of the long-time behavior of the imbalance, we focus our attention on the localized regime $\Delta/J > 2$.

For most of the results in this chapter we only keep the first two terms in Eq. (6.6). Remarkably, this approximation, which only involves calculating the dynamics of one or two particles, shows all the features seen in the experiments of Ref. [147].

6.2 Numerical Results

Figure 6.1 shows typical $\langle I(t) \rangle$ for interacting fermions in the localized regime. The solid blue curves show calculations using the first two terms in the cluster expansion in Eq. (6.6). The imbalance initially has a value $I(t = 0) = 1$, reflecting the fact that the initial states have particles localized only on odd sites. At long times, the imbalance saturates to a non-zero value with small fluctuations about the mean. For comparison, the red dots show calculations using time-dependent density matrix renormalization group (t-DMRG) [173, 174]. For the DMRG calculations, we average over 100 initial states drawn from the probability distribution $W(\{n\})$. The cluster expansion and the t-DMRG show excellent agreement at the smaller density $\epsilon = 0.2$. At the larger density $\epsilon = 0.5$ there is some small quantitative disagreement, but the average long-time imbalance is nearly identical for the two approaches. As a test of the convergence of the cluster expansion, we have also computed the contribution from three-particle terms (orange curve in Fig. 6.1). Including these terms gives small corrections to the two-particle calculation and yields better agreement with t-DMRG.

Figure 6.2 shows the long time imbalance I_∞ as a function of interaction strength for a series of superlattice strengths. We compute $\langle I(t)\rangle_{\text{init}}$ by numerically evaluating the first two terms of Eq. (6.6) at a density $\epsilon = 0.2$. Each data point in Fig. 6.2 represents $\langle I(t)\rangle$ averaged over the times $200 < tJ < 500$ and averaged over twelve values of the superlattice potential phase ϕ evenly spaced in the range $[0, \pi]$. All simulations were performed on a lattice with 20 sites using open boundary conditions. We have explicitly verified that finite size effects are negligible; the system size was chosen for numerical convenience.

Each curve is symmetric under $U \to -U$. As pointed out in Ref. [146] this symmetry is expected for time-reversal invariant operators such as $I(t)$, as long as the initial states are localized in space. For $|U/J| \lesssim 2\Delta$, interactions cause some 2-particle scattering states to become less localized than 1-particle states, and the long time imbalance decreases with increasing interaction strength. For larger interactions, the imbalance begins to increase again and produces a "W" shape consistent with the re-entrant behavior predicted for similar systems [115]. The "W" is most pronounced for $\Delta/J \approx 3$.

At large interaction strengths, up-spin and down-spin particles initially localized at the same site (doublons) become bound and have a reduced effective tunneling rate $J_{\text{eff}} \approx J^2/U$ [18, 55]. The contribution to I_∞ from these doublons causes the long time imbalance at large interaction strengths to become greater than the long-time imbalance at $U = 0$.

We further explore the contribution of doublons to I_∞ by giving doublons and singlons separate weights in our average over initial states (see Eq. (A.12) in Appendix A). We let ϵ be the total density of particles and η the density of doublons. Fig. 6.3 shows I_∞ as a function of U/J at $\Delta/J = 3$ for three different

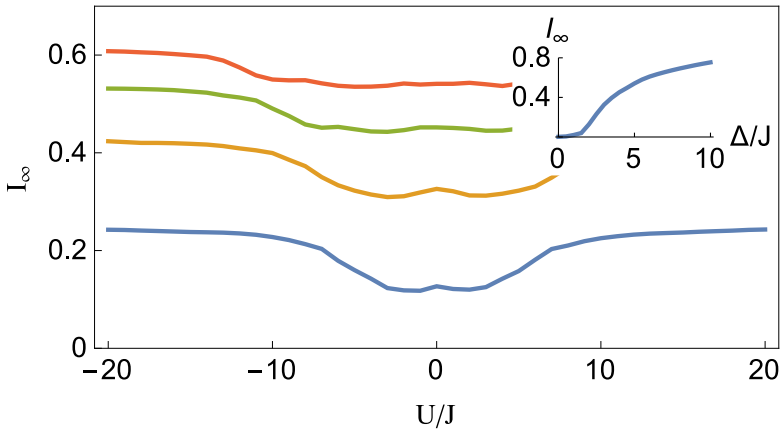

Figure 6.2: Long time density imbalance I_∞ as a function of interaction strength U/J for a one-dimensional lattice with 20 sites at density $\epsilon = 0.2$. The superlattice period is $\beta^{-1} = (0.721)^{-1}$ in units of the lattice spacing. The different curves correspond to different superlattice strengths: $\Delta/J = 2, 3, 4, 5$ (from bottom to top). The inset shows I as a function of superlattice strength for $U/J = 0$.

values of η/ϵ in the initial states of the system: 0 ($\epsilon = 0.5$), 0.23 ($\epsilon = 0.57$), and 0.5 ($\epsilon = 0.67$) for the bottom (blue), middle (orange), top (green) graphs, respectively. All other parameters are the same as in Figure 6.2. In the case where there are no doublons $I_\infty(U/J = 0) = I_\infty(U/J \to \infty)$. This is a reflection of the fact that the dynamics of singlons in the hard core $U/J \to \infty$ limit is identical to the dynamics of free spinless fermions [147]. As more doublons are added to the system, I_∞ at large U/J increases, as expected from the reduced tunneling rate of bound pairs. The blue and orange points in Fig. 6.3 show corresponding experimental results from Ref. [147], where the doublon density was controlled by varying the loading protocol.

We chose η and ϵ to best match the experimental data, finding excellent agreement. Our best-fit value of η is somewhat smaller than estimates in Ref. [147]. Similar discrepancies were seen in DMRG calculations [147].

Motivated by more recent experiments [26], and as a further demonstration

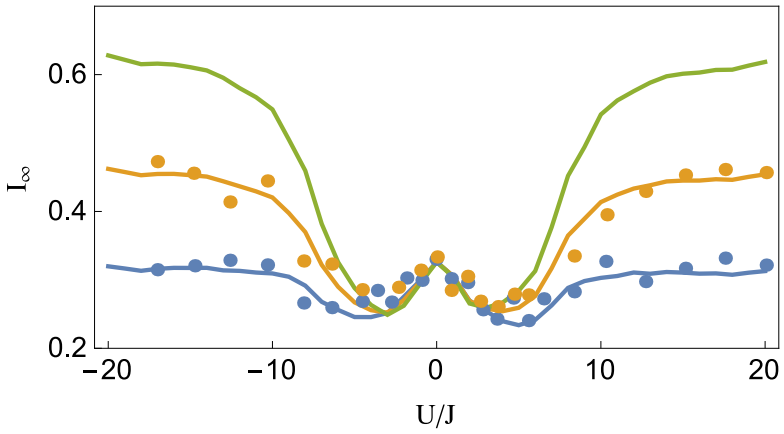

Figure 6.3: Long time density imbalance I_∞ as a function of interaction strength U/J for a one-dimensional lattice at superlattice strength $\Delta/J = 3$. The different curves show calculations using a cluster expansion on a 20 site lattice with different densities η of doublons in the ensemble of initial states: The bottom (blue), middle (orange), and top (green) curves correspond to a ratio of doublons to particles of $\eta/\epsilon = 0, 0.23, 0.5$, respectively. The blue and orange points are experimental measurements for a small doublon fraction ($\eta/\epsilon \approx 0.08$) and larger doublon fraction ($\eta/\epsilon \approx 0.5$), from Fig. 6 of Ref. [147], courtesy of Ulrich Schneider.

of our cluster method approach, we have extended our calculations to two-dimensional lattices. We consider a two-dimensional Hamiltonian with a one-dimensional superlattice potential $V = \Delta\cos(2\pi\beta i_x + \phi)$. As before, we take J to be the hopping in the x-direction and J_y the hopping in the y-direction. In this case we average over initial states where atoms are localized on odd sites in the x-direction and are in $k_y = 0$ momentum eigenstates in the y-direction. This choice of initial states, which requires periodic boundary conditions in the y-direction, was chosen purely for numerical simplicity; we expect no qualitative changes if we initialize with spatially localized states and use open boundary conditions in the y-direction. We once again use Eq. (6.6) including only one-particle and two-particle terms to compute the even-odd imbalance in the x-direction.

Because the eigenstates are inherently delocalized in this situation, we only expect our cluster expansion to be accurate for short times. Fig. 6.4 shows the

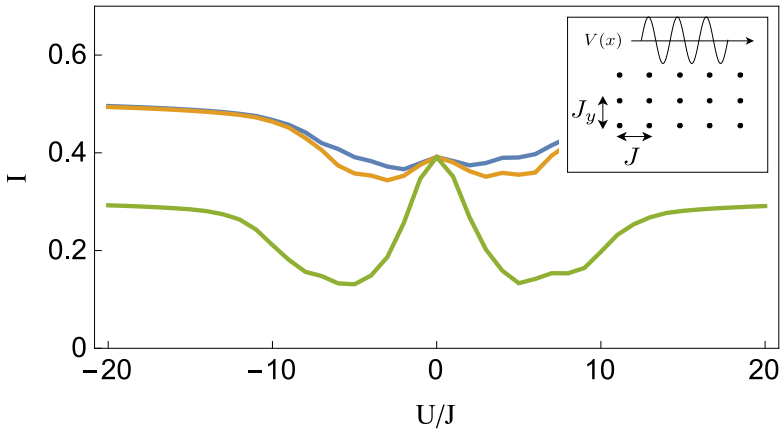

Figure 6.4: Density imbalance I averaged over time from $t = 5/J$ to $t = 10/J$ as a function of interaction strength U/J for a two-dimensional lattice with 10×10 sites at superlattice strength $\Delta/J = 3.0$ and density $\epsilon = 0.2$. The superlattice potential is only one-dimensional: $V(i_x, i_y) = \Delta \cos(2\pi\beta i_x + \phi)$. $J_y/J = 0, 0.1, 1$ for the top, middle, and bottom (blue, orange, green) curves, respectively. The inset shows a diagram of the setup.

imbalance I in the x-direction, averaged over times between $t = 5/J$ and $t = 10/J$ as a function of U/J. These simulations were performed on a lattice with 10×10 sites. Scattering in the y-direction (transverse to the superlattice potential) allows for the density imbalance to relax to smaller values, and I becomes suppressed as J_y is increased. Similar results are observed in Ref. [26].

6.3 Conclusion

In this chapter we have applied a new cluster expansion method to simulate experiments [147] which studied the non-equilibrium dynamics of fermions pattern-loaded in quasi-disordered one-dimensional lattices. Our calculations, which involve keeping the first two terms in the cluster expansion and account for only single particle and two particle dynamics, reproduce all experimental features of the long-time density imbalance between even and odd sites, and

agree quantitatively with simulations using t-DMRG. We have also extended our calculations to two-dimensional lattices, finding that the density imbalance is suppressed when adding hopping in the direction transverse to the superlattice potential.

Although principally designed to calculate the experimental observable, this cluster approach also gives some insight into many-body localization. For example we have shown that time dynamics of the many-body wave function in the localized phase can be written as a sum of 1-body, 2-body, ..., n-body terms. In the dilute limit, the dynamics are dominated by few-particle physics, a feature which was not previously recognized.

Our cluster approach can be also used to explicitly construct the local integrals of motion which underly the phenomenology of the many-body localized phase [150, 80, 35, 142]. As detailed below, we use the solution to the j-body problem to construct fermionic creation operators $a^{\dagger(j)}_{n\sigma}$ where $\{a^{(j)}_{n\sigma}, a^{\dagger(j)}_{m\tau}\} = \delta_{mn}\delta_{\tau\sigma}$. Our operators have the property that in the i-particle subspace, all of the $a^{\dagger(j)}_{n\sigma}$ are equivalent for $j \geq i$: $a^{\dagger(i)}_{n\sigma}P_i = a^{\dagger(j)}_{n\sigma}P_i$ where P_i projects into the i particle subspace. Our conserved quantities are manifest in the requirement

$$[a^{\dagger(i)}_{n\sigma}a^{(i)}_{n\sigma}, P_i H P_i] = 0 \tag{6.7}$$

If the $a^{\dagger(i)}_{n\sigma}$ are "local", we thereby complete the construction.

We take $a^{\dagger(1)}_{n\sigma}$ to create the single-particle eigenstate with spin σ and energy ϵ_n; suppressing the spin indices $|n\rangle = a^{\dagger(1)}_n|\text{vac}\rangle$. This operator is local if these eigenstates are localized. Trivially, Eq. (6.7) is satisfied.

Next we construct

$$a^{\dagger(2)}_{n\sigma} = a^{\dagger(1)}_{n\sigma} + \sum_{\tau\tau'\tau''}^{jkl} \Gamma^{n\sigma}_{\substack{jkl \\ \tau\tau'\tau''}} a^{\dagger(1)}_{j\tau} a^{\dagger(1)}_{k\tau'} a^{(1)}_{n\tau''} \tag{6.8}$$

so that $a^{\dagger(2)}_{n\sigma} P_1 = a^{\dagger(1)}_{n\sigma} P_1$. We can always choose the Γ's such that $|n\sigma, m\tau\rangle = a^{\dagger(2)}_{n\sigma} a^{\dagger(2)}_{m\tau}|\text{vac}\rangle$ is an eigenstate of H with energy $E^{\sigma\tau}_{mn}$. Neglecting the spin indices

$$\Gamma^{n}_{jkl} = (\langle j| \otimes \langle k|)|nl\rangle - \delta_{jn}\delta_{kl} \tag{6.9}$$

There are as many ways of doing this are there are ways of assigning the indices to the 2-particle states. We choose the indices to maximize the overlap $(\langle n| \otimes \langle m|)|nl\rangle$. If the two-particle states and one-particle states are localized, then $a^{\dagger(2)}_{n\sigma}$ will be localized. Eq. (6.7) is clearly satisfied. Constructing the higher order operators follows the same procedure.

To connect with the existing literature [150, 80, 35, 142], we note that this construction yields a Hamiltonian of the form

$$H = \sum_{n\sigma} \epsilon_n \tilde{n}_{n\sigma} + \sum_{\substack{nm \\ \sigma\sigma'}} U^{(2)}_{\substack{nm \\ \sigma\sigma'}} \tilde{n}_{n\sigma} \tilde{n}_{m\sigma'} + \ldots \tag{6.10}$$

where $\tilde{n}_{n\sigma} = \lim_{j\to\infty} a^{\dagger(j)}_{n\sigma} a^{(j)}_{n\sigma}$. The coefficients are local, meaning $U^{(k)}_{i_1 i_2 \ldots i_k} \sim \exp(-\max|\mathrm{i}_\alpha - \mathrm{i}_\beta|/\xi_\mathrm{k})$. They can be expressed in terms of the eigenvalues of the k-body problem; for example $U^{(2)}_{\substack{nm \\ \sigma\sigma'}} = E^{\sigma\sigma'}_{mn} - \epsilon_n - \epsilon_m$. Appendix A.4 shows a graph of this quantity for typical parameters, illustrating the exponential decay.

CHAPTER 7

OBSERVATION OF A NEW SUPERFLUID PHASE FOR 3HE EMBEDDED IN NEMATICALLY ORDERED AEROGEL

The work discussed in this chapter was done in collaboration with an experimental group at Cornell led by Jeevak Parpia. This work was originally published as *Observation of a new superfluid phase for 3He embedded in nematically ordered aerogel* by N. Zhelev, M. D. Reichl, T. S. Abhilash, E. N. Smith, K. X. Nguyen, E. J. Mueller and J. M. Parpia, Nature Communications 7: 12975 (2016).

Superfluid ^{3}He is our best example of a quantum system where the fermionic constituents form Cooper pairs with finite angular momentum. Similar to unconventional superconductors, such as Sr_2RuO_4 and UPt_3 [109, 42] the properties of this exotic superfluid can be engineered with disorder [133, 145]. Theory predicts that nanoscale confinement and anisotropic disorder profoundly change the stability of the pairing, and can lead to novel phases [12, 162, 175, 169]

Two superfluid phases – A and B phase – are observed in bulk 3He when it is cooled to ultralow temperatures (below 0.902 to 2.444 mK depending on the pressure) [168]. At these temperatures bulk ^{3}He is an extremely pure system free of any disorder: anything besides helium is solid and condenses on the surfaces, and ^{4}He phase separates with practically zero solubility in the ^{3}He. To deliberately introduce disorder one can embed the fluid in highly porous aerogels [134, 156]. For ^{3}He in aerogel, T_c is suppressed and the relative stability of the A and B phases is markedly different compared to the bulk. The phase diagram is further distorted when weak anisotropy is introduced by compress-

ing or stretching the aerogel [133, 24, 60, 49]. In the experiment described here the fluid is imbeded within a highly oriented nematic aerogel [14, 50, 15] which provides extreme anisotropy. Nuclear magnetic resonance (NMR) experiments [14, 50, 15] identify the resulting phases as polar-distorted A and B phases. Evidence for a novel polar phase was recently observed in a NMR measurement of a different high-density nematic aerogel [51]. In the experiments described in this chapter, the aerogel is mounted on a torsion pendulum and the strands that comprise the aerogel are aligned parallel to the pendulum axis. This technique is very different from NMR and is specifically sensitive to the in-plane superfluid fraction. Spin diffusion measurements in an aerogel sample similar to the one we study reveal that the mean-free path for a particle traveling along the strands is nearly twice that of one moving perpendicular [13]. The period of the pendulum in the experiment described here measures the fraction of the fluid that is decoupled from the container, which is related to the superfluid fraction. We observe kinks when superfluid fraction is plotted versus temperature, corresponding to phase transitions. We find a new superfluid phase just below the normal to superfluid transition that is not seen in bulk ^{3}He. Drawing on theoretical work [145, 12, 63, 81] we argue that at low pressure this new superfluid phase is the polar phase.

7.1 Results

7.1.1 Microstructure of the Nematic Aerogel

Scanning electron microscope images of the aerogel sample showing its highly oriented microstructure are shown in Fig. 7.1. We estimate that the aerogel con-

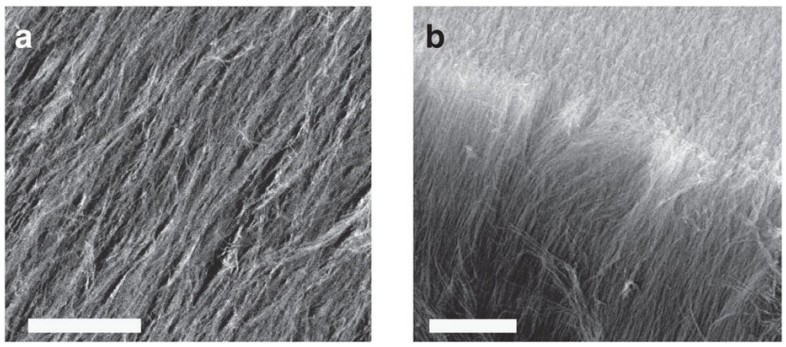

Figure 7.1: (a) SEM image in a plane parallel to the aerogel strands. Scale bar 1 μm. (b) SEM image of the edge of the aerogel sample at the intersection of planes parallel and perpendicular to the strands. Scale bar 5 μm. Images are taken at Cornell, using Tescan Mira3 Field Emission SEM.

sists of ~10 nm thick strands, spaced ~100 nm apart.

7.1.2 Ginzburg-Landau Model

The order parameter for ^{3}He is a rank-2 tensor describing the spin and orbital angular momentum of the pairs. In the bulk A-phase, the orbital angular momentum points in a fixed direction, and there exist gapless excitations whose momenta are parallel to this direction. In the B-phase, the superfluid gap is isotropic and nonzero in all directions around the Fermi surface. The polar phase, which is not stable in bulk ^{3}He, has a nodal plane: for any momentum direction in this plane, one can find gapless quasiparticles. Larger superfluid densities are associated with having fewer low-energy excitations, allowing us to distinguish these phases. Figure 7.2a shows the bulk phase diagram, and Fig. 7.2b gives a visual representation of the superfluid energy gaps in the various phases.

Following convention, we represent the order parameter as a 3×3 matrix

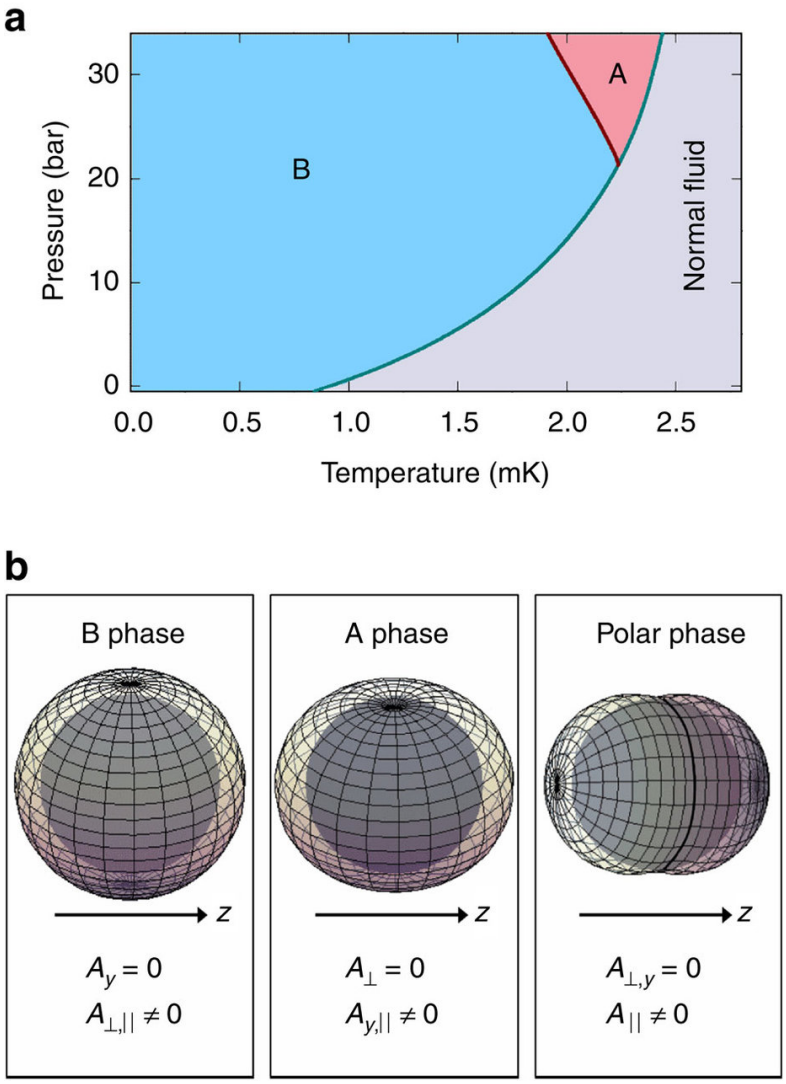

Figure 7.2: (a) Superfluid phase diagram for bulk ^{3}He at zero magnetic field. The anisotropic superfluid A phase is realized only in a relatively small region at high pressures and at temperatures near the superfluid transition temperature. (b) Visual representation of the superfluid gap around the Fermi surface for various superfluid phases of ^{3}He. The direction of largest superfluid gap is aligned with the aerogel strands along the z axis.

A with components related to the coupling of the x, y and z components of the spin and orbital angular momentum. All three phases that we see are captured by the ansatz

$$\mathbf{A} = \begin{pmatrix} A_\perp & 0 & 0 \\ 0 & A_\perp & 0 \\ 0 & iA_y & A_\parallel \end{pmatrix} \tag{7.1}$$

The conventional bulk A-phase corresponds to $A_y = A_\parallel$ and $A_\perp = 0$. Similarly, the isotropic B-phase has $A_\perp = A_\parallel$ and $A_y = 0$. The polar phase has $A_\perp = A_y = 0$. Guided by the form of the Ginsburg-Landau (GL) free energy in Refs. [145, 63] we write the free energy for this system including the fourth-order terms scaled by the appropriate coefficients β_i as follows:

$$\begin{aligned} F = &-\left(\frac{T_c - T}{T_c^{\text{bulk}}}\right)\hat{\Delta}^2|A_\parallel|^2 - \left(\frac{T_c - T}{T_c^{\text{bulk}}} + \delta\right)\hat{\Delta}^2(2|A_\perp|^2 + |A_y|^2) + \beta_1|\operatorname{Tr}(\mathbf{A}\mathbf{A}^T)|^2 \\ &\beta_2[\operatorname{Tr}(\mathbf{A}\mathbf{A}^\dagger)]^2 + \beta_3 \operatorname{Tr}[\mathbf{A}\mathbf{A}^T(\mathbf{A}\mathbf{A}^T)^*] + \beta_4 \operatorname{Tr}(\mathbf{A}\mathbf{A}^\dagger)^2 + \beta_5 \operatorname{Tr}[\mathbf{A}\mathbf{A}^\dagger(\mathbf{A}\mathbf{A}^\dagger)^*] \end{aligned} \tag{7.2}$$

Here $\hat{\Delta}$ is the value of the condensation energy, and T_c and T_c^{bulk} the superfluid transition temperatures for the fluid within the aerogel and the bulk fluid, respectively. The anisotropy in the system is parameterized by δ. The nonzero value of δ leads to two distinct transition temperatures, $T_{c\perp}$ and $T_{c\parallel} = T_c$, below which the components of the order parameter perpendicular and parallel to the aerogel anisotropy axis develop. The effect of the anisotropy of the system splitting the superfluid transition has been observed for Sr_2RuO_4 under uniaxial strain [76]. More precisely δ can be defined as:

$$\delta = \frac{T_{c\parallel} - T_{c\perp}}{T_c^{\text{bulk}}}\left(1 + \frac{\beta_1 - \beta_2 + \beta_3 - \beta_4 - \beta_5}{\beta_1 + \beta_2 + \beta_3 + \beta_4 + \beta_5}\right) \tag{7.3}$$

In the linear pair-breaking regime, δ is given by Ref. [145]:

$$\delta \simeq -\frac{\pi^2}{4}\xi_o\left(\frac{1}{\lambda_\perp} - \frac{1}{\lambda_\parallel}\right) \tag{7.4}$$

with ξ_0 being the zero-temperature coherence length, which is a measure of the strength of the pairing and $\lambda_{\perp,\parallel}$ being the quasi-particle mean-free path perpendicular or parallel to the strands.

For $T_{c\perp} < T < T_{c\parallel}$, this GL theory predicts that the system will be in the polar phase ($A_{\perp,y} = 0, A_\parallel > 0$). For lower temperature, one finds either a distorted A-phase, where $A_\perp = 0$ and $A_\parallel > A_y > 0$ or a distorted B-phase, where $A_y = 0$ and $A_\parallel > A_\perp > 0$. The relative stability of these phases depends on the magnitude of the β terms in equation (7.2). Quasi-particle mean-free paths in the nematic aerogel are expected to be relatively long (>450 nm (Ref. [13])), compared with the mean-free paths of ordinary silica aerogel (~100 nm). Thus, we assume that the β parameters are only weakly affected by the disorder, and in our analysis, we use the bulk values given in Ref. [39].

The degree of polar distortion can be parameterized by $A_y/A_\parallel$ in the A-phase and $A_\perp/A_\parallel$ in the B-phase. Both these ratios become smaller at lower pressures (corresponding to more polar distortion), and all three phases become less distinct. The A-to-B transition is first order and is hysteretic, while A-to-polar or B-to-polar transition is second order and should be free of hysteresis. Recent theoretical work argues that this Ginzburg-Landau theory may breakdown at high pressures, with several competing possibilities for the high-temperature phase [81]. The torsion pendlum measurements discussed here suggest that this breakdown does indeed occur, but they cannot distinguish between the various possible high-temperature phases.

7.1.3 Evidence for Phase Transitions in the Superfluid Fraction Data

The torsional oscillator experiment probes the superfluid density in the direction perpendicular to the pendulum axis, and hence perpendicular to the aerogel strands. Data for the superfluid fraction versus T/T_c^{bulk} for six different pressures ranging from 32 bar, down to 0.1 bar are shown in Fig. 7.3a. At high pressures (32, 29.1 and 15.4 bar), a clear hysteresis loop is seen between warming and cooling, indicating a first-order phase transition. Guided by the results from NMR experiments done on a similar sample[14, 50, 15] and by the GL model predictions, we identify these as polar-distorted B and polar-distorted A. As pressure is lowered, the hysteresis loop gets less pronounced, indicating a larger degree of polar distortion. Experimental uncertainty in the data is characterized by the relative spread of the data points. In addition, a small systematic error could arise due to the possible thermal lag between our thermometer and the experimental cell. Differences between cooling and warming at 3.6 and 0.1 bar are attributed to this systematic error.

At temperatures slightly above the hysteresis loop, on both cooling and warming, we observe a change in slope in the superfluid fraction versus T. The change in slope is especially pronounced at low pressures. We label the temperature of this feature as T_{kink}. At 7.5 bar (Fig. 7.3b), data for cooling and warming overlap at low temperatures and near T_c. A difference between the cooling and warming traces larger than the experimental uncertainty is observed at intermediate temperatures. This difference is too large to be due to thermal lag. Instead, we associate the difference with an A-to-B transition. In addition, we observe a very sharp and pronounced kink in the superfluid fraction data. Thus, we con-

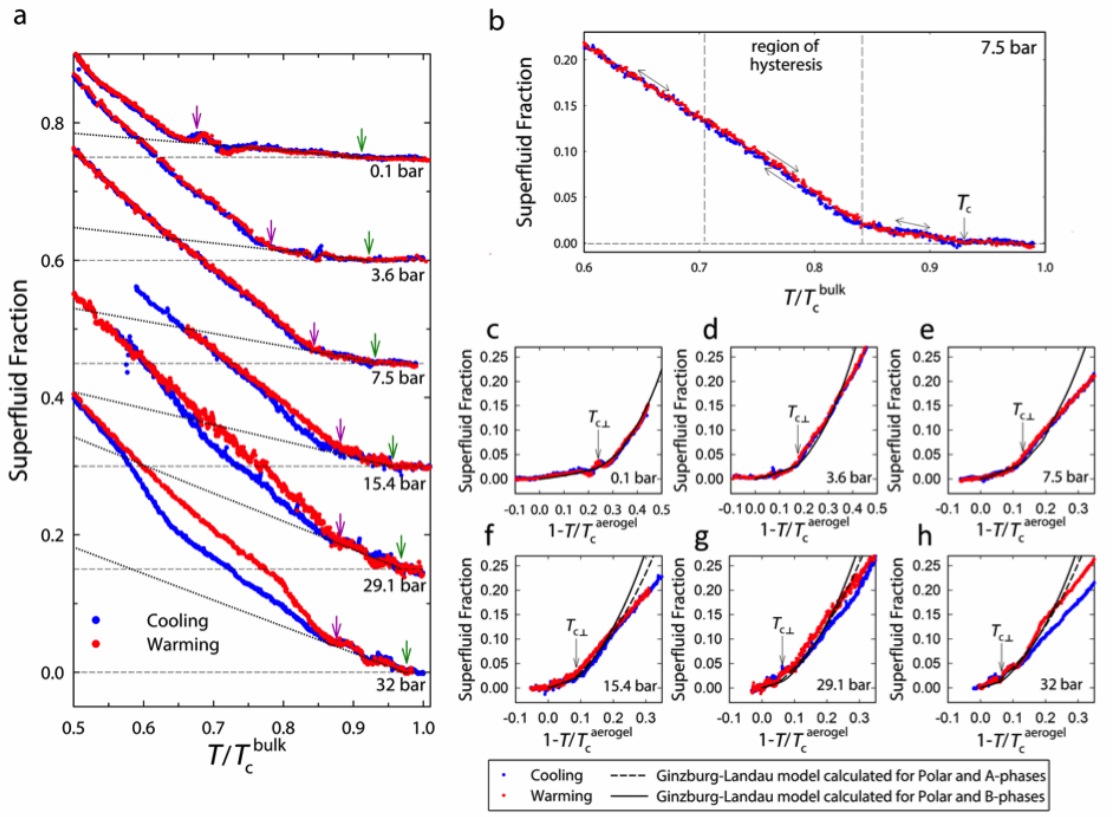

Figure 7.3: (a) Experimental data for the measured superfluid fraction versus T/T_c^{bulk} for both cooling and warming at each of the experimental pressures. Data for each adjacent pressure are offset by 0.15 in the y direction for clarity. Dashed lines indicate the zero superfluid fraction level for each pressure. Green arrows mark the superfluid transition temperature for the ^{3}He in the aerogel (T_c). Magenta arrows indicate the point at which change in the superfluid fraction data is observed (T_{kink}). Dotted lines match the data between T_c and T_{kink} and serve as guides to the eye, aiding to identify the precise location of T_{kink}. (b) Data for 7.5 bar. A region of slight hysteresis between cooling and warming is bounded by two vertical dashed lines. (c-h) Superfluid fraction data (cooling and warming) plotted alongside the superfluid fraction calculated using a GinzburgLandau (GL) model for the ^{3}He in the nematically ordered aerogel. At high pressures, both A and B phases are present, whereas at low pressures, only B-phase is observed. Data are plotted versus $1 - T/T_c$, where T_c is the temperature of the superfluid transition in aerogel. The temperature, $T_{c\perp}$, at which the components of the order parameter perpendicular to the strands become nonzero is indicated for each pressure with an arrow.

clude that there are three superfluid phases present. Near T_c a high-temperature phase is stable, which transitions on cooling to a distorted A phase. Cooling through the region of hysteresis the distorted A-phase transitions to a distorted B-phase. On warming, the distorted B-phase persists through the region of hysteresis until it transitions to the high-temperature phase just below T_c. We identify $T_{\rm kink}$ as the temperature of the phase transition between a high-temperature superfluid phase and A or B phase. No hysteresis is associated with the transition at $T_{\rm kink}$, therefore the transition is second order. The superfluid phase right below T_c is identified by NMR as an equal spin pairing phase [14, 50, 15] (both the A-phase and polar phase are characterized by equal spin pairing).

7.2 Discussion

To test whether $T_{\rm kink}$ is related to $T_{c\perp}$, we look for the value of the anisotropy parameter δ in equation (7.2) such that we obtain the best match between the predicted values for $T_{c\perp}$ and the observed $T_{\rm kink}$. The resulting value for δ is of a similar magnitude compared with the one predicted in equation (7.4), as we insert the values for $\lambda_{\perp,\parallel}$ measured by spin diffusion (450 and 850 nm) [13]. $T_{\rm kink}$ conforms to our prediction for $T_{c\perp}$ reasonably well at low pressures (0.1, 3.6, 7.5 and 15.4 bar). At high pressures (29.1 and 32 bar), the agreement is not as good and the kink is seen at lower temperatures than the predicted location of $T_{c\perp}$. Minimizing the Ginzburg-Landau free energy in equation (7.2), we obtain the values for the equilibrium order parameter A and calculate the expected superfluid fraction (see Appendix B). The calculated values, guided by our model, assume a transition from a pure polar to a polar-distorted A or B phase (and not merely a crossover) and a degree of superfluid order parameter suppres-

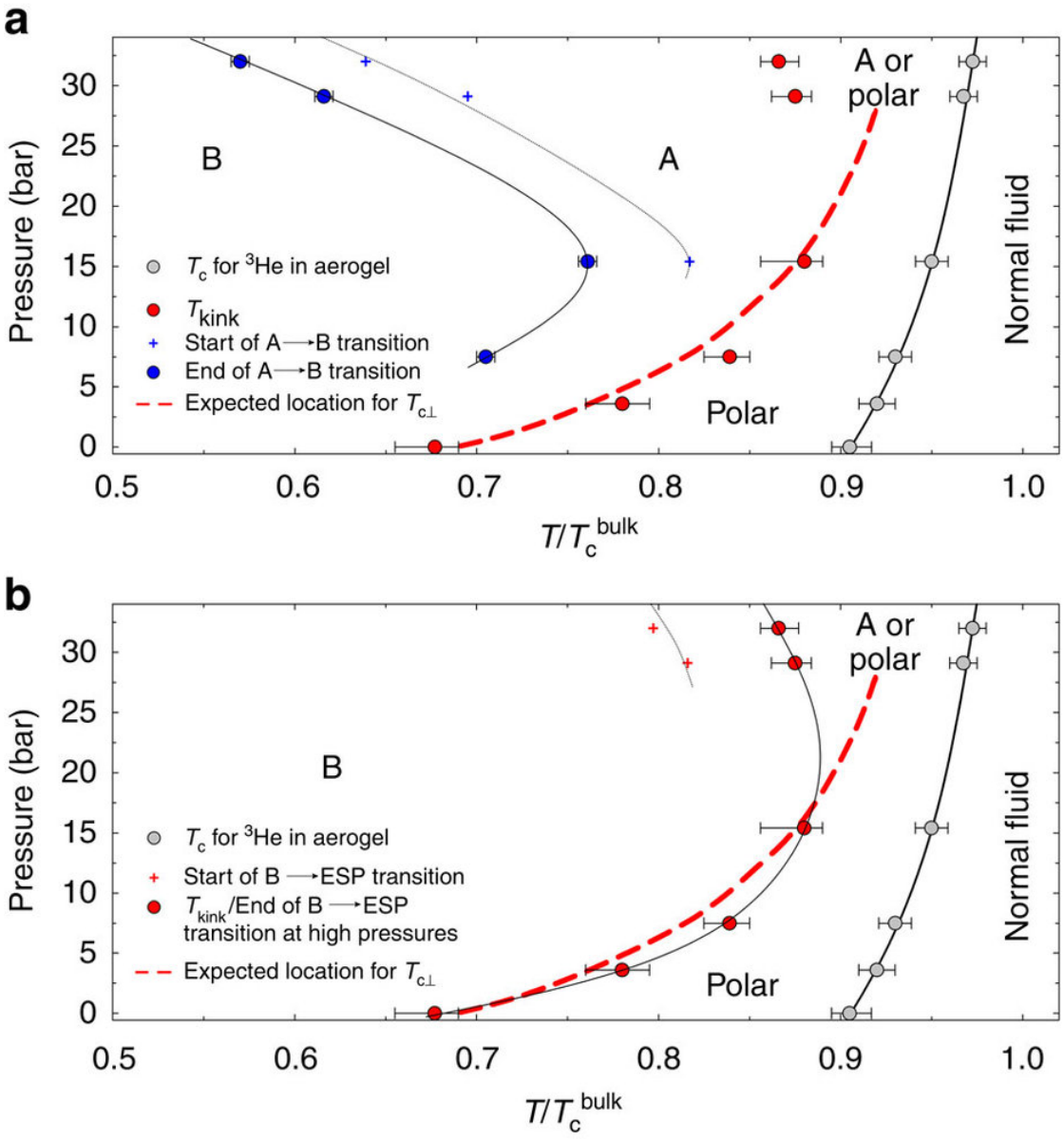

Figure 7.4: (a) Experimental phase diagram on cooling. (b) Experimental phase diagram on warming. Shown are the locations for the experimentally observed phase transitions. Black lines (solid and dotted) connecting the experimental data points are guides to the eye. Due to the experimental noise in the data, there is some uncertainty in locating the precise temperatures at which the superfluid fraction data deviated from the bulk contribution (T_c for the ^{3}He in aerogel), the data changes slope ($T_{\rm kink}$) and the locations at which the cooling and warming traces join (end of A-to-B and end of B-to-ESP transitions). These uncertainties are indicated with appropriate error bars.

sion due to the proximity of the aerogel strands (see Appendix B). We see very good agreement, especially at low pressures, between the data and calculated values (Fig. 7.3c). This leads us to conclude that at low pressures, the high-temperature phase has characteristics that correspond to the polar phase, while at high pressures it has additional structure. The system thus displays characteristics of two distinct transitions associated (by G-L theory) with the highly anisotropic mean free paths. The first transition is from the normal to the pure Polar phase and the second to the low temperature A or B phase. These latter phases evolve continuously with diminishing polar distortion as the temperature is lowered. This interpretation is also consistent with NMR measurements, which were done with an aerogel sample that was grown by the same process as ours. They found a larger frequency shift at low pressures than at high pressures [14, 50, 15]. Such an evolution of the frequency shift is consistent with a polar-like phase evolving into another structure, but even at the lowest pressures, the frequency shift observed in the NMR measurements was somewhat smaller than what one expects for a pure polar phase. Furthermore, by exposing the superfluid to a rapid series of large NMR pulses, the Moscow group managed to create a spin glass state between the A and B transition and T_c. A spin glass state cannot be created in the polar phase. We note, however, beyond the possibility of aerogel sample differences, the differences of the interpretation between the NMR measurements and this experiment can be explained the following way. If there is a coexistence of a polar and A-phase localized in different parts of the sample, NMR would measure a spatial average that would appear as a highly polar-distorted A-phase. In contrast, torsion pendulum experiments probe the component of the superfluid fraction tensor in the flow direction perpendicular to the aerogel strands. The superfluid density samples the gap along the equa-

torial nodal line of the Fermi surface leading to the strong superfluid fraction suppression. Even if not all the fluid in the torsion pendulum head is in the polar phase, as long as there is no path connecting the regions of non-polar phase throughout the pendulum head, the superfluid fraction suppression would still be similar to that of the case of having only polar phase in the sample. Torsion pendulum measurements are thus inherently more sensitive to the presence of the polar phase compared with NMR. In addition, the Moscow group recently observed clear evidence for a fully polar phase of superfluid ^{3}He embedded in a different type of nematic aerogel using NMR [51]. Both results confirm the prediction that the strong anisotropy of the nematically ordered aerogel matrix promotes the emergence of the polar phase [12].

We summarize the observed phase transitions and our inferences for the natures of the superfluid phases occupying each region of the phase diagram in Fig. 7.4.

In this chapter, we have described a series of experiments that reveal striking new phenomena in the superfluid phases of ^{3}He embedded in a highly oriented aerogel. Both A and B phases are polar-distorted compared with their bulk counterparts, and their region of stability is markedly different compared with the bulk. We see a high-temperature phase that has no analogue in the bulk. We argue that at low pressures, this superfluid is the polar phase.

APPENDIX A

COMMENTS ON THE AUBREY-ANDRE MODEL AND A DERIVATION OF THE CLUSTER EXPANSION

A.1 Imbalance vs. Superlattice Period in the Non-interacting Limit

In the non-interacting limit, the experiment is well modeled by the Aubrey-Andre model

$$H = -J \sum_{i,\sigma} \left(c^{\dagger}_{i,\sigma} c_{i+1,\sigma} + \text{h.c} \right) + \Delta \sum_{i,\sigma} \cos(2\pi\beta i + \phi) c^{\dagger}_{i,\sigma} c_{i,\sigma} \tag{A.1}$$

where J is the nearest neighbor hopping strength, Δ is the strength of the periodic superlattice, and β^{-1} is the period of the superlattice. As discussed in the main text, this is an interesting model as its behavior depends on if β is rational or irrational (or in a finite system of length N_s, if $N_s\beta$ is an integer or not).

Starting with a particle on an odd site, we numerical evolve the single-particle wave-function and calculate the average long-time imbalance $I_\infty = n_{\text{odd}} - n_{\text{even}}$, where $n_{\text{odd/even}}$ is the average long-time density on odd and even sites, respectively.

Fig. A.1 shows I_∞ as a function of β where $N_s = 200$, $\Delta/J = 3$ and $\phi = 0$. The behavior of the imbalance depends strongly on whether β is irrational or rational, and thus displays a fractal structure. When $N_s\beta = N_s p/q$ is an integer, I_∞ has peaks for even q and troughs for odd q. Increasing N_s leads to finer structure.

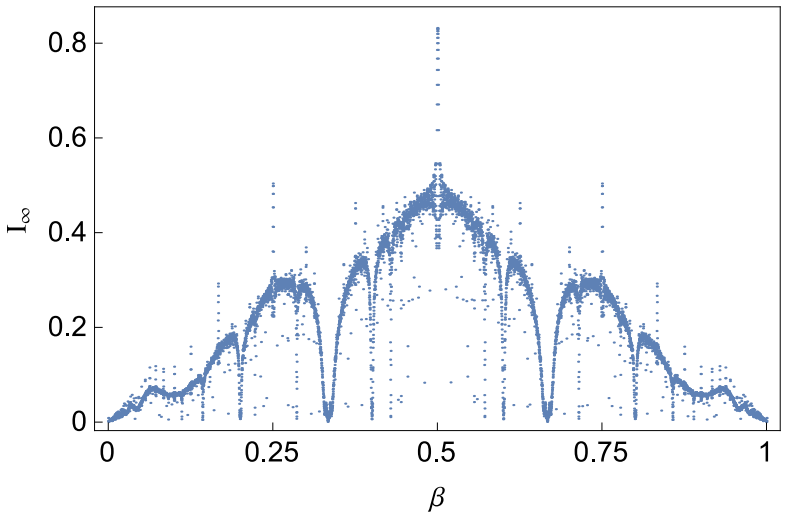

Figure A.1: Long time density imbalance I_∞ as a function of the period β^{-1} of the superlattice (in units of the lattice constant for the primary lattice) for a noninteracting one dimensional system with $N_s = 200$ sites and superlattice strength $\Delta/J = 3$.

A.2 Derivation of Cluster Expansion

Here we will derive Eq. (6.6) given in the main text. From Eq. (6.4) we have

$$\begin{aligned}\langle I(t)\rangle =&\frac{1}{Z}\Big[\epsilon(1-\epsilon)^{N_s-1}\sum_{\{1\}}{}'C_{\{1\}}(t)+\frac{\epsilon^2}{2}(1-\epsilon)^{N_s-2}\sum_{\{2\}}{}'C_{\{2\}}(t)\\&+\frac{\epsilon^3}{3}(1-\epsilon)^{N_s-3}\sum_{\{3\}}{}'C_{\{3\}}(t)+...+\frac{\epsilon^{N_s}}{N_s}\sum_{\{N_s\}}{}'C_{\{N_s\}}(t)\Big].\end{aligned} \tag{A.2}$$

where $\{n\} = \{i_1\sigma_1, i_2\sigma_2, ..., i_n\sigma_n\}$ labels an n-particle initial state with particles at sites i with spin σ, $\sum'_{\{n\}}$ denotes a sum over the i_j's and σ_j's such that the i_j's are restricted to odd sites.

Substituting Eq. (6.5) in Eq. (6.4) we have

$$\begin{aligned}Z\langle I(t)\rangle =&\epsilon(1-\epsilon)^{N_s-1}\sum_{\{1\}}{}'\widetilde{C}_{\{1\}}(t)+\frac{\epsilon^2}{2}(1-\epsilon)^{N_s-2}\sum_{\{2\}}{}'\Big[\widetilde{C}_{\{2\}}(t)+\sum_{\langle\{1\}\in\{2\}\rangle}\widetilde{C}_{\{1\}}(t)\Big]\\&+\frac{\epsilon^3}{3}(1-\epsilon)^{N_s-3}\sum_{\{3\}}{}'\Big[\widetilde{C}_{\{3\}}(t)+\sum_{\langle\{2\}\in\{3\}\rangle}\widetilde{C}_{\{2\}}(t)+\sum_{\langle\{1\}\in\{3\}\rangle}\widetilde{C}_{\{1\}}(t)\Big]+...\end{aligned} \tag{A.3}$$

where $\sum_{\langle\{k\}\in\{n\}\rangle}$ denotes a sum over all $\binom{n}{k}$ combinations of k site and spin labels in $\{n\}$. For example, neglecting spin indices: $\sum_{\{2\}}{}' \sum_{\langle\{1\}\in\{2\}\rangle} f(\{1\}) = \sum_{\substack{i_1\text{odd}\\ i_2\text{odd}}}(f(i_1) + f(i_2))$.

We note the following identity:

$$\sum_{\{n\}}{}' \sum_{\langle\{k\}\in\{n\}\rangle} \widetilde{C}_{\{k\}}(t) = \binom{N_s-k}{n-k} \sum_{\{k\}}{}' \widetilde{C}_{\{k\}}(t) \tag{A.4}$$

where the combinatorial factor is the number of ways of choosing the $n-k$ elements of $\{n\}$ which are not in $\{k\}$ out of the N_s-k available starting positions/spins.

Substituting this identity into Eq. (A.3) yields

$$\begin{aligned} Z\langle I(t)\rangle =& \epsilon(1-\epsilon)^{N_s-1} \sum_{\{1\}}{}' \widetilde{C}_{\{1\}}(t) + \frac{\epsilon^2}{2}(1-\epsilon)^{N_s-2}\Big[\sum_{\{2\}}{}' \widetilde{C}_{\{2\}}(t) + \binom{N_s-1}{1}\sum_{\{1\}}{}' \widetilde{C}_{\{1\}}(t)\Big] \\ &+ \frac{\epsilon^3}{3}(1-\epsilon)^{N_s-3}\Big[\sum_{\{3\}}{}' \widetilde{C}_{\{3\}}(t) + \binom{N_s-2}{1}\sum_{\{2\}}{}' \widetilde{C}_{\{2\}}(t) + \binom{N_s-1}{2}\sum_{\{1\}}{}' \widetilde{C}_{\{1\}}(t)\Big] + \ldots \end{aligned} \tag{A.5}$$

Collecting like terms, we have

$$\begin{aligned} Z\langle I(t)\rangle =& \sum_{n=1}^{N_s} \frac{1}{n}\epsilon^n(1-\epsilon)^{N_s-n}\binom{N_s-1}{n-1}\sum_{\{1\}}{}' \widetilde{C}_{\{1\}}(t) \\ &+ \sum_{n=2}^{N_s} \frac{1}{n}\epsilon^n(1-\epsilon)^{N_s-n}\binom{N_s-2}{n-2}\sum_{\{2\}}{}' \widetilde{C}_{\{2\}}(t) \\ &+ \sum_{n=3}^{N_s} \frac{1}{n}\epsilon^n(1-\epsilon)^{N_s-n}\binom{N_s-3}{n-3}\sum_{\{3\}}{}' \widetilde{C}_{\{3\}}(t) \\ &+ \ldots \end{aligned} \tag{A.6}$$

which can be expressed as

$$\langle I(t)\rangle = A_1(\epsilon)\sum_{\{1\}}{}'\widetilde{C}_{\{1\}}(t) + A_2(\epsilon)\sum_{\{2\}}{}'\widetilde{C}_{\{2\}}(t) + A_3(\epsilon)\sum_{\{3\}}{}'\widetilde{C}_{\{3\}}(t) + ... + \sum_{\{N_s\}}{}'A_{N_s}(\epsilon)\widetilde{C}_{\{N_s\}}(t) \tag{A.7}$$

where $A_k(\epsilon) = \frac{1}{Z}\sum_{n=k}^{N_s}\frac{1}{n}\epsilon^n(1-\epsilon)^{N_s-n}\binom{N_s-k}{n-k}$. Taking the $N_s \to \infty$ limit gives Eq. (6.6) to $O(\epsilon^2)$. Including finite size corrections, we have $A_1(\epsilon) = \frac{1}{N_s}$ and $A_2(\epsilon) = \frac{\epsilon N_s - 1 + (1-\epsilon)^{N_s}}{N_s(N_s-1)(1-(1-\epsilon)^{N_s})}$.

A.3 Doublon Weighting

Here we develop a cluster expansion for an ensemble averaged imbalance $\langle I(t)\rangle'$ which weights initial states with separate probabilities for doublons and singlons. We define $\langle I(t)\rangle'$ by

$$\langle I(t)\rangle' = \frac{1}{\langle N\rangle Z}\sum_{\substack{n_\uparrow,n_\downarrow,n_d \\ n_\uparrow+n_\downarrow+n_d\le N_s/2}}\sum{}'_{\{n_\uparrow\}\{n_\downarrow\}\{n_d\}}\rho^{n_\uparrow+n_\downarrow}\tau^{n_d}\langle\{n_\uparrow\}\{n_\downarrow\}\{n_d\}|\hat{n}_I(t)|\{n_\uparrow\}\{n_\downarrow\}\{n_d\}\rangle \tag{A.8}$$

where $\{n_\uparrow\} = \{i_1, i_2, ..., i_{n_\uparrow}\}$, $\{n_\downarrow\} = \{j_1, j_2, ..., j_{n_\downarrow}\}$, and $\{n_d\} = \{k_1, k_2, ..., k_{n_d}\}$ label the sites of up spin singlons, down spin singlons, and doublons, respectively. The symbol $\sum'_{\{n_\uparrow\}\{n_\downarrow\}\{n_d\}}$ denotes a sum over all possible locations of $n_\uparrow$ up-spin singlons, $n_\downarrow$ down-spin singlons, and n_d doublons, restricted to odd sites. ρ and τ are weights for the singlons and doublons. Z is a normalization factor given by

$$Z = \sum_{\substack{n_\uparrow,n_\downarrow,n_d \\ n_\uparrow+n_\downarrow+n_d\le N_s/2}}\rho^{n_\uparrow+n_\downarrow}\tau^{n_d}\binom{N_s/2}{n_\uparrow n_\downarrow n_d} = (1+2\rho+\tau)^{N_s/2} \tag{A.9}$$

where $\binom{N_s/2}{n_\uparrow n_\downarrow n_d} = \frac{N_s/2!}{n_\uparrow! n_\downarrow! n_d!(N_s/2-n_\uparrow n_\downarrow n_d)!}$ is the number of ways of assigning $n_\uparrow + n_\downarrow$ singlons and n_d doublons to $N_s/2$ odd sites. $\langle N\rangle$ is the mean number of particles

and is given by

$$\langle N\rangle = \frac{1}{Z}\sum_{\substack{n_\uparrow,n_\downarrow,n_d \\ n_\uparrow+n_\downarrow+n_d\leq N_s/2}} \rho^{n_\uparrow+n_\downarrow}\tau^{n_d}\binom{N_s/2}{n_\uparrow n_\downarrow n_d}(n_\uparrow+n_\downarrow+2n_d) = \frac{N_s(\rho+\tau)}{1+2\rho+\tau} \tag{A.10}$$

We define $C_{\{n_\uparrow\}\{n_\downarrow\}\{n_d\}}(t) = \langle\{n_\uparrow\}\{n_\downarrow\}\{n_d\}|\hat{n}_I(t)|\{n_\uparrow\}\{n_\downarrow\}\{n_d\}\rangle$. We decompose the expectation value $C(t)$ into single particle contributions, two particle contributions, etc. in a manner similar to Eq. (6.5) in the main text:

$$\begin{aligned} C_{\{n_\uparrow\}\{n_\downarrow\}\{n_d\}}(t) = &\sum_{\langle\{1\}\in\{n_\uparrow\}\rangle} C_{\{1\}\{0\}\{0\}}(t) + \sum_{\langle\{1\}\in\{n_\downarrow\}\rangle} C_{\{0\}\{1\}\{0\}}(t) \\ &+ \sum_{\langle\{1\}\in\{n_d\}\rangle} C_{\{0\}\{0\}\{1\}}(t) + \sum_{\langle\{1\}\in\{n_\uparrow\},\{1\}\in\{n_\downarrow\}\rangle} \widetilde{C}_{\{1\}\{1\}\{0\}}(t) + ... \end{aligned} \tag{A.11}$$

$\sum_{\langle\{1\}\in\{k\}\rangle}$ denotes a sum over all labels in $\{k\}$ and $\widetilde{C}_{\{1\}\{1\}\{0\}}(t) = C_{\{1\}\{1\}\{0\}}(t) - C_{\{1\}\{0\}\{0\}}(t) - C_{\{0\}\{1\}\{0\}}(t)$. There are higher particle number terms in this decomposition, but for the low density limit we consider here, it is sufficient (and notationally simpler) to keep terms up to two-body. We note that two-body terms like $\widetilde{C}_{\{2\}\{0\}\{0\}}(t) = C_{\{2\}\{0\}\{0\}}(t) - C_{\{1\}\{0\}\{0\}}(t) - C_{\{1\}\{0\}\{0\}}(t)$ vanish, since two atoms with the same spin do not interact.

Substituting Eq. (A.11) into Eq. (A.8) and performing simple summations yields

$$\begin{aligned} \langle I(t)\rangle' = &\frac{\rho}{\rho+\tau}\frac{1}{N_s}\left(\sum_{\{1\}}{}' C_{\{1\}\{0\}\{0\}}(t) + \sum_{\{1\}}{}' C_{\{0\}\{1\}\{0\}}(t)\right) \\ &+ \frac{\tau}{\rho+\tau}\frac{1}{N_s}\sum_{\{1\}}{}' C_{\{0\}\{0\}\{1\}}(t) + \frac{\rho+\tau}{(1+2\rho+\tau)}\frac{1}{N_s}\sum{}'_{\{1\},\{1\}} \widetilde{C}_{\{1\}\{1\}\{0\}}(t) \end{aligned} \tag{A.12}$$

We vary ρ and τ in Eq. (A.12) to produce Fig. 6.3 in the main text.

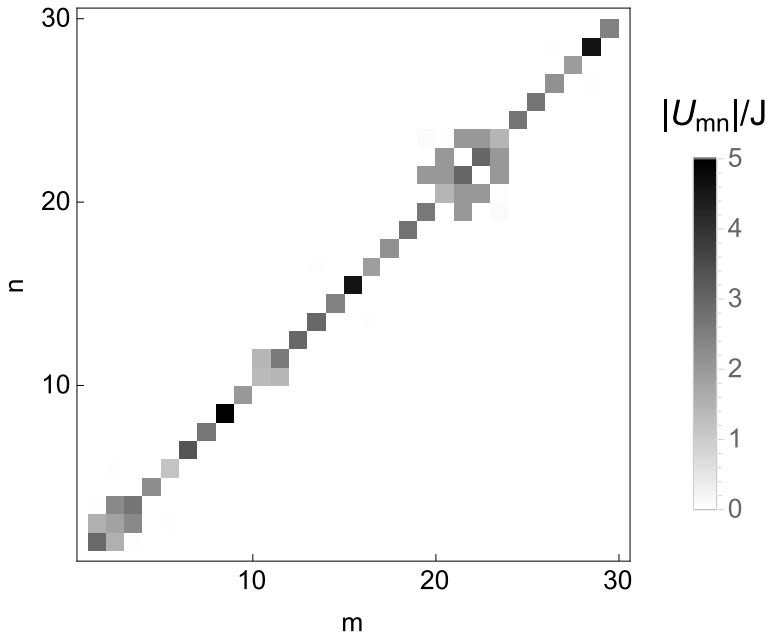

Figure A.2: Two particle interaction term $U^{(2)}_{mn}$ appearing in Eq. (5.10) of the main text. Here $\Delta/J = 3$, $U/J = 3$, and $\beta = 0.721$. Darker colors correspond to larger values of $|U^{(2)}_{mn}|$. For large $|n - m|$, $U^{(2)}_{nm}$ is exponentially small. For $n = m$, $U^{(2)}_{mn} \sim U$.

A.4 Local Integrals of Motion

Fig. A.2 shows the coefficients $U^{(2)}_{\substack{mn \\ \uparrow\downarrow}}$ which appear in Eq. (6.10) of the main text.

APPENDIX B

CALCULATING THE SUPERFLUID FRACTION FROM THE GL-MODEL

Having determined the values of the matrix order parameter that minimizes the GL free energy, we calculate the superfluid fraction in the plane of the torsion pendulum head starting from Ref. [168]:

$$\rho^0_{nij} = 3\rho\langle\hat{\mathbf{k}}_i\hat{\mathbf{k}}_j Y_o(\hat{k}, T)\rangle_{\hat{k}} \tag{B.1}$$

$$\rho_n = \frac{m^*}{m}\left(\mathbf{1} + \frac{1}{3}F_1^s\frac{\rho_n^0}{\rho}\right)^{-1}\rho_n^0 \tag{B.2}$$

$$\rho_{s,\text{in-plane}} = \rho - \frac{\rho_{n,xx} + \rho_{n,yy}}{2} \tag{B.3}$$

where ρ_n and ρ_n^0 are 3×3 matrices with components $\rho_{n,ij}$ and $\rho^0_{n,ij}$ respectively, m^* is the ^{3}He quasiparticles renormalized mass, and F_1^s is the Landau parameter. $Y_0(\hat{\mathbf{k}}, T)$ is the Yosida function, which is related to the energy density distribution along the Fermi sphere, f:

$$Y_0(\hat{\mathbf{k}}, T) = -\int_{-\infty}^{\infty} d\epsilon_{\hat{\mathbf{k}}}\left(\frac{\partial f}{\partial E_{\hat{\mathbf{k}}}}\right) \tag{B.4}$$

with the information for the gap structure contained in $\frac{\partial f}{\partial E_{\hat{\mathbf{k}}}}$.

The presence of impurity scattering in aerogels leads to a reduction of the superfluid gap, as well as the superfluid temperature compared to the bulk [102, 162]. Figure B.1 shows data compiled in Ref. [102] for the measured superfluid gap over the superfluid gap in the bulk fluid plotted versus the ratio of

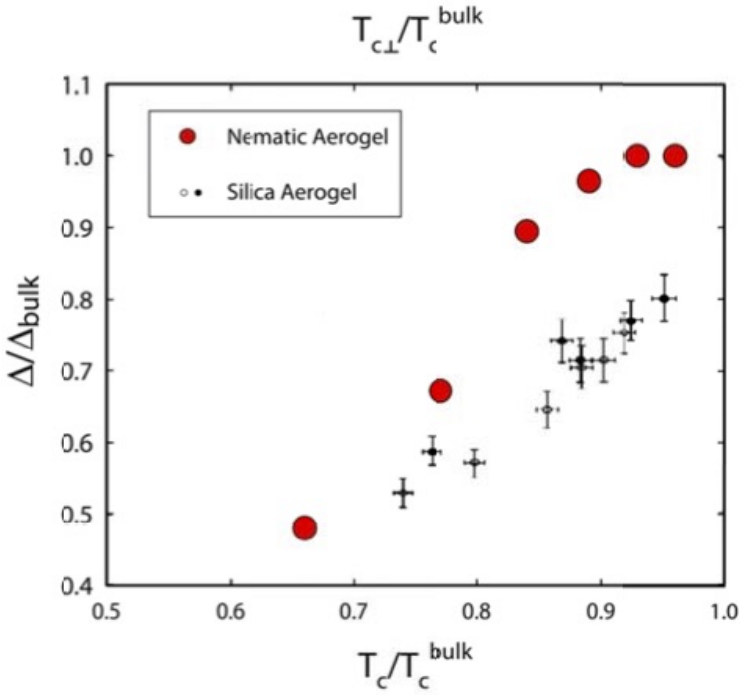

Figure B.1: The ratio of the superfluid gap for the fluid in the aerogel over the superfluid gap of the bulk fluid is plotted versus the superfluid transition temperature suppression for different aerogel samples. Black filled and empty circles represent data from Ref. [102] plotted against T_c/T_c^{bulk} for two isotropic silica aerogel samples with different porosities (99.5% and 98%). Filled red dots indicate the factors by which we scaled the superfluid gap in our GL model calculated superfluid fractions for the present experiment plotted versus T_c/T_c^{bulk}.

T_c in aerogel and in bulk for several isotropic (silica) aerogel samples. It is observed that a strong relationship between T_c suppression and gap suppression exists. In our aerogel sample (nematic aerogel), we take $T_{c\perp}/T_c^{\text{bulk}}$ to be the relevant parameter that should determine the ratio of the superfluid gap for ^{3}He in the aerogel compared to that in the bulk. We scale the superfluid fractions from Eq. (B.3) by the square of the ratio between the superfluid gap for the fluid within the aerogel and the bulk superfluid gap (superfluid density is proportional to the square of the gap). The ratio that best fits the experimental data is plotted as filled red circles in Fig. B.1 for each of the experimental pressures. These were chosen to be temperature independent, but varied with pressure.

As seen in the figure, the factors by which the gap is suppressed that best match the data vary roughly linearly with superfluid transition temperature suppression in a similar fashion as previously observed for the fluid in isotropic silica aerogels.

BIBLIOGRAPHY

[1] M. Abad, M. Guilleumas, R. Mayol, and M. Pi. Vortex rings in toroidal bose-einstein condensates. *Laser Physics*, 18(5):648–652, 2008.

[2] E. Abrahams, P. W. Anderson, D. C. Licciardello, and T. V. Ramakrishnan. Scaling theory of localization: Absence of quantum diffusion in two dimensions. *Physical Review Letters*, 42(10):673–676, 1979.

[3] A. Adams, L. D. Carr, T. Schäfer, P. Steinberg, and J. E. Thomas. Strongly correlated quantum fluids: ultracold quantum gases, quantum chromodynamic plasmas and holographic duality. *New Journal of Physics*, 14(11):115009, 2012.

[4] M. Aidelsburger, M. Atala, M. Lohse, J. T. Barreiro, B. Paredes, and I. Bloch. Realization of the hofstadter hamiltonian with ultracold atoms in optical lattices. *Physical Review Letters*, 111(18):185301, 2013.

[5] E. Altman and R. Vosk. Universal dynamics and renormalization in many-body-localized systems. *Annu. Rev. Condens. Matter Phys.*, 6(1):383–409, 2015.

[6] A. Amaricci, A. Privitera, and M. Capone. Inhomogeneous bcs-bec crossover for trapped cold atoms in optical lattices. *Physical Review A*, 89(5):053604, 2014.

[7] D. Amit and E. P. Gross. Vortex rings in a bose fluid. *Physical Review*, 145(1):130, 1966.

[8] B. P. Anderson, P. C. Haljan, C. A. Regal, D. L. Feder, L. A. Collins, C. W. Clark, and E. A. Cornell. Watching dark solitons decay into vortex rings in a bose-einstein condensate. *Physical Review Letters*, 86(14):2926, 2001.

[9] Mike H Anderson, Jason R Ensher, Michael R Matthews, Carl E Wieman, and Eric A Cornell. Observation of bose-einstein condensation in a dilute atomic vapor. *Science*, 269(5221):198, 1995.

[10] P. W. Anderson. Absence of diffusion in certain random lattices. *Physical Review*, 109(5):1492, 1958.

[11] M. Antezza, F. Dalfovo, L. P. Pitaevskii, and S. Stringari. Dark solitons in a superfluid fermi gas. *Physical Review A*, 76(4):043610, 2007.

[12] K. Aoyama and R. Ikeda. Pairing states of superfluid he 3 in uniaxially anisotropic aerogel. *Physical Review B*, 73(6):060504, 2006.

[13] R. S. Askhadullin, V. V. Dmitriev, D. A. Krasnikhin, P. N. Martynov, L. A. Melnikovsky, A. A. Osipov, A. A. Senin, and A. N. Yudin. Measurements of spin diffusion in liquid 3he in ordered aerogel. *Journal of Physics: Conference Series*, 400(1):012002, 2012.

[14] R. S. Askhadullin, V. V. Dmitriev, D. A. Krasnikhin, P. N. Martynov, A. A. Osipov, A. A. Senin, and A. N. Yudin. Phase diagram of superfluid 3he in nematically ordered aerogel. *JETP Letters*, 95(6):326–331, 2012.

[15] R. S. Askhadullin, V. V. Dmitriev, P. N. Martynov, A. A. Osipov, A. A. Senin, and A. N. Yudin. Anisotropic 2d larkin-imry-ma state in the polar distorted abm phase of 3he in a nematically ordered aerogel. *JETP Letters*, 100(10):662–668, 2015.

[16] M. Atala, M. Aidelsburger, J. T. Barreiro, D. Abanin, T. Kitagawa, E. Demler, and I. Bloch. Direct measurement of the zak phase in topological bloch bands. *Nature Physics*, 9(12):795–800, 2013.

[17] S. Aubry and G. André. Analyticity breaking and anderson localization in incommensurate lattices. *Ann. Israel Phys. Soc*, 3(133):18, 1980.

[18] A. Barelli, J. Bellissard, P. Jacquod, and D. L. Shepelyansky. Double butterfly spectrum for two interacting particles in the harper model. *Physical Review Letters*, 77(23):4752, 1996.

[19] D. M. Basko, I. L. Aleiner, and B. L. Altshuler. Metal–insulator transition in a weakly interacting many-electron system with localized single-particle states. *Annals of Physics*, 321(5):1126–1205, 2006.

[20] George Keith Batchelor. *An introduction to fluid dynamics*. Cambridge university press, 2000.

[21] S. K. Baur, M. H. Schleier-Smith, and N. R. Cooper. Dynamic optical superlattices with topological bands. *Physical Review A*, 89(5):051605, 2014.

[22] G. Baym and C. Pethick. *Landau Fermi-liquid theory: concepts and applications*. John Wiley & Sons, 2008.

[23] C. Becker, S. Stellmer, P. Soltan-Panahi, S. Dörscher, M. Baumert, E.-M.

Richter, J. Kronjäger, K. Bongs, and K. Sengstock. Oscillations and interactions of dark and dark–bright solitons in bose–einstein condensates. *Nature Physics*, 4(6):496–501, 2008.

[24] R. G. Bennett, N. Zhelev, E. N. Smith, J. Pollanen, W. P. Halperin, and J. M. Parpia. Modification of the he 3 phase diagram by anisotropic disorder. *Physical Review Letters*, 107(23):235504, 2011.

[25] J. Billy, V. Josse, Z. Zuo, A. Bernard, B. Hambrecht, P. Lugan, D. Clément, L. Sanchez-Palencia, P. Bouyer, and A. Aspect. Direct observation of anderson localization of matter waves in a controlled disorder. *Nature*, 453(7197):891–894, 2008.

[26] P. Bordia, H. P. Lüschen, S. S. Hodgman, M. Schreiber, I. Bloch, and U. Schneider. Coupling identical one-dimensional many-body localized systems. *Physical Review Letters*, 116(14):140401, 2016.

[27] J. Brand and W. P. Reinhardt. Solitonic vortices and the fundamental modes of the snake instability: Possibility of observation in the gaseous bose-einstein condensate. *Physical Review A*, 65(4):043612, 2002.

[28] V. A. Brazhnyi and V. M. Pérez-García. Stable multidimensional soliton stripes in two-component bose–einstein condensates. *Chaos, Solitons & Fractals*, 44(6):381–389, 2011.

[29] A. Bulgac, M. M. Forbes, M. M. Kelley, K. J. Roche, and G. Wlazłowski. Quantized superfluid vortex rings in the unitary fermi gas. *Physical Review Letters*, 112(2):025301, 2014.

[30] S. Burger, K. Bongs, S. Dettmer, W. Ertmer, K. Sengstock, A. Sanpera, G. V. Shlyapnikov, and M. Lewenstein. Dark solitons in bose-einstein condensates. *Physical Review Letters*, 83(25):5198, 1999.

[31] T. H. Busch and J. R. Anglin. Motion of dark solitons in trapped bose-einstein condensates. *Physical Review Letters*, 84(11):2298, 2000.

[32] Ronald Meyer Caplan. *Study of Vortex Ring Dynamics in the Nonlinear Schrdinger Equation Utilizing GPU-Accelerated High-Order Compact Numerical Integrators*. Claremont Colleges, 2012.

[33] R. Carretero-González, D. J. Frantzeskakis, and P. G. Kevrekidis. Nonlin-

ear waves in bose–einstein condensates: physical relevance and mathematical techniques. *Nonlinearity*, 21(7):R139, 2008.

[34] A. Cetoli, J. Brand, R. G. Scott, F. Dalfovo, and L. P. Pitaevskii. Snake instability of dark solitons in fermionic superfluids. *Physical Review A*, 88(4):043639, 2013.

[35] A. Chandran, I. H. Kim, G. Vidal, and D. A. Abanin. Constructing local integrals of motion in the many-body localized phase. *Physical Review B*, 91(8):085425, 2015.

[36] Q. Chen and J. Wang. Pseudogap phenomena in ultracold atomic fermi gases. *Frontiers of Physics*, 9(5):539–570, 2014.

[37] C.-C. Chien, H. Guo, Y. He, and K. Levin. Comparative study of bcs-bec crossover theories above tc: The nature of the pseudogap in ultracold atomic fermi gases. *Physical Review A*, 81(2):023622, 2010.

[38] C. Chin, R. Grimm, P. Julienne, and E. Tiesinga. Feshbach resonances in ultracold gases. *Reviews of Modern Physics*, 82(2):1225, 2010.

[39] H. Choi, J. P. Davis, J. Pollanen, T. M. Haard, and W. P. Halperin. Strong coupling corrections to the ginzburg-landau theory of superfluid he 3. *Physical Review B*, 75(17):174503, 2007.

[40] C. E. Creffield and F. Sols. Generation of uniform synthetic magnetic fields by split driving of an optical lattice. *Physical review A*, 90(2):023636, 2014.

[41] J. Dalibard, F. Gerbier, G. Juzeliūnas, and P. Öhberg. Colloquium: Artificial gauge potentials for neutral atoms. *Reviews of Modern Physics*, 83(4):1523, 2011.

[42] Y. Dalichaouch, M. C. De Andrade, D. A. Gajewski, R. Chau, P. Visani, and M. B. Maple. Impurity scattering and triplet superconductivity in u pt 3. *Physical Review Letters*, 75(21):3938, 1995.

[43] A. Dauphin and N. Goldman. Extracting the chern number from the dynamics of a fermi gas: Implementing a quantum hall bar for cold atoms. *Physical Review Letters*, 111(13):135302, 2013.

[44] Kendall B Davis, M-O Mewes, Michael R Andrews, NJ Van Druten,

DS Durfee, DM Kurn, and Wolfgang Ketterle. Bose-einstein condensation in a gas of sodium atoms. *Physical Review Letters*, 75(22):3969, 1995.

[45] P. G. De Gennes. Superconducting of metals and alloys, 1966.

[46] B. DeMarco and D. S. Jin. Onset of fermi degeneracy in a trapped atomic gas. *Science*, 285(5434):1703–1706, 1999.

[47] J. Denschlag, J. E. Simsarian, D. L. Feder, C. W. Clark, L. A. Collins, J. Cubizolles, L. Deng, E. W. Hagley, K. Helmerson, W. P. Reinhardt, et al. Generating solitons by phase engineering of a bose-einstein condensate. *Science*, 287(5450):97–101, 2000.

[48] T. Devakul and R. R. P. Singh. Early breakdown of area-law entanglement at the many-body delocalization transition. *Physical Review Letters*, 115(18):187201, 2015.

[49] V. V. Dmitriev, D. A. Krasnikhin, N. Mulders, A. A. Senin, G. E. Volovik, and A. N. Yudin. Orbital glass and spin glass states of 3he-a in aerogel. *JETP letters*, 91(11):599–606, 2010.

[50] V. V. Dmitriev, A. A. Senin, A. A. Soldatov, E. V. Surovtsev, and A. N. Yudin. B phase with polar distortion in superfluid 3he in ordered aerogel. *Journal of Experimental and Theoretical Physics*, 119(6):1088–1096, 2014.

[51] V. V. Dmitriev, A. A. Senin, A. A. Soldatov, and A. N. Yudin. Polar phase of superfluid he 3 in anisotropic aerogel. *Physical Review Letters*, 115(16):165304, 2015.

[52] E. V. H. Doggen and J. J. Kinnunen. Momentum-resolved spectroscopy of a fermi liquid. *Scientific Reports*, 5:9539, 2015.

[53] S. Donadello, S. Serafini, M. Tylutki, L. P. Pitaevskii, F. Dalfovo, G. Lamporesi, and G. Ferrari. Observation of solitonic vortices in bose-einstein condensates. *Physical Review Letters*, 113(6):065302, 2014.

[54] Russell J Donnelly. *Quantized vortices in helium II*, volume 2. Cambridge University Press, 1991.

[55] G. Dufour and G. Orso. Anderson localization of pairs in bichromatic optical lattices. *Physical Review Letters*, 109(15):155306, 2012.

[56] S. Dutta and E. J. Mueller. Collective modes of a soliton train in a fermi superfluid. *arXiv preprint arXiv:1612.04845*, 2016.

[57] Z. Dutton, M. Budde, C. Slowe, and L. V. Hau. Observation of quantum shock waves created with ultra-compressed slow light pulses in a bose-einstein condensate. *Science*, 293(5530):663–668, 2001.

[58] A. Eilmes, U. Grimm, R. A. Römer, and M. Schreiber. Two interacting particles at a metal-insulator transition. *The European Physical Journal B-Condensed Matter and Complex Systems*, 8(4):547–554, 1999.

[59] J. Eisert, M. Friesdorf, and C. Gogolin. Quantum many-body systems out of equilibrium. *Nature Physics*, 11(2):124–130, 2015.

[60] J. Elbs, Y. M. Bunkov, E. Collin, H. Godfrin, and G. E. Volovik. Strong orientational effect of stretched aerogel on the he 3 order parameter. *Physical Review Letters*, 100(21):215304, 2008.

[61] DL Feder, MS Pindzola, LA Collins, BI Schneider, and CW Clark. Dark-soliton states of bose-einstein condensates in anisotropic traps. *Physical Review A*, 62(5):053606, 2000.

[62] A. L. Fetter and A. A. Svidzinsky. Vortices in a trapped dilute bose-einstein condensate. *Journal of Physics: Condensed Matter*, 13(12):R135, 2001.

[63] I. A. Fomin. Phenomenological phase diagram of superfluid 3he in a stretched aerogel. *Journal of Experimental and Theoretical Physics*, 118(5):765–770, 2014.

[64] D. J. Frantzeskakis. Dark solitons in atomic bose–einstein condensates: from theory to experiments. *Journal of Physics A: Mathematical and Theoretical*, 43(21):213001, 2010.

[65] J. P. Gaebler, J. T. Stewart, T. E. Drake, D. S. Jin, A. Perali, P. Pieri, and G. C. Strinati. Observation of pseudogap behaviour in a strongly interacting fermi gas. *Nature Physics*, 6(8):569–573, 2010.

[66] N. S. Ginsberg, J. Brand, and L. V. Hau. Observation of hybrid soliton vortex-ring structures in bose-einstein condensates. *Physical Review Letters*, 94(4):040403, 2005.

[67] N. Goldman, J. Beugnon, and F. Gerbier. Detecting chiral edge states in the hofstadter optical lattice. *Physical Review Letters*, 108(25):255303, 2012.

[68] N. Goldman, J. Beugnon, and F. Gerbier. Identifying topological edge states in 2d optical lattices using light scattering. *The European Physical Journal Special Topics*, 217(1):135–152, 2013.

[69] N. Goldman, J. Dalibard, A. Dauphin, F. Gerbier, M. Lewenstein, P. Zoller, and I. B. Spielman. Direct imaging of topological edge states in cold-atom systems. *Proceedings of the National Academy of Sciences*, 110(17):6736–6741, 2013.

[70] A. Gómez-León and G. Platero. Floquet-bloch theory and topology in periodically driven lattices. *Physical Review Letters*, 110(20):200403, 2013.

[71] I. V. Gornyi, A. D. Mirlin, and D. G. Polyakov. Interacting electrons in disordered wires: Anderson localization and low-t transport. *Physical Review Letters*, 95(20):206603, 2005.

[72] I. Gotlibovych, T. F. Schmidutz, A. L. Gaunt, N. Navon, R. P. Smith, and Z. Hadzibabic. Observing properties of an interacting homogeneous bose-einstein condensate: Heisenberg-limited momentum spread, interaction energy, and free-expansion dynamics. *Physical Review A*, 89(6):061604, 2014.

[73] M. Guilleumas, D. M. Jezek, R. Mayol, M. Pi, and M. Barranco. Generating vortex rings in bose-einstein condensates in the line-source approximation. *Physical Review A*, 65(5):053609, 2002.

[74] P. Hauke, O. Tieleman, A. Celi, C. Ölschläger, J. Simonet, J. Struck, M. Weinberg, P. Windpassinger, K. Sengstock, M. Lewenstein, et al. Non-abelian gauge fields and topological insulators in shaken optical lattices. *Physical Review Letters*, 109(14):145301, 2012.

[75] R. Haussmann, M. Punk, and W. Zwerger. Spectral functions and rf response of ultracold fermionic atoms. *Physical Review A*, 80(6):063612, 2009.

[76] C. W. Hicks, D. O. Brodsky, E. A. Yelland, A. S. Gibbs, J. A. N. Bruin, M. E. Barber, S. D. Edkins, K. Nishimura, S. Yonezawa, Y. Maeno, et al. Strong increase of tc of sr2ruo4 under both tensile and compressive strain. *Science*, 344(6181):283–285, 2014.

[77] D. Ho and J. Gong. Topological effects in chiral symmetric driven systems. *Physical Review B*, 90(19):195419, 2014.

[78] T.-L. Horng, S.-C. Gou, and T.-C. Lin. Bending-wave instability of a vortex ring in a trapped bose-einstein condensate. *Physical Review A*, 74(4):041603, 2006.

[79] C. H. Hsueh, S.-C. Gou, T. L. Horng, and Y.-M. Kao. Vortex-ring solutions of the gross–pitaevskii equation for an axisymmtrically trapped bose–einstein condensate. *Journal of Physics B: Atomic, Molecular and Optical Physics*, 40(24):4561, 2007.

[80] D. A. Huse, R. Nandkishore, and V. Oganesyan. Phenomenology of fully many-body-localized systems. *Physical Review B*, 90(17):174202, 2014.

[81] R. Ikeda. Anisotropic strong-coupling effects on superfluid he 3 in aerogels: Conventional spin-fluctuation approach. *Physical Review B*, 91(17):174515, 2015.

[82] S. Iyer, V. Oganesyan, G. Refael, and D. A. Huse. Many-body localization in a quasiperiodic system. *Physical Review B*, 87(13):134202, 2013.

[83] B. Jackson, J. F. McCann, and C. S. Adams. Vortex line and ring dynamics in trapped bose-einstein condensates. *Physical Review A*, 61(1):013604, 1999.

[84] F. Jendrzejewski, A. Bernard, K. Mueller, P. Cheinet, V. Josse, M. Piraud, L. Pezzé, L. Sanchez-Palencia, A. Aspect, and P. Bouyer. Three-dimensional localization of ultracold atoms in an optical disordered potential. *Nature Physics*, 8(5):398–403, 2012.

[85] C. A. Jones, S. J. Putterman, and P. H. Roberts. Motions in a bose condensate. v. stability of solitary wave solutions of non-linear schrodinger equations in two and three dimensions. *Journal of Physics A: Mathematical and General*, 19(15):2991, 1986.

[86] C. A. Jones and P. H. Roberts. Motions in a bose condensate. iv. axisymmetric solitary waves. *Journal of Physics A: Mathematical and General*, 15(8):2599, 1982.

[87] A. M. Kamchatnov and L. P. Pitaevskii. Stabilization of solitons generated

by a supersonic flow of bose-einstein condensate past an obstacle. *Physical Review Letters*, 100(16):160402, 2008.

[88] M. Kardar. *Statistical physics of particles*. Cambridge University Press, 2007.

[89] Y. T. Katan and D. Podolsky. Generation and manipulation of localized modes in floquet topological insulators. *Physical Review B*, 88(22):224106, 2013.

[90] M. Killi, S. Trotzky, and A. Paramekanti. Anisotropic quantum quench in the presence of frustration or background gauge fields: A probe of bulk currents and topological chiral edge modes. *Physical Review A*, 86(6):063632, 2012.

[91] T. Kitagawa, E. Berg, M. Rudner, and E. Demler. Topological characterization of periodically driven quantum systems. *Physical Review B*, 82(23):235114, 2010.

[92] S. N. Klimin, J. Tempere, G. Lombardi, and J. T. Devreese. Finite temperature effective field theory and two-band superfluidity in fermi gases. *The European Physical Journal B*, 88(5):122, 2015.

[93] S. Koghee, L.-K. Lim, M. O. Goerbig, and C. M. Smith. Merging and alignment of dirac points in a shaken honeycomb optical lattice. *Physical Review A*, 85(2):023637, 2012.

[94] S. S. Kondov, W. R. McGehee, J. J. Zirbel, and B. DeMarco. Three-dimensional anderson localization of ultracold matter. *Science*, 334(6052):66–68, 2011.

[95] V. V. Konotop and L. Pitaevskii. Landau dynamics of a grey soliton in a trapped condensate. *Physical Review Letters*, 93(24):240403, 2004.

[96] J. Koplik and H. Levine. Scattering of superfluid vortex rings. *Physical Review Letters*, 76(25):4745, 1996.

[97] Mark J. H. Ku, W. Ji, B. Mukherjee, E. Guardado-Sanchez, L. W. Cheuk, T. Yefsah, and M. W. Zwierlein. Motion of a solitonic vortex in the bec-bcs crossover. *Physical Review Letters*, 113(6):065301, 2014.

[98] Mark J. H. Ku, B. Mukherjee, T. Yefsah, and M. W. Zwierlein. Cascade

of solitonic excitations in a superfluid fermi gas: From planar solitons to vortex rings and lines. *Physical Review Letters*, 116(4):045304, 2016.

[99] E. A. Kuznetsov and S. K. Turitsyn. Instability and collapse of solitons in media with a defocusing nonlinearity. *Sov. Phys. JETP*, 67(8):1583–1588, 1988.

[100] EA Kuznetsov and J Juul Rasmussen. Instability of two-dimensional solitons and vortices in defocusing media. *Physical Review E*, 51(5):4479, 1995.

[101] G. Lamporesi, S. Donadello, S. Serafini, F. Dalfovo, and G. Ferrari. Spontaneous creation of kibble-zurek solitons in a bose-einstein condensate. *Nature Physics*, 9(10):656–660, 2013.

[102] G. Lawes and J. M. Parpia. Estimate of the gap parameter for superfluid 3 he in aerogel. *Physical Review B*, 65(9):092511, 2002.

[103] X. Li, S. Ganeshan, J. H. Pixley, and S. D. Sarma. Many-body localization and quantum nonergodicity in a model with a single-particle mobility edge. *Physical Review Letters*, 115(18):186601, 2015.

[104] R. Liao and J. Brand. Traveling dark solitons in superfluid fermi gases. *Physical Review A*, 83(4):041604, 2011.

[105] Y.-J. Lin, R. L. Compton, K. Jimenez-Garcia, J. V. Porto, and I. B. Spielman. Synthetic magnetic fields for ultracold neutral atoms. *Nature*, 462(7273):628–632, 2009.

[106] N. H. Lindner, G. Refael, and V. Galitski. Floquet topological insulator in semiconductor quantum wells. *Nature Physics*, 7(6):490–495, 2011.

[107] G. Lombardi, W. Van Alphen, S. N. Klimin, and J. Tempere. Soliton-core filling in superfluid fermi gases with spin imbalance. *Physical Review A*, 93(1):013614, 2016.

[108] Giovanni Lombardi, Wout Van Alphen, Sergei N Klimin, and Jacques Tempere. Snake instability of dark solitons across the bec-bcs crossover: an effective field theory perspective. *arXiv preprint arXiv:1612.07558*, 2016.

[109] A. P. Mackenzie and Y. Maeno. The superconductivity of sr 2 ruo 4 and the physics of spin-triplet pairing. *Reviews of Modern Physics*, 75(2):657, 2003.

[110] P. Magierski, G. Wlazłowski, and A. Bulgac. Onset of a pseudogap regime in ultracold fermi gases. *Physical Review Letters*, 107(14):145304, 2011.

[111] A. V. Mamaev, M. Saffman, and A. A. Zozulya. Propagation of dark stripe beams in nonlinear media: snake instability and creation of optical vortices. *Physical Review Letters*, 76(13):2262, 1996.

[112] A. M. Mateo and J. Brand. Chladni solitons and the onset of the snaking instability for dark solitons in confined superfluids. *Physical Review Letters*, 113(25):255302, 2014.

[113] C. J. M. Mathy, D. A. Huse, and R. G. Hulet. Enlarging and cooling the néel state in an optical lattice. *Physical Review A*, 86(2):023606, 2012.

[114] K. M. Mertes, J. W. Merrill, R. Carretero-González, D. J. Frantzeskakis, P. G. Kevrekidis, and D. S. Hall. Nonequilibrium dynamics and superfluid ring excitations in binary bose-einstein condensates. *Physical Review Letters*, 99(19):190402, 2007.

[115] V. P. Michal, I. L. Aleiner, B. L. Altshuler, and G. V. Shlyapnikov. Finite-temperature fluid–insulator transition of strongly interacting 1d disordered bosons. *Proceedings of the National Academy of Sciences*, 113(31):E4455–E4459, 2016.

[116] H. Miyake, G. A. Siviloglou, C. J. Kennedy, W. C. Burton, and W. Ketterle. Realizing the harper hamiltonian with laser-assisted tunneling in optical lattices. *Physical Review Letters*, 111(18):185302, 2013.

[117] R. Modak and S. Mukerjee. Many-body localization in the presence of a single-particle mobility edge. *Physical Review Letters*, 115(23):230401, 2015.

[118] E. J. Mueller. Evolution of the pseudogap in a polarized fermi gas. *Physical Review A*, 83(5):053623, 2011.

[119] AE Muryshev, HB van Linden van den Heuvell, and GV Shlyapnikov. Stability of standing matter waves in a trap. *Physical Review A*, 60(4):R2665, 1999.

[120] Z. H. Musslimani and J. Yang. Transverse instability of strongly coupled dark–bright manakov vector solitons. *Optics Letters*, 26(24):1981–1983, 2001.

[121] R. Nandkishore and D. A. Huse. Many-body localization and thermalization in quantum statistical mechanics. *Annu. Rev. Condens. Matter Phys.*, 6(1):15–38, 2015.

[122] S. Nascimbene, N. Navon, S. Pilati, F. Chevy, S. Giorgini, A. Georges, and C. Salomon. Fermi-liquid behavior of the normal phase of a strongly interacting gas of cold atoms. *Physical Review Letters*, 106(21):215303, 2011.

[123] T. W. Neely, E. C. Samson, A. S. Bradley, M. J. Davis, and B. P. Anderson. Observation of vortex dipoles in an oblate bose-einstein condensate. *Physical Review Letters*, 104(16):160401, 2010.

[124] P. Nozieres and S. Schmitt-Rink. Bose condensation in an attractive fermion gas: From weak to strong coupling superconductivity. *Journal of Low Temperature Physics*, 59(3-4):195–211, 1985.

[125] B. A. Olsen, M. C. Revelle, J. A. Fry, D. E. Sheehy, and R. G. Hulet. Phase diagram of a strongly interacting spin-imbalanced fermi gas. *Physical Review A*, 92(6):063616, 2015.

[126] F. Palestini, A. Perali, P. Pieri, and G. C. Strinati. Dispersions, weights, and widths of the single-particle spectral function in the normal phase of a fermi gas. *Physical Review B*, 85(2):024517, 2012.

[127] C. V. Parker, L.-C. Ha, and C. Chin. Direct observation of effective ferromagnetic domains of cold atoms in a shaken optical lattice. *Nature Physics*, 2013.

[128] D. E. Pelinovsky and P. G. Kevrekidis. Variational approximations of trapped vortices in the large-density limit. *Nonlinearity*, 24(4):1271, 2011.

[129] A. Perali, F. Palestini, P. Pieri, G. C. Strinati, J. T. Stewart, J. P. Gaebler, T. E. Drake, and D. S. Jin. Evolution of the normal state of a strongly interacting fermi gas from a pseudogap phase to a molecular bose gas. *Physical Review Letters*, 106(6):060402, 2011.

[130] A. Perali, P. Pieri, G. C. Strinati, and C. Castellani. Pseudogap and spectral function from superconducting fluctuations to the bosonic limit. *Physical Review B*, 66(2):024510, 2002.

[131] D. S. Petrov, C. Salomon, and G. V. Shlyapnikov. Weakly bound dimers of fermionic atoms. *Physical Review Letters*, 93(9):090404, 2004.

[132] F. Piazza, L. A. Collins, and A. Smerzi. Instability and vortex ring dynamics in a three-dimensional superfluid flow through a constriction. *New Journal of Physics*, 13(4):043008, 2011.

[133] J. Pollanen, J. I. A. Li, C. A. Collett, W. J. Gannon, W. P. Halperin, and J. A. Sauls. New chiral phases of superfluid 3he stabilized by anisotropic silica aerogel. *Nature Physics*, 8(4):317–320, 2012.

[134] J. V. Porto and J. M. Parpia. Superfluid 3 he in aerogel. *Physical Review Letters*, 74(23):4667, 1995.

[135] H. M. Price and N. R. Cooper. Mapping the berry curvature from semiclassical dynamics in optical lattices. *Physical Review A*, 85(3):033620, 2012.

[136] George William Rayfield and F Reif. Quantized vortex rings in superfluid helium. *Physical Review*, 136(5A):A1194, 1964.

[137] M. C. Rechtsman, J. M. Zeuner, Y. Plotnik, Y. Lumer, D. Podolsky, F. Dreisow, S. Nolte, M. Segev, and A. Szameit. Photonic floquet topological insulators. *Nature*, 496(7444):196–200, 2013.

[138] C. A. Regal and D. S. Jin. Experimental realization of the bcs-bec crossover with a fermi gas of atoms. *Advances In Atomic, Molecular, and Optical Physics*, 54:1–79, 2007.

[139] M. D. Reichl and E. J. Mueller. Vortex ring dynamics in trapped bose-einstein condensates. *Physical Review A*, 88(5):053626, 2013.

[140] G. Roati, C. DErrico, L. Fallani, M. Fattori, C. Fort, M. Zaccanti, G. Modugno, M. Modugno, and M. Inguscio. Anderson localization of a non-interacting bose–einstein condensate. *Nature*, 453(7197):895–898, 2008.

[141] P. H. Roberts and J. Grant. Motions in a bose condensate. i. the structure of the large circular vortex. *Journal of Physics A: General Physics*, 4(1):55, 1971.

[142] V. Ros, M. Mueller, and A. Scardicchio. Integrals of motion in the many-body localized phase. *Nuclear Physics B*, 891:420–465, 2015.

[143] M. S. Rudner, N. H. Lindner, E. Berg, and M. Levin. Anomalous edge states and the bulk-edge correspondence for periodically driven two-dimensional systems. *Physical Review X*, 3(3):031005, 2013.

[144] Y. Sagi, T. E. Drake, R. Paudel, R. Chapurin, and D. S Jin. Breakdown of the fermi liquid description for strongly interacting fermions. *Physical Review Letters*, 114(7):075301, 2015.

[145] J. A. Sauls. Chiral phases of superfluid 3 he in an anisotropic medium. *Physical Review B*, 88(21):214503, 2013.

[146] U. Schneider, L. Hackermüller, J. P. Ronzheimer, S. Will, S. Braun, T. Best, I. Bloch, E. Demler, S. Mandt, D. Rasch, et al. Fermionic transport and out-of-equilibrium dynamics in a homogeneous hubbard model with ultracold atoms. *Nature Physics*, 8(3):213–218, 2012.

[147] M. Schreiber, S. S. Hodgman, P. Bordia, H. P. Lschen, M. H. Fischer, R. Vosk, E. Altman, U. Schneider, and I. Bloch. Observation of many-body localization of interacting fermions in a quasirandom optical lattice. *Science*, 349(6250):842–845, 2015.

[148] R. G. Scott, F. Dalfovo, L. P. Pitaevskii, and S. Stringari. Dynamics of dark solitons in a trapped superfluid fermi gas. *Physical Review Letters*, 106(18):185301, 2011.

[149] R. G. Scott, F. Dalfovo, L. P. Pitaevskii, S. Stringari, O. Fialko, R. Liao, and J. Brand. The decay and collisions of dark solitons in superfluid fermi gases. *New Journal of Physics*, 14(2):023044, 2012.

[150] M. Serbyn, Z. Papić, and D. A. Abanin. Local conservation laws and the structure of the many-body localized states. *Physical Review Letters*, 111(12):127201, 2013.

[151] M. Serbyn, Z. Papić, and D. A. Abanin. Quantum quenches in the many-body localized phase. *Physical Review B*, 90(17):174302, 2014.

[152] Karim Shariff and Anthony Leonard. Vortex rings. *Annual Review of Fluid Mechanics*, 24(1):235–279, 1992.

[153] D. L. Shepelyansky. Two interacting particles in the harper model. *Physical Review B*, 54(21):14896, 1996.

[154] I. Shomroni, E. Lahoud, S. Levy, and J. Steinhauer. Evidence for an oscillating soliton/vortex ring by density engineering of a bose–einstein condensate. *Nature Physics*, 5(3):193–197, 2009.

[155] J. B. Sokoloff. Unusual band structure, wave functions and electrical conductance in crystals with incommensurate periodic potentials. *Physics Reports*, 126(4):189–244, 1985.

[156] D. T. Sprague, T. M. Haard, J. B. Kycia, M. R. Rand, Y. Lee, P. J. Hamot, and W. P. Halperin. Homogeneous equal-spin pairing superfluid state of 3 he in aerogel. *Physical Review Letters*, 75(4):661, 1995.

[157] A. Spuntarelli, L. D. Carr, P. Pieri, and G. C. Strinati. Gray solitons in a strongly interacting superfluid fermi gas. *New Journal of Physics*, 13(3):035010, 2011.

[158] G. C. Strinati. Pairing fluctuations approach to the bcs–bec crossover. In *The BCS-BEC Crossover and the Unitary Fermi Gas*, pages 99–126. Springer, 2012.

[159] J. Struck, C. Ölschläger, M. Weinberg, P. Hauke, J. Simonet, A. Eckardt, M. Lewenstein, K. Sengstock, and P. Windpassinger. Tunable gauge potential for neutral and spinless particles in driven optical lattices. *Physical Review Letters*, 108(22):225304, 2012.

[160] S.-Q. Su, D. E. Sheehy, J. Moreno, and M. Jarrell. Dynamical cluster quantum monte carlo study of the single-particle spectra of strongly interacting fermion gases. *Physical Review A*, 81(5):051604, 2010.

[161] M. Tezuka and A. M. García-García. Testing the universality of the many-body metal-insulator transition by time evolution of a disordered one-dimensional ultracold fermionic gas. *Physical Review A*, 85(3):031602, 2012.

[162] E. V. Thuneberg, S. K. Yip, M. Fogelström, and J. A. Sauls. Models for superfluid h 3 e in aerogel. *Physical Review Letters*, 80(13):2861, 1998.

[163] V. Tikhonenko, J. Christou, B. Luther-Davies, and Y. S. Kivshar. Observation of vortex solitons created by the instability of dark soliton stripes. *Optics Letters*, 21(15):1129–1131, 1996.

[164] Q.-J. Tong, J.-H. An, J. Gong, H.-G. Luo, and C. H. Oh. Generating many majorana modes via periodic driving: A superconductor model. *Physical Review B*, 87(20):201109, 2013.

[165] S. Tsuchiya, R. Watanabe, and Y. Ohashi. Single-particle properties and

pseudogap effects in the bcs-bec crossover regime of an ultracold fermi gas above tc. *Physical Review A*, 80(3):033613, 2009.

[166] S. Tsuchiya, R. Watanabe, and Y. Ohashi. Pseudogap temperature and effects of a harmonic trap in the bcs-bec crossover regime of an ultracold fermi gas. *Physical Review A*, 84(4):043647, 2011.

[167] G. Valtolina, A. Burchianti, A. Amico, E. Neri, K. Xhani, J. A. Seman, A. Trombettoni, A. Smerzi, M. Zaccanti, M. Inguscio, et al. Josephson effect in fermionic superfluids across the bec-bcs crossover. *Science*, 350(6267):1505–1508, 2015.

[168] D. Vollhardt and P. Wölfle. *The superfluid phases of helium 3*. Courier Corporation, 2013.

[169] A. B. Vorontsov and J. A. Sauls. Crystalline order in superfluid he 3 films. *Physical Review Letters*, 98(4):045301, 2007.

[170] R. Vosk, D. A. Huse, and E. Altman. Theory of the many-body localization transition in one-dimensional systems. *Physical Review X*, 5(3):031032, 2015.

[171] L. Wang, Alexey A. S., and M. Troyer. Proposal for direct measurement of topological invariants in optical lattices. *Physical Review Letters*, 110(16):166802, 2013.

[172] Y. Wang, H. Hu, and S. Chen. Many-body ground state localization and coexistence of localized and extended states in an interacting quasiperiodic system. *The European Physical Journal B*, 89(3):1–6, 2016.

[173] S. R. White. Density-matrix algorithms for quantum renormalization groups. *Physical Review B*, 48(14):10345, 1993.

[174] S. R. White and A. E. Feiguin. Real-time evolution using the density matrix renormalization group. *Physical Review Letters*, 93(7):076401, 2004.

[175] J. J. Wiman and J. A. Sauls. Superfluid phases of 3he in a periodic confined geometry. *Journal of Low Temperature Physics*, 175(1-2):17–30, 2014.

[176] T. Yefsah, A. T. Sommer, M. J. H. Ku, L. W. Cheuk, W. Ji, W. S. Bakr, and M. W. Zwierlein. Heavy solitons in a fermionic superfluid. *Nature*, 499(7459):426–430, 2013.

[177] V. E. Zakharov and A. M. Rubenchik. Instability of waveguides and solitons in nonlinear media. *Soviet Journal of Experimental and Theoretical Physics*, 38:494, 1974.

[178] S.-L. Zhang and Q. Zhou. Shaping topological properties of the band structures in a shaken optical lattice. *Physical Review A*, 90(5):051601, 2014.

[179] W. Zheng and H. Zhai. Floquet topological states in shaking optical lattices. *Physical Review A*, 89(6):061603, 2014.

[180] W. Zwerger. *The BCS-BEC crossover and the unitary Fermi gas*, volume 836. Springer Science & Business Media, 2011.